Studies on Indoor Energy Harvesting with Perovskite Solar Cells Toward IoT Applications and Development of Practicable Fabrication Process

(IoT 応用に向けたペロブスカイト型太陽電池を用いた屋内環境発電に関する研究および実用化に向けた作製プロセスの開発)

Itaru RAIFUKU

來福 至

March 2019

Graduate School of Materials Science

Nara Institute of Science and Technology

Abstract

Recently, the concept of “Internet of Things (IoT)” is gradually applied in various fields. For further development of IoT, one of the key issues is how to ensure the power sources. In this thesis, perovskite solar cells (PSCs) were focused as flexible and light power sources for IoT applications. It is considered that PSCs are suitable candidates for power sources of IoT applications due to PSCs have p-i-n structure, which enables solar cells to work even under low-illuminance conditions. However, the characteristics of PSCs under low-illuminance conditions have not been investigated in detail. In this work, the low-illuminance characteristics of PSCs were investigated from the view point of application of PSCs for energy harvesting. Furthermore, to overcome the poor reliability of PSCs, sputtering process was suggested and investigated as a novel fabrication process of PSCs.

In Chapter 2, characteristics of PSCs were investigated under various light intensities with AM 1.5 spectrum, which is similar to emission spectrum of sunlight. It was clarified that PSCs can maintain high open circuit voltage (V_{OC}) under low-illuminance conditions. Comparing with amorphous Si solar cells, which have been used for indoor applications, PSCs showed higher V_{OC} values under same light intensity (PSCs 0.71 V, a-Si 0.58 V at 0.1 mW/cm^2). The internal resistance of PSCs were evaluated with impedance spectroscopy under various light intensities. From the results, it was considered that the mesoporous TiO_2 layer included in PSCs acts as an internal resistance and decreases V_{OC} under low-illuminance conditions. Therefore, a planar structure, which does not have mesoporous layer, was suggested as a suitable device structure under low-illuminance conditions. Furthermore, experimental results showed planar type PSCs

can keep higher V_{OC} than mesostructured PSCs under low-illuminance conditions (mesostructured 0.71V, planar 0.84 V at 0.1 mW/cm^2).

In Chapter 3, characteristics of PSCs were investigated under fluorescent lamp illumination, which is one of the many types of indoor lighting. It was confirmed that PSCs, which have an optimum band gap for AM 1.5 spectrum, showed power conversion efficiency (PCE) of 27.1% under 200 lx condition. In addition, PSCs which have higher band gap than conventional ones showed PCE of over 30% under 200 lx illumination. These PCE are the highest values compared with the other kind of solar cells under similar light intensities. Commonly, higher band gap perovskite materials show phase segregation, which causes poor photovoltaic performance due to formation of recombination site, under 1 sun condition. However, results described in this chapter indicate the phase segregation affect have a slight influence on photovoltaic performance of PSCs under low-illuminance conditions. From stability tests, PSCs stored under ambient condition showed 93% of its initial PCE after being stored for approximately a month.

In Chapter 4, sputtering process was suggested as novel fabrication process of PSCs and the sputter processed perovskite films and PSCs were evaluated. From the XRD measurement and UV/vis spectroscopy, it was confirmed that $CH_3NH_3PbI_3$ perovskite films could be synthesized from sputtered PbI_2 films. After sputtering process for perovskite films have been established, PSCs were fabricated using sputter processed perovskite films. A PCE of 1.84% was confirmed in PSCs employing sputter processed perovskite films. The EQE of the sputter processed PSCs was markedly increased by applying a reverse bias voltage during measurements. It indicated that there is still room to improve the PCE of PSCs by reducing the number of defects in the perovskite films.

Acknowledgements

This work has been done at the Information Device Science Laboratory, Graduate School of Materials Science, Nara Institute of Science and Technology (NAIST), under the direction of Prof. Yukiharu Uraoka.

The author would like to express his deepest appreciation and gratitude to Prof. Yukiharu Uraoka for his kind advices, continuous supporting, valuable suggestions and encouragements to this study as well as critical reading of this thesis. He is also grateful to his supervisors at NAIST; Prof. Hiroshi Daimon, Assoc. Prof. Takashi Matsuo, for their valuable discussions and critical comments for this thesis.

The author sincerely acknowledges to Prof. Peter Chen at National Cheng Kung University, Taiwan, for collaboration work and giving the chance of oversea study to the author in his Laboratory. The author wish to express his deepest thanks to Assoc. Prof. Yasuaki Ishikawa at NAIST, Prof. Seigo Ito at University of Hyogo, for their helpful discussions and valuable advices. The author also indebted to Dr. Thipaine Bourgeteau, Prof. Yvan Bonnassieux, and Prof. Pere Roca i Cabarrocas for their technical advices and comments to conduct collaboration work.

The author also very much applicate to Asst. Prof. Mutsunori Uenuma, Asst. Prof. Mami N. Fujii, Asst. Prof. Juan Paolo Soria Bermundo, Asst. Prof. Masahiro Horita, Mr. Akio Watakabe, and Mr. Hirotoshi Kawahira for the technical help and advice. The author would like to express my appreciation of Ms. Yukiko Morita for her great support and kindness in my daily work.

The author also deeply grateful to Dr. Ippei Inoue, Mr. Kenichi Toyoda, and Yuki Umemura for developing the basis of perovskite solar cells in our laboratory with the aothor.

The author sincerely acknowledge Dr. Naoyuki Shibayama, Dr. Hiroyuki Kanda, Mr. Shota Fukumoto, Dr. Yuji Okamoto, Dr. Yu-Hsien Chiang, Dr. Pei-Ying Lin, and Dr. Ming-Hsien Li for technical advices and helpful discussion. The author also would like to thank Mr. Christian Mark Ocson Pelicano, and Ms. Sachiko Morioka for their assistance on fabrication and measurement.

The author would like to extend his great appreciation to Dr. Takahiro Doe, Dr. Hiroki Kamitake, Dr. Haruka Yamazaki, Dr. Takahiro Ban, Dr. Koji Yoshitsugu, Dr. Satoshi Urakawa, Dr. Shinji Araki, Dr. Seiya Yoshinaga, Dr. Kahori Kise, and Mr. Tatsuki Honda for helpful discussion. The author wish to acknowledge Dr. Syunsuke Uchiyama, Dr. Yuta Fujimoto, Mr. Liu Yang, Ms. Hiromi Okada, Mr. Yuki Tada, Mr. Shun Okazaki, Mr. Yoshiaki Nieda, Mr. Yuki Hashima, Mr. Yuma Karaki, Mr. Yusuke Kawamura, Mr. Kazuki Noguchi, Mr. Takuya Oshima, Mr. Yuya Nakai, Mr. Daisuke Kobayashi, Mr. Go Sasakawa, Mr. Ryosuke Sato, and all of members and graduates of information device science laboratory for their understanding and for sharing good times during this research work.

Finally, the author really thanks his parents, sisters, and all friends for their understanding, support, and encouragement.

March 2019

Itaru RAIFUKU

Contents

List of Abbreviations

Abbreviation	Description
3-cat-Br16	$Cs_{0.05}FA_{0.79}MA_{0.16}Pb(I_{0.84}Br_{0.16})_3$
3-cat-Br50	$Cs_{0.05}FA_{0.79}MA_{0.16}Pb(I_{0.50}Br_{0.50})_3$
AM	Air mass
a-Si	Amorphous silicon
AZO	Aluminum-doped zinc oxide
c-Si	Crystalline silicon
CVD	Chemical vapor deposition
DMF	*N*,*N*-dimethylformamide
DMSO	Dimethyl sulfoxide
DSSCs	Dye sensitized solar cells
EDX	Energy dispersive X-ray spectrometry
EQE	External quantum efficiency
ETL	Electron transport layer
FF	Fill factor
FTO	Fluorine-doped tin oxide
FA	Formamidinium
HTL	Hole transport layer
IoT	Internet of Things
J_{SC}	Short circuit current density
J-V	Current density-voltage
LED	Light emitting diode
Li-TFSI	lithium bis-(trifluoromethanesulfonyl) imide
MA	Methylammonium

mp-TiO_2	Mesoporous TiO_2
OPV	Organic solar cells (Organic photovoltaics)
PCE	Power conversion efficiency
PECVD	Plasma enhanced chemical vapor deposition
P_{MAX}	Maximum output
PSCs	Perovskite solar cells
RF	Radio frequency
SEM	Scanning electron microscopy
Spiro-OMeTAD	2,2',7,7'-tetrakis (*N*,*N*-di-*p*-methoxyphenylamino)-9,9'-spirobifluorene
Rs	Series resistance
Rsh	Shunt resistance
TL	Transmission line
VASP	Vapor assisted solution process
V_{OC}	Open circuit voltage
XRD	X-ray diffraction

Chapter 1

Introduction

1.1 Background

Recently, various things are connected to the internet not only communication facilities such as personal computer and mobile phone. This concept called “Internet of Things (IoT)”, is gradually applied in various fields such as automobile, agriculture, security, and so on. It is reported that the number of things that is connected to the internet will increase up to 50 billion in 2020 [1]. For further development of IoT, one of the key issues is how to ensure the power sources. Although wired power supply and battery with large capacity have been used, they are not suitable for a part of use such as wearable devices, smart skin, and so on (examples are shown in Fig. 1.1). Energy harvesting devices that convert ambient energy to electrical power have attracted much attention as an alternative to overcome this problem. In the IoT applications, vibration energy, piezoelectricity, thermal energy, and solar energy are focused as energy sources of the energy harvesting [2, 3].

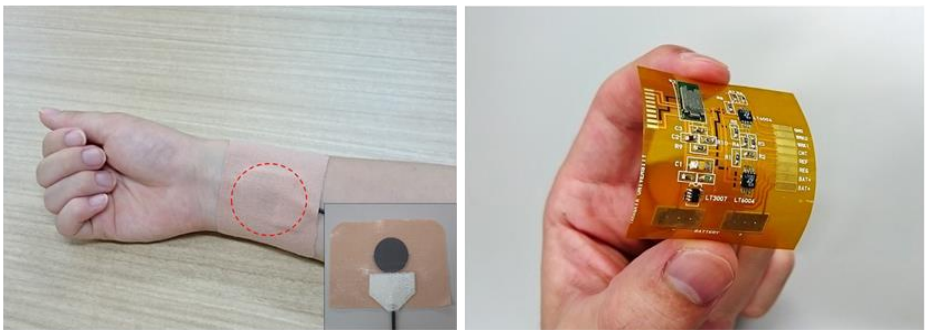

Figure 1.1 Examples of wearable devices [4].

Compact, flexible, and stable devices are ideal as power sources to spread IoT applications. Comparing above energy harvesters, the efficiency of vibration energy harvester decreases when the device area is limited [5]. Although piezoelectric devices can work effectively even device area become small, the lifetime is unclear because of its energy source is physical stress [5]. Thermoelectric devices can also work with small device area. However, flexible and efficient thermoelectric devices at room temperature is still under investigation [6, 7]. By contrast, solar cells can work with small device area and part of solar cells have already commercialized for indoor applications [8]. Moreover, flexible solar cells have already been developed and part of them are working efficiently [9-12]. Therefore, solar cell is one of promising energy harvester for IoT applications.

1.2 Various kinds of solar cells

Solar cell is one of the semiconductor devices that convert solar energy into electrical energy. Solar cells are classified according to the light absorbing materials and the power generation mechanism. Features of representative solar cells are described below.

Crystalline silicon (c-Si) solar cells are consists of p-n junction of p-type and n-type c-Si as shown in Figure 1.2 (a). The c-Si solar cell is most commonly used one because of its high power conversion efficiency (PCE) (26.6%), stability, and reliability [13-15]. On the other hand, it is hard to achieve thin solar cells since c-Si has relatively low light absorption coefficient in visible wavelength region compared with other photovoltaic materials. It is also hard to get flexible solar cells using c-Si wafer.

Amorphous silicon (a-Si) solar cells are consists of p-i-n junction of a-Si as shown in Figure 1.2 (b). Because a-Si has higher absorption coefficient in visible light range than c-Si, it is possible to fabricate thinner solar cells leading lower fabrication cost [16]. However, the PCE of a-Si solar cells is low and they suffer from light induced deterioration [15, 17-18].

Compound solar cells are mainly consist of heterojunction of p-type and n-type compound semiconductor materials. The representative one is $CuInGaSe_2$ (CIGS) solar cell. CIGS solar cells show relatively high PCE of 22.9% [15]. In addition, flexible and thin CIGS solar cells have been developed [10]. The problems of CIGS solar cells are including rare metals and toxic materials.

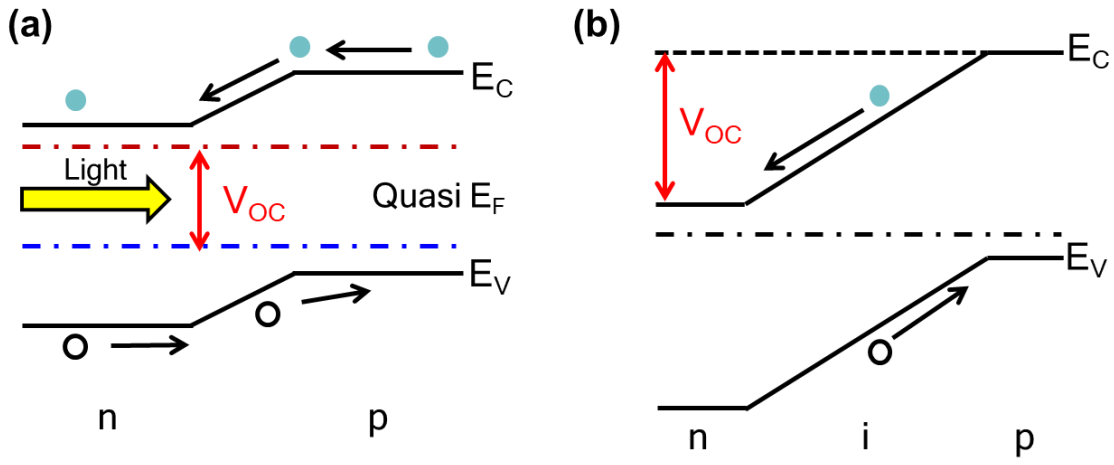

Figure 1.2 Band structure of (a) crystalline Si and (b) amorphous Si solar cells.

Organic thin films solar cells (OPV) includes organic semiconductors as light absorbing materials. Because of its low processing temperature, flexible and light solar cells are achievable [11]. Moreover, it is possible to control the absorption range by tuning the composition of organic materials [19-20]. Relatively poor PCE (12.6% [21]) and stability issue are problems to be solved.

Dye sensitized solar cells (DSSCs) have quite different structure and working mechanism compared with the above solar cells [22, 23]. DSSCs consist of mesoporous TiO_2 (mp-TiO_2), dye, and electrolyte as shown in Figure 1.3. The working mechanism is below; the dye act as a light absorber and generate electrons. The generated electrons are injected into conduction band of mp-TiO_2 layer. The injected electrons move into electrolyte through external circuit. After that, redox reaction occur between dye, electron, and electrolyte. Although flexible solar cells are achievable, long-term stability and low PCE (11.9%) should be improved [12, 15].

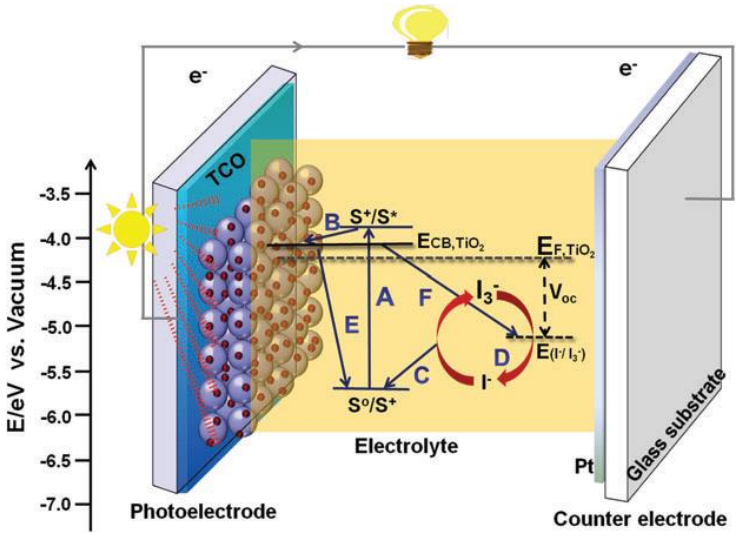

Figure 1.3 Structure and working mechanism of dye sensitized solar cells [23].

Very recently, perovskite solar cells (PSCs) based on DSSCs have emerged as a new type of solar cells. Overview of PSCs are described in next section.

1.3 Overview of perovskite solar cells

1.3.1 Brief history of perovskite solar cells

Miyasaka and coworkers first reported PSCs with a PCE of 3.8% [24]. In the first report, the device structure followed that of liquid DSSCs. Methylammonium lead bromide ($CH_3NH_3PbBr_3$) and methylammonium lead iodide ($CH_3NH_3PbI_3$) were used as the sensitizer instead of organic dyes. Due to electrolytes dissolve those perovskite materials, the device had very poor stability. In 2012, Snaith *et al*. reported solid state PSCs by replacing the electrolyte with an organic semiconductor and the PCE exceeded 10% [25]. After that, many approaches have been applied to improve the PCE of PSCs such as optimizing the fabrication process, controlling the composition of perovskite materials, adding additives, and employing interface modification [26-43]. To date, a PCE of 23.7%, which is comparable to that of c-Si solar cells and compound solar cells has been reported [15]. In the past 9 years, the PCE of PSCs increased from 3.8% to 23.7%. This is one of a unique points of PSCs. Progress of PCE in PSCs are shown in Figure 1.4.

1.3.2 Perovskite compounds for photovoltaic devices

Perovskite structured materials (ABX_3, A: Cation, B: Metal, X: Halogen) are used as the light absorber of PSCs. The crystal structure of perovskite structured materials is shown in Figure 1.5 [44]. In PSCs, organic-inorganic hybrid lead halide perovskite is mainly used as a light absorber. The representative compound is $CH_3NH_3PbX_3$, which was used in the first report. This material has suitable characteristics for photovoltaic devices, such as strong light absorption, low binding

energy of excitons, and tunable bandgap [45-47]. It is possible to control the bandgap of the perovskite by tuning the halogen ratio. For instance, the bandgap increases from 1.5 eV to 2.3 eV by changing the all iodine into bromine [48]. This phenomenon enable us to expect various applications of PSCs such as not only single-junction solar cells but also tandem solar cells.

It is also possible to substitute the cation component. For example, $CsPb(I_{1-x}Br_x)_3$ has been investigated as a light absorber of all-inorganic PSCs [49-51]. Besides that, mixed-cation perovskite materials have also investigated. After the PCE of $CH_3NH_3PbI_3$ based PSCs was saturated, formamidinium-methylammonium mixed-cation perovskite materials have applied as a light absorber. The mixed-cation PSCs showed remarkable PCE of over 20% [52]. Moreover, triple-cation perovskite, which has an additional metal cation such as cesium or potassium in the mixed-cation perovskite, have also showed enormous performance [53].

Interestingly, most of perovskite compounds can be formed by spin-coating of the precursor solution and consequence annealing. This feature also attracted much attention of many researchers. Various fabrication processes of the perovskite compounds are described in subsection 1.3.4.

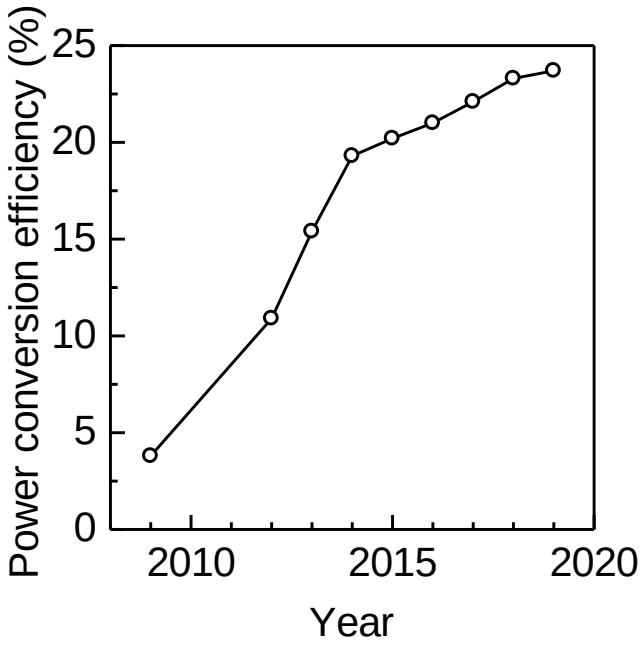

Figure 1.4 Progress of power conversion efficiency in perovskite solar cells [21].

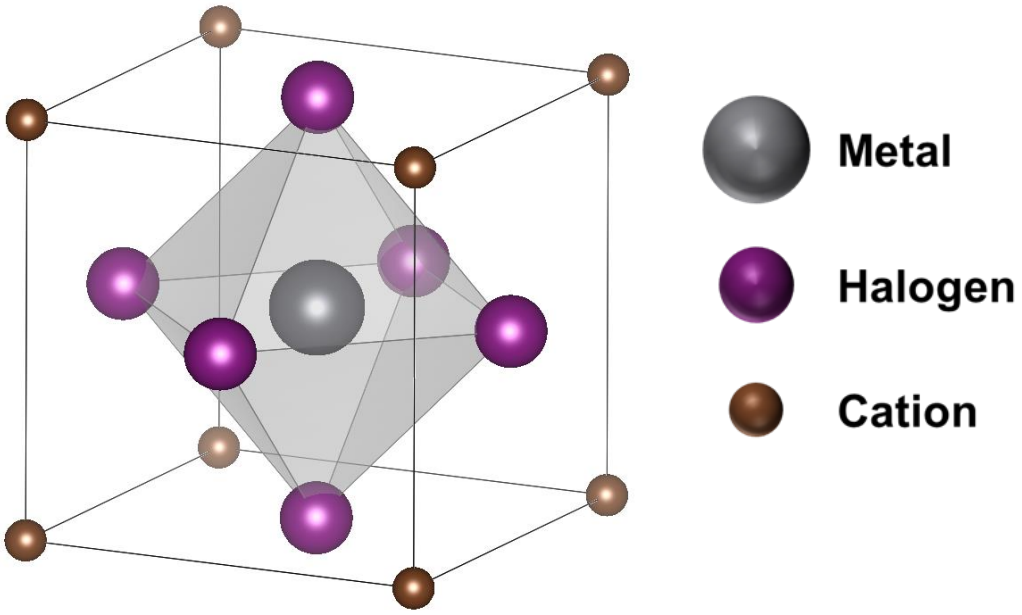

Figure 1.5 Crystal structure of perovskite materials. The structure is written using CIF file from reference [44].

1.3.3 Application of perovskite solar cells in tandem solar cells

Recently, PCE of several solar cells such as c-Si solar cells and PSCs approache their theoretical efficiency. To achieve higher PCE than the theoretical efficiency, tandem solar cells, which combine several solar cells in series, have been investigated. Because its high PCE and tunable bandgap, PSCs is suitable candidate as top cell of tandem solar cells. For example, PSCs and c-Si solar cells show high external quantum efficiency (EQE) at different wavelength ranges, perovskite/c-Si tandem solar cells have attracted much attention, and several investigations have been reported [54-56]. Figure 1.6 shows the device configuration of typical perovskite/c-Si tandem solar cells. The PCE of 26.4%, which is close to the highest PCE of c-Si solar cells has already been reported [57]. Although journal paper have not been published, Oxford PV reported PCE of 27.3% [15, 58]. There is a report on the simulated efficiency of two terminal perovskite/c-Si tandem solar cells. In that report, a projected efficiency of over 30% is suggested [59].

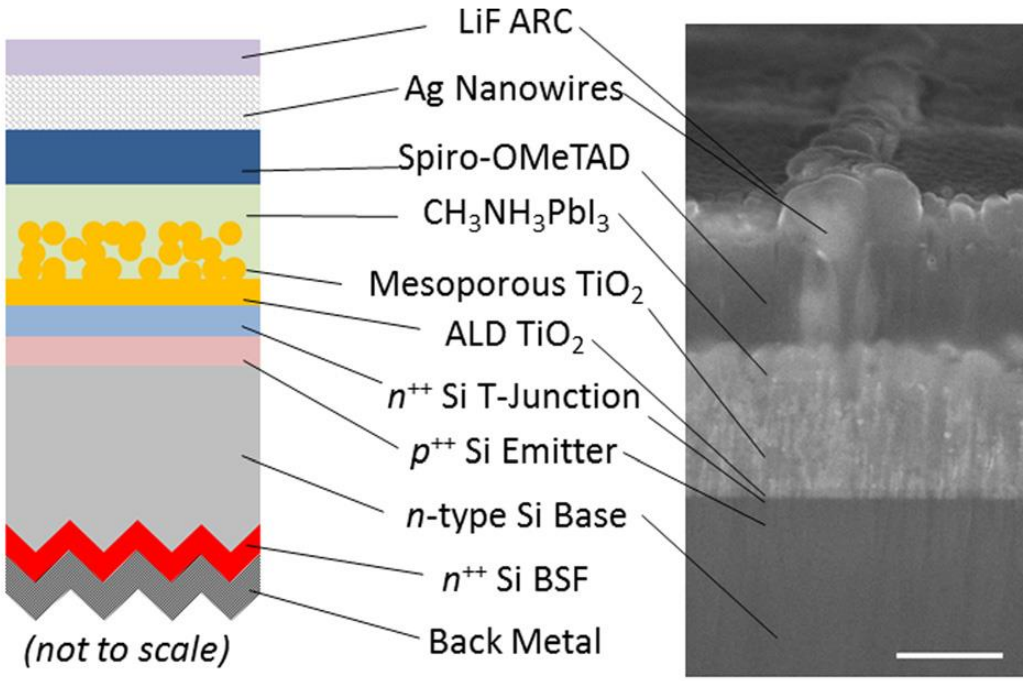

Figure 1.6 Device configuration of perovskite/crystalline Si 2-terminal tandem solar cells [58].

1.3.4 Fabrication process of perovskite thin films

Solution process. As described previous subsection, most of perovskite thin films can be obtained by spin-coating process. In early investigations, perovskite films were fabricated by spin-coating precursor solution including lead halide (PbX_2) and methylammonium halide (CH_3NH_3X) [25]. Then, sequential deposition method was employed to overcome inhomogeneity of perovskite films [26]. In this process, PbX_2 films were first deposited on substrates and then reacted with CH_3NH_3X solution as shown in Figure 1.7 (a). After that, single spin-coating process had attracted attention again due to the facile process. To obtain homogeneous films, anti-solvent crystallization method was applied [28, 29]. During spin-coating process, anti-solvent, which dissolve solvent of precursor solution but does not dissolve perovskite materials, is dropped onto the rotating substrates to facilitate homogeneous crystal nucleation as shown in Figure 1.7 (b). Perovskite films obtained by anti-solvent method show uniform surface morphology and PSCs based on the method show high PCE. Today, the anti-solvent methods is the most commonly used process to fabricate PSCs. It is possible to obtain various perovskite films by controlling the composition of precursor solution. For example, $CH_3NH_3PbI_3$ can be obtained by spin-coating precursor solution including PbI_2 and CH_3NH_3I. Mixed-cation or mixed-halide perovskite films can be obtained by just adding cation-halide or lead-bromide, respectively [53]. To achieve large scale PSCs, other solution processes have also investigated such as screen printing, spray coating, and so on [60].

Vacuum process. Vacuum evaporation is also powerful tool to obtain homogeneous perovskite films. Snaith and coworkers reported co-evaporation processed perovskite films in 2013 [31]. In this report, $CH_3NH_3PbI_3$ films were fabricated by co-evaporation of $PbCl_2$ and CH_3NH_3I as shown in Figure 1.8 (a). Chen *et al*., reported sequential vacuum deposition method. In their process,

$PbCl_2$ films were firstly deposited and then CH_3NH_3I was evaporated on to the obtain $CH_3NH_3PbI_3$ films as shown in Figure 1.8 (b) [32]. Perovskite films obtained by both evaporation process show uniform film thickness over a large area. In addition, evaporation process is able to eliminate moisture, which degrade perovskite materials, from fabrication process. That might leads better stability than solution processed PSCs. By contrast, it is difficult to control composition of perovskite films due to methylammonium sources are difficult to control under vacuum condition [32].

Hybrid process. There are also hybrid process combining solution process and vacuum process. The representatives are vapor assisted solution process (VASP) and chemical vapor deposition (CVD) [61-63]. In both process, PbX_2 films are firstly deposited by spin-coating and then the films are reacted with vaporized cation-halide. Comparing with spin-coating process, hybrid process can obtain homogeneous films with large area. In addition, controlling the composition is easier than vacuum deposition method.

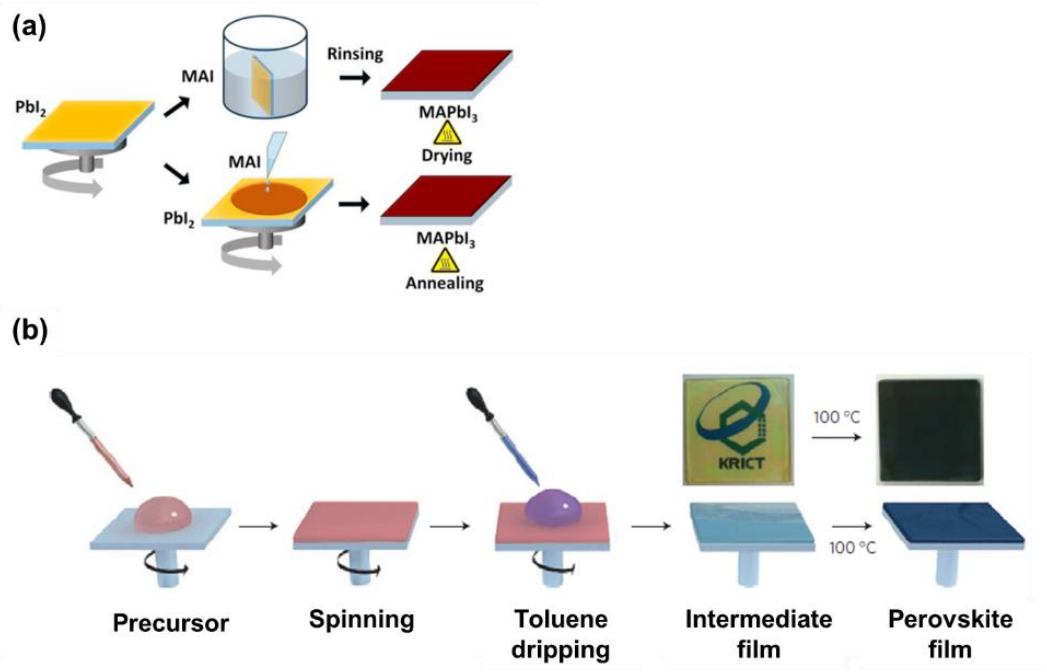

Figure 1.7 Solution process for perovskite solar cells. (a) Sequential process [30] and (b) anti-solvent process [28].

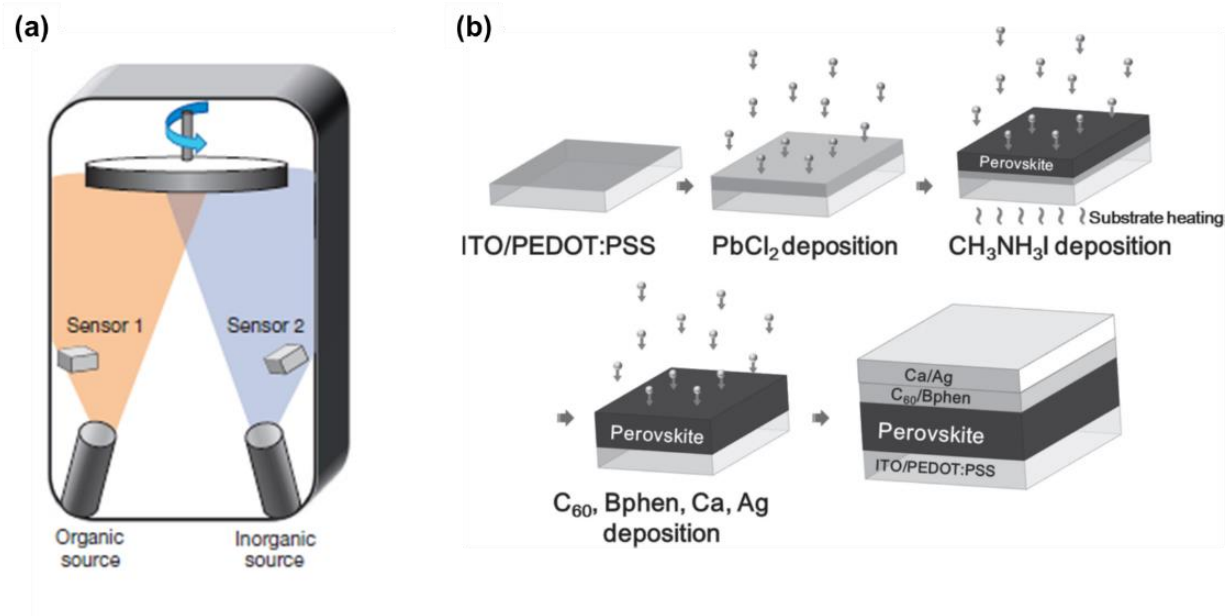

Figure 1.8 Vacuum process for perovskite solar cells. (a) Co-evaporation [31] and (b) sequential evaporation [32].

1.3.5 Device structure of perovskite solar cells

PSCs consist with n-type electron transport layer (ETL), light absorbing perovskite layer, p-type hole transport layer (HTL), and electrodes. The perovskite layer generates electrons and holes under light irradiation. Then, the electrons and holes are injected into ETL and HTL, respectively.

There are mainly 3 types of PSCs as shown in Figure 1.9. First one is mesostructured PSCs, which is consisted by mp-TiO_2 layer in the structure [53]. Because the PSCs emerged from DSSCs, mp-TiO_2 was believed to be a necessary component. Second one is planar PSCs, which does not include mesoporous metal oxide layer in the structure [31]. Owing to the necessity of high temperature annealing to form mp-TiO_2 layer, rigid glass was mainly used as the substrate. After the finding that planar PSCs work efficiently, flexible substrates became available [64, 65]. Above mesostructured and planar PSCs have structure of substrate / ETL / perovskite / HTL / electrode. Third type PSCs called inverted PSCs have structure of substrate / HTL / perovskite / ETL / electrode [66]. By exchanging the place of ETL and HTL, several materials, which are difficult to deposit on perovskite layer, become available. Another advantage of inverted PSCs is its reliability. It normally shows less hysteresis in electrical characteristics than the case of mesostructured and planar PSCs [67]. The hysteresis problem is described in next subsection.

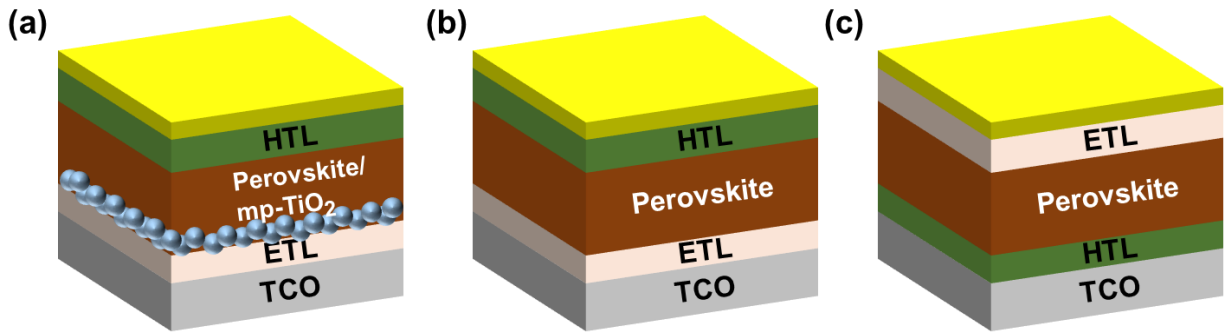

Figure 1.9 Device structure of perovskite solar cells. (a) Mesostructured, (b) Planar structure, and (c) Inverted structure.

1.3.6 Challenges in perovskite solar cells

There are some issues should be solved to commercialize PSCs. Because hybrid perovskite compounds are one of the ionic crystals, they are easily dissolved by water. Thus, PSCs show poor stability under ambient conditions [68]. $CH_3NH_3PbI_3$ films become PbI_2 after exposed to ambient conditions few days as shown in Figure 1.10. Recent studies show some strategy to improve the stability. By introducing large alkyl chain as a cation of perovskite, crystal structure changes from 3D structure to 2D structure. It was found that 2D structure perovskite shows better stability under light illumination and high humidity conditions [69, 70]. 3D perovskite including several cations, called mixed-cation perovskite also show better stability than conventional materials [53]. However, stability issue is still being a challenge comparing with other kind of solar cells.

Second problem is that PSCs showing high PCE include toxic Pb element. So far, several materials have been applied to overcome this problem. Firstly, Sn based perovskite materials (e.g. $CH_3NH_3SnI_3$) have been applied PSCs and showed PCE of 5.73% [71]. However, Sn based perovskite materials are unstable because the perovskite structure is easily decomposed by

oxidization of Sn^{2+} [72]. Hayase and coworkers found that Sn based perovskite become stable by doping Ge element into the perovskite structure and they achieved PCE of 6.9% [73]. Although the stability issue is almost solved, Sn based perovskite is also concerned as a harmful material [74]. After that, Bi, Sb, and Ti based perovskite materials were applied. Because these metals have different valent from Pb, the perovskite structure has different composition (e.g. $A_3B_2X_9$) [75-78]. Although the PCE of Pb-free PSCs is still lower than that of Pb-based one, parts of them are showing enormous stability.

Third problem is reliability of the PSCs. PSCs show hysteresis, which means different current density-voltage (*J-V*) curves dependent on the scan direction as shown in Figure 1.11 [79]. In other words, PCE of PSCs is sensitive to measurement conditions. In general, PSCs show higher PCE by reverse scan (scan direction: forward bias to negative bias) than forward scan (scan direction: negative bias to forward bias). The hysteresis behavior makes it difficult to evaluate the accurate performance of PSCs. The origin of the hysteresis has been discussed and some reasons have been suggested such as ferroelectric effect, ion migration, and capacitance effect [80-83].

Large scale PSCs are also one of the challenging topics. Although PSCs achieved high PCE, the device area is very small such as under 0.1 cm^2. For instance, the PCE of 23.7% was obtained with device area of 0.0739cm^2 [15]. However, the PCE dramatically decreases when the device area is increased. For example, PCE of PSCs decreases from 20.9% down to 11.7% with device area of 1 cm^2, and 703 cm^2, respectively [15].

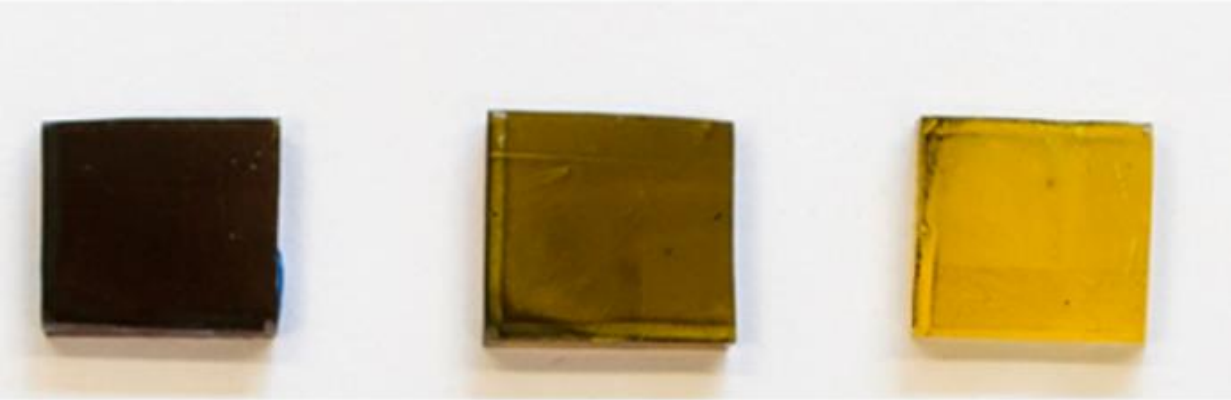

Figure 1.10 Pictures of perovskite films after exposed to ambient condition [68]. Films on right side are exposed to air longer time than left side.

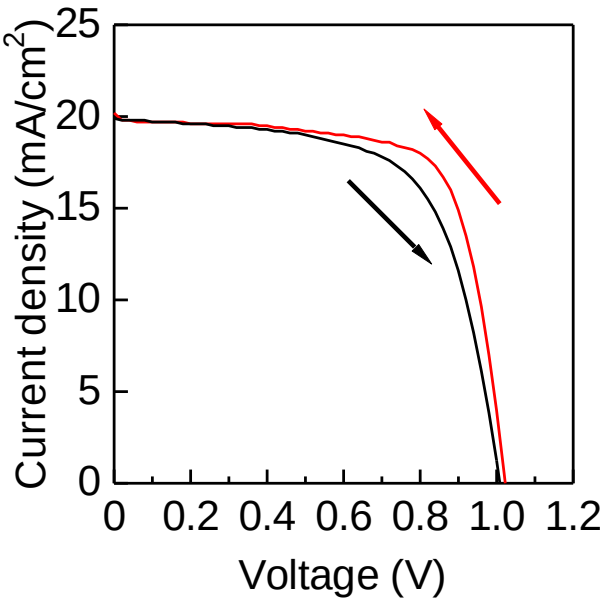

Figure 1.11 Hysteresis in perovskite solar cells. PSCs shows different *J-V* curves depending on the scan direction.

1.4 Solar cells in terms of indoor applications

To date, characteristics of several solar cells such as c-Si, a-Si and DSSCs have been investigated even under low-illuminance conditions [8, 84, 85]. Comparing c-Si and a-Si solar cells, c-Si solar cells show higher PCE under sun light. By contrast, a-Si solar cells show higher efficiency under LED or fluorescent lamp illumination. DSSCs show higher efficiency than a-Si solar cells under both illuminations. This is mainly because of the spectral matching and device structure. The absorption spectrum of typical PSCs cover the emission spectra of typical indoor lighting such as LED and fluorescent lamp [47, 86]. Also, PSCs have p-i-n structure, which enables solar cells to work even under low-illuminance conditions (described in Chapter 2), like a-Si solar cells. Moreover, PSCs show higher PCE than a-Si and DSSCs [15]. Therefore, it is expected that PSCs shows high PCE even under low-illuminance conditions. If PSCs work effectively even under low-illuminance conditions, it will be a promising candidate of indoor energy harvesting. However, there are only few reports on the characteristics of PSCs under low-illuminance conditions [86].

1.5 Objective and outline of this thesis

As described previous subsections, PSCs will work efficiently even under low-illuminance conditions. In addition, because flexible PSCs have been developed, PSCs are available for various applications such as wireless power sources of IoT applications. However, the performance of PSCs under such low-illuminance conditions are still unclear. In this thesis, the low-illuminance characteristics of PSCs are described from the view point of application of PSCs to power sources

for IoT. From the obtained experimental results, it was found that PSCs have great potential as power sources under low-illuminance conditions.

Another noticeable issue of PSCs is their reliability. Although PSCs shows high efficiency with small device area, large area device is still a challenge as described above subsection. Stability issue and reproducibility of PSCs should be solved to commercialize PSCs. In this thesis, sputtering, one of the dry processes is proposed as a novel fabrication process of PSCs to overcome above problems.

In Chapter 2, *J-V* characteristics of PSCs were evaluated under various light intensities with standard AM1.5 spectrum. In addition, the characteristics were compared with conventional c-Si and a-Si solar cells. Furthermore, internal resistance of PSCs under various illuminance were evaluated by employing impedance spectroscopy. Based on the results of impedance spectroscopy, a better device structure for low-illuminance applications was suggested and the performance was investigated.

In Chapter 3, the performance of PSCs under indoor lighting was evaluated using 200 lx fluorescent lamp. In addition, the effect of band gap tuning of perovskite materials on the device performance was investigated. Furthermore, the stability of PSCs under low-illuminance condition was evaluated.

In Chapter 4, sputtering process was employed as a novel fabrication process of PSCs. Perovskite films that have composition of $CH_3NH_3PbI_3$ were prepared from sputtered PbI_2 films. The composition of fabricated films were confirmed by X-ray diffraction measurement. Furthermore, sputter processed perovskite films were applied as light absorbing layer of PSCs and

the device performance was evaluated. In addition, morphology of sputter processed perovskite films on textured substrates was investigated.

In Chapter 5, the conclusions of this study and future outlook are summarized.

References

[1] CISCO IBSG, "Embracing the Internet of Everything To Capture Japan's Share of $14.4 Trillion", (2013).

[2] J. M. Gilbert, and F. Balouchi, *International Journal of Automation and Computing* ***05,*** 334 (2008).

[3] A. Raj, and D. Steingart, *J. Electrochem. Soc*. **165**, B3130 (2018).

[4] T. Sekine, R. Sugano, T. Tashiro, J. Sato, Y. Takeda, H. Matsui, D. Kumaki, F. D. D. Santos, A. Miyabo, and S. Tokito, *Sci. Rep.* **8**, 4442 (2018).

[5] I. Kanno, *J. Surf. Finish. Soc. Jpn*. **67**, 348 (2016).

[6] K. Umeda, M. Uenuma, D. Senaha, J. C. Felizco, Y. Uraoka, and H. Adachi, *J. Phys.: Conf. Ser*. **1052**, 012016 (2018).

[7] B. M. M. Faustino, D. Gomes, J. Faria, T. Juntunen, G. Gaspar, C. Bianchi, A. Almeida, A. Marques, I. Tittonen, and I. Ferreira, *Sci. Rep*. **8**, 6867 (2018).

[8] Y. Li, N. J. Grabham, S. P. Beeby, and M. J. Tudor, *Solar Energy* **111**, 21 (2015).

[9] T. Söderström, F.-J. Haug, V. T.-Daudrix, and C. Ballif, *J. Appl. Phys*. **103**, 114509 (2008).

[10] F. Kessler, and D. Rudmann, *Solar Energy* **77**, 685 (2004).

[11] M. Kaltenbrunner, M. S. White, E. D. Glowacki, T. Sekitani, T. Someya, N. S. Sariciftci, and S. Bauer, *Nature Communications* **3**, 770 (2012).

[12] S. Ito, N.-L. C. Ha, G. Rothenberger, P. Liska, P. Comte, S. M. Zakeeruddin, P. Pechy, M. K. Nazeeruddin, and M. Grätzel, *Chem. Commun*., 4004 (2006).

[13] C. Battaglia, A. Cuevas, and S. D. Wolf, *Energy Environ. Sci*. **9**, 1552 (2016).

[14] K. Yoshikawa, H. Kawasaki, W. Yoshida, T. Irie, K. Konishi, K. Nakano, T. Uto, D. Adachi, M. Kanematsu, H. Uzu, and K. Yamamoto, *Nature Energy* **2**, 17032 (2017).

[15] M. A. Green, Y. Hishikawa, E. D. Dunlop, D. H. Levi, J. H.-Ebinger, and A. W. Y. H.-Baillie, *Prog. Photovolt. Res. Appl*. **27**, 3 (2019).

[16] A. V. Shah, H. Schade, M. Vanecek, J. Meier, E. V.-Sauvain, N. Wyrsch, U. Kroll, C. Droz, and J. Bailat, *Prog. Photovolt. Res. Appl*. **12**, 113 (2004).

[17] T. Matsui, A. Bidiville, K. Maejima, H. Sai, T. Koida, T. Suezaki, M. Matsumoto, K. Saito, I. Yoshida, and M. Kondo, *Appl. Phys. Lett*. **106**, 053901 (2015).

[18] A. Klaver, and R. A. C. M. M. Swaaij, *Sol. Energ. Mat. Sol. C*. **92**, 50 (2008).

[19] K. Colladet, S. Fourier, T. J. Cleij, L. Lutsen, J. Gelan, and D. Vanderzande, *Macromolecules* **40**, 65 (2007).

[20] Z. A. Page, F. Liu, T. P. Russell, and T. Emrick, *J. Polym. Sci. A* **53**, 327 (2015).

[21] NREL, "Best Research-Cell Efficiencies".

[22] M. Grätzel, *J. Photochem. Photobiol. C* **4**, 145 (2003).

[23] C. Ge, M. M. Rahman, N. C. D. Nath, M. J. Ju, K.-M. Noh, and J.-J. Lee, *Bull. Korean Chem. Soc*. **36**, 762 (2015).

[24] A. Kojima, K. Teshima, Y. Shirai, and T. Miyasaka, *J. Am. Chem. Soc.* **131**, 6050 (2009).

[25] M. M. Lee, J. Teuscher, T. Miyasaka, T. N. Murakami, and H. J. Snaith, *Science* **338**, 643 (2012).

[26] J. Burschka, N. Pellet, S.-J. Moon, R. H.-Baker, P. Gao, M. K. Nazeeruddin, and M. Grätzel, *Nature* **499**, 316 (2013).

[27] N. Ahn, D.-Y. Son, I.-H. Jang, S. M. Kang, M. Choi, and N.-G. Park, *J. Am. Chem. Soc.* **137**, 8696 (2015).

[28] N. J. Jeon, J. H. Noh, Y. C. Kim, W. S. Yang, S. Ryu, and S. I. Seok, *Nature Materials* **13**, 897 (2014).

[29] M. Xiao, F. Huang, W. Huang, Y. Dkhissi, Y. Zhu, J. Etheridge, A. G.-Weale, U. Bach, Y.-B. Cheng, and L. Spiccia, *Angew. Chem.* **126**, 10056 (2014).

[30] A.B. Djurisic, F.Z. Liu, H.W. Tam, M. K. Wong, A. Ng, C. Surya, W. Chen, and Z.B. He, *Progress in quantum Electronics* **53**, 1-37 (2017).

[31] M. Liu, M. B. Johnston, and H. J. Snaith, *Nature* **501**, 395 (2013).

[32] C.-W. Chen, H.-W. Kang, S.-Y. Hsiao, P.-F. Yang, K.-M. Chiang, and H.-W. Lin, *Adv. Mater.* **26**, 6647 (2014).

[33] N. J. Jeon, J. H. Noh, W. S. Yang, Y. C. Kim, S. Ryu, J. Seo, and S. I. Seok, *Nature* **517**, 476 (2015).

[34] Y. Sun, J. Peng, Y. Chen, Y. Yao, and Z. Liang, *Sci. Rep.* **7**, 46193 (2017).

[35] M. Zhang, J. S. Yun, Q. Ma, J. Zheng, C. F. J. Lau, X. Deng, J. Kim, D. Kim, J. Seidel, M. A. Green, S. Huang, and A. W. Y. H.-Baillie *ACS Energy Lett.* **2**, 438 (2017).

[36] Z. Tang, T. Bessho, F. Awai, T. Kinoshita, M. M. Maitani, R. Jono, T. N. Murakami, H. Wang, T. Kubo, S. Uchida, and H. Segawa, *Sci. Rep.* **7**, 12183 (2017).

[37] W. S. Yang, J. H. Noh, N. J. Jeon, Y. C. Kim, S. Ryu, J. Seo, S. I. Seok, *Science* **348**, 1234 (2015).

[38] P. Wang, J. Zhang, R. Chen, Z. Zeng, X. Huang, L. Wang, J. Xu, Z. Hu, and Y. Zhu, *Electrochemica Acta* **227**, 180 (2017).

[39] Y. Zhao, J. Wei, H. Li, Y. Yan, W. Zhou, D. Yu, and Q. Zhao, *Nature Communications* **7**, 10228 (2016).

[40] H. Lee, A. Kim, H.-C. Kwon, W. Yang, Y. Oh, D. Lee, and J. Moon, *ACS Appl. Mater. Interfaces* **8**, 29419 (2016).

[41] Y. Wu, F. Xie, H. Chen, X. Yang, H. Su, M. Cai, Z. Zhou, T. Noda, and L. Han, *Adv. Mater.* **28**, 1701073 (2017).

[42] L. Zuo, Z. Gu, T. Ye, W. Fu, G. Wu, H. Li, and H. Chen, *J. Am. Chem. Soc.* **137**, 2674 (2015).

[43] H. Zhou, Q. Chen, G. Li, S. Luo, T. Song, H.-S. Duan, Z. Hong, J. You, Y. Liu, and Y. Yang, *Science* **345**, 542 (2014).

[44] S. G, P. Mahale, B. P. Kore, S. Mukherjee, M. S. Pavan, C. De, S. Ghara, A. Sundaresan, A. Pandey, T. N. G. Row, and D. D. Sarma, *J. Phys. Chem. Lett*. **7**, 2412 (2016).

[45] G. Xing, N. Mathews, S. Sun, S. S. Lim, Y. M. Lam, M. Grätzel, S. Mhaisalkar, and T. C. Sum, *Science* **342**, 344 (2013).

[46] A. Miyata, A. Mitioglu, P. Plochocka, O. Portugall, J. T.-W. Wang, s. D. Stranks, H. J. Snaith, and R. J. Nicholas, *Nature physics* **11**, 582 (2015).

[47] D. P. McMeekin, G. Sadoughi, W. Rehman, G. E. Eperon, M. Saliba, M. T. Hörantner, A. Haghighirad, N. Sakai, L. Korte, B. Rech, M. B. Johnston, L. M. Hertz, and H. J. Snaith, *Science* **351**, 151 (2016).

[48] D. M. Jang, K. Park, D. H. Kim, J. Park, F. Shojaei, H. S. Kang, J.-P. Ahn, J. W. Lee, and J. K. Song, *Nano Lett*. **15**, 5191 (2015).

[49] P. Wang, X. Zhang, Y. Zhou, Q. Jiang, Q. Ye, Z. Chu, X. Li, X. Yang, Z. Yin, and J. You, *Nature Communications* **9**, 2225 (2018).

[50] R. Kottokkaran, H. A. Gaonkar, B. Bagheri, and V. L. Dalal, *J. Vac. Sci. Technol. A* **36**, 041201 (2018).

[51] J. Liang, C. Wang, Y. Wang, Z. Xu, Z. Lu, Y. Ma, H. Zhu, Y. Hu, C. Xiao, X. Yi, G. Zhu, H. Lv, L. Ma, T. Chen, Z. Tie, Z. Jin, and J. Liu, *J. Am. Chem. Soc*. **138**, 15829 (2016).

[52] W. S. Yang, B.-W. Park, E. H. Jung, N. J. Jeon, Y. C. Kim, D. U. Lee, S. S. Shin, J. Seo, E. K. Kim, J. H. Noh, and S. I. Seok, *Science* **356**, 1376 (2017).

[53] M. Saliba, T. Matsui, J.-Y. Seo, K. Domanski, J.-P. C.-Baena, M. K. Nazeeruddin, S. M. Zakeeruddin, W. Tress, A. Abate, A. Hagfeldt and Michael Grätzel, *Energy Environ. Sci.* **9**, 1989 (2016).

[54] J. P. Mailoa, C. D. Bailie, E. C. Johlin, E. T. Hoke, A. J. Akey, W. H. Nguyen, M. D. McGehee, and T. Buonassisi, *Appl. Phys. Lett.* **106**, 121105 (2015).

[55] B. Chen, Y. Bai, Z. Yu, T. Li, X. Zheng, Q. Dong, L. Shen, M. Boccard, A. Gruverman, Z. Holman, and J. Huang, *Adv. Energy Mater.* **6**, 1601128 (2016).

[56] S. Albrecht, M. Saliba, J. P. C. Baena, F. Lang, L. Kegelmann, M. Mews, L. Steier, A. Abate, J. Rappich, L. Korte, R. Schlatmann, M. K. Nazeeruddin, A. Hagfeldt, M. Grätzel, and B. Recha, *Energy Environ. Sci.* **9**, 81-88 (2016).

[57] J. Werner, B. Niesen, and C. Ballif, *Adv. Mater. Interfaces* **5**, 1700731 (2018).

[58] M. Osborne, "Oxford PV takes record perovskite tandem solar cell to 27.3% conversion efficiency"

[59] S. Fostera and S. John, *J. Appl. Phys*. **120**, 103103 (2016).

[60] Y. Rong, Y. Ming, W. Ji, D. Li, A. Mei, Y. Hu, and H. Han, *J. Phys. Chem. Lett*. **9**, 2707 (2018).

[61] Q. Chen, H. Zhou, Z. Hong, S. Luo, H.-S. Duan, H.-H. Wang, Y. Liu, G. Li, and Y. Yang, *J. Am. Chem. Soc*. **136**, 622 (2014).

[62] M. R. Leyden, L. K. Ono, S. R. Raga, Y. Kato, S. Wang, and Y. Qi, *J. Mater. Chem. A* **2**, 18745 (2014).

[63] M.-H. Li, H.-H. Yeh, Y.-H. Chiang, U-S. Jeng, C.-J. Su, H.-W. Shiu, Y.-J. Hsu, N. Kosugi, T. Ohigashi, Y.-A. Chen, P.-S. Shen, P. Chen, and T.-F. Guo, *Adv. Mater.* **30**, 1801401 (2018).

[64] D. Liu, and T. L. Kelly, *Nature photonics* **8**, 133 (2014).

[65] J.-Y. Lam, J.-Y. Chen, P.-C. Tsai, Y.-T. Hsieh, C.-C. Chueh, S.-H. Tung, and W.-C. Chen, *RSC Adv*. **7**, 54361 (2017).

[66] Z. Zhu, Y. Bai, T. Zhang, Z. Liu, X. Long, Z. Wei, Z. Wang, L. Zhang, J. Wang, F. Yan, and S. Yang, *Angew. Chem.* **126**, 12779 (2014).

[67] M. B. Islam, M. Yanagida, Y. Shirai, Y. Nabetani, and K. Miyano, *ACS Omega* **2**, 2291 (2017).

[68] S. N. Habisreutinger, T. Leijtens, G. E. Eperon, S. D. Stranks, R. J. Nicholas, and H. J. Snaith, *Nano Lett*. **14**, 5561 (2014).

[69] I. C. Smith, E. T. Hoke, D. S.-Ibarra, M. D. McGehee, and H. I. Karunadasa, *Angew. Chem*. **126**, 11414 (2014).

[70] G. Grancini, C. R.-Carmona, I. Zimmermann, E. Mosconi, X. Lee, D. Martineau, S. Narbey, F. Oswald, F. D. Angelis, M. Grätzel, and M. K. Nazeeruddin, *Nature Communications* **8**, 15684 (2017).

[71] F. Hao, C. C. Stoumpos, D. H. Cao, R. P. H. Chang, and M. G. Kanatzidis, *Nature photonics* **8**, 489 (2014).

[72] Y. M. Lee, J. Park, B. D. Yu, S. Hong, M.-C. Jung, and M. Nakamura, *J. Phys. Chem. Lett*. **9**, 2293 (2018).

[73] N. Ito, M. A. Kamarudin, D. Hirotani, Y. Zhang, Q. Shen, Y. Ogomi, S. Iikubo, T. Minemoto, K. Yoshino, and S. Hayase, *J. Phys. Chem. Lett*. **9**, 1682 (2018).

[74] A. Babayigit, A. Ethirajan, M. Muller, and B. Conings, *Nature materials* **15**, 247 (2016).

[75] Z. Zhang, X. Li, X. Xia, Z. Wang, Z. Huang, B. Lei, and Y. Gao, *J. Phys. Chem. Lett*. **8**, 4300 (2017).

[76] A. K. Baranwal1, H. Masutani, H. Sugita, H. Kanda, S. Kanaya, N. Shibayama, Y. Sanehira, M. Ikegami, Y. Numata, K. Yamada, T. Miyasaka, T. Umeyama, H. Imahori and S. Ito, *Nano Convergence* **4**, 26 (2017).

[77] P. Karuppuswamy, K. M. Boopathi, A. Mohapatra, H.-C. Chen, K.-T. Wong, P.-C. Wang, and C.-W. Chu, *Nano Energy* **45**, 330 (2018).

[78] M. Chen, M.-G. Ju, A. D. Carl, Y. Zong, R. L. Grimm, J. Gu, X. C. Zeng, Y. Zhou, and N. P. Padture, *Joule* **2**, 558 (2018).

[79] H. J. Snaith, A. Abate, J. M. Ball, G. E. Eperon, T. Leijtens, N. K. Noel, S. D. Stranks, J. T.-W. Wang, K. Wojciechowski, and W. Zhang, *J. Phys. Chem. Lett*. **5**, 1511 (2014).

[80] T. Zhang, H. Chen, Y. Bai, S. Xiao, L. Zhu, C. Hu, Q. Xue, and S. Yang, *Nano Energy* **26**, 620 (2016).

[81] L. Cojocaru, S. Uchida, P. V. V. Jayaweera, S. Kaneko, J. Nakazaki, T. Kubo, and H. Segawa, *Chem. Lett*. **44**, 1750 (2015).

[82] J. Wei, Y. Zhao, H. Li, G. Li, J. Pan, D. Xu, Q. Zhao, and D. Yu, *J. Phys. Chem. Lett*. **5**, 3937 (2014).

[83] N. D. Sankir, and M. Sankir (2017). *Printable Solar Cells*. Scrivener Publishing.

[84] I. Mathews, P. J. King, F. Stafford, and R. Frizzell, *IEEE Journal of Photovoltaics* **6**, 230 (2016).

[85] M. Freitag, J. Teuscher, Y. Saygili, X. Zhang, F. Giordano, P. Liska, J. Hua, S. M. Zakeeruddin, J.-E. Moser, M. Grätzel, and A. Hagfeldt, *Nature photonics* **11**, 372 (2017).

[86] C.-Y. Chen, J.-H. Chang, K.-M. Chiang, H.-L. Lin, S.-Y. Hsiao, and H.-W. Lin, *Adv. Funct. Mater.* **25**, 7064 (2015).

Chapter 2

Characteristics of Perovskite Solar Cells Under Various Light Intensities

2.1 Introduction

PSCs have attracted much attention due to their high PCE and its low fabrication cost. As described in Chapter 1, the common structure of PSCs consists of n-type ETL, intrinsic perovskite layer, p-type HTL, and electrodes. Thus, the device structure of PSCs is a type of p-i-n junction similar to the structure of a-Si solar cells. Owing to an internal electrical field, which is formed between p and n layer to control carrier transport, recombination of carriers is inhibited even under low-level injection conditions. Therefore, PSCs could work under low-illuminance conditions that is one of a low-level injection condition.

In this chapter, the characteristics of PSCs under low-illuminance conditions are discussed. In section 2.3, *J-V* characteristics of mesostructured PSCs under low-illuminance conditions are compared with other kind of solar cells. In section 2.4, internal resistance, which affect open circuit voltage (V_{OC}) of solar cells is evaluated with impedance spectroscopy. In section 2.5, planar structure is suggested as a better structure for indoor application from the results of impedance spectroscopy. In addition, *J-V* characteristics of planar type PSCs are described.

2.2 Experimental

2.2.1 Fabrication process of solar cells

PSCs. Fluorine-doped tin oxide (FTO) coated glass substrates (AGC Fabritech, thickness: 1.8 mm) were etched with zinc powder and 2 M HCl. The etched substrates were then washed with detergent and acetone in an ultrasonic bath for 10 min. Then, UV/O_3 treatment was carried out for 15 min at 115 °C. To prepare ETL, 0.15 M titanium diisopropoxide bis(acetylacetonate) (Sigma-Aldrich, 75 wt% in isopropanol) in 1-butanol was spin-coated on a FTO glass substrate at 700 rpm for 8 s, 1000 rpm for 10 s, and 2000 rpm for 40 s, which was followed by drying at 125 °C for 5 min. The mp-TiO_2 layer was deposited on the ETL by spin-coating with a TiO_2 paste (JGC Co., PST-18NR) diluted in ethanol (2:7, weight ratio) at 1000 rpm for 5 s and 5000 rpm for 25 s. After drying at 125 °C for 5 min, the substrate was annealed at 450 °C for 1 h. Before depositing the perovskite layer, UV/O_3 treatment was carried out again. In order to prepare a perovskite precursor solution, 461 mg of PbI_2, 159 mg of CH_3NH_3I, and 78 mg of DMSO was mixed in 600 mg of DMF and then stirred at room temperature for 3 h. The precursor solution was spin-coated on mp-TiO_2 layer at 4000 rpm for 25 s and 0.5 mL of diethyl ether was dripped on the rotating substrate at 6 s after starting the spin-coating. After spin-coating, the substrate was annealed at 65 °C for 1 min and 100 °C for 2 min. 2,2',7,7'-tetrakis (*N,N*-di-*p*-methoxyphenylamino)-9,9'-spirobifluorene (spiro-OMeTAD) solution consisting of 17 mg spiro-OMeTAD, 6.9 μL of 4-*tert*-butylpyridine, and 4.2 μL of lithium bis-(trifluoromethanesulfonyl) imide (Li-TFSI) solution (520 mg Li-TFSI in 1 mL acetonitrile) in 240 μL of chlorobenzene was spin-coated on the perovskite layer at 1000 rpm for 4 s and 4000 rpm for 26 s to form a HTL. Finally, an Au electrode was deposited by

thermal deposition on the HTL. Planar type PSCs were fabricated by same process expect spin-coating of mp-TiO_2 paste.

c-Si solar cells. P-type Si wafer (resistivity: 1-5 Ω・cm, thickness: 200 μm) was used as a substrate. N-type emitter layer (R_S = 50 Ω/sq.) was formed by phosphorus diffusion using $POCl_3$ at 890 °C. SiN layer was deposited on emitter layer by plasma enhanced chemical vapor deposition (PECVD). Then, Ag paste was applied on the SiN layer by screen printing. After the screen printing, the substrate was annealed at 800 °C in rapid thermal annealing furnace (fire through process). After the fire through process, Al paste was screen printed on back surface of the substrate. Then, substrate was heated at 500 °C for metallization.

a-Si solar cells. Asahi-U substrate was used. 10 nm of p-type a-SiC, 200 nm of intrinsic a-Si, and 20 nm of n-type a-Si were deposited on the substrate by PECVD. Here, a buffer layer inserted between the p-type a-SiC and the intrinsic a-Si was introduced to avoid abrupt change of band gap at the interface by gradual controlling of the carbon concentration. Then, Al doped ZnO (AZO) and Ag layer were formed on n-type a-Si layer. All deposition processes were carried out at less than 200 °C.

The device structure of c-Si and a-Si solar cells are shown in Figure 2.1.

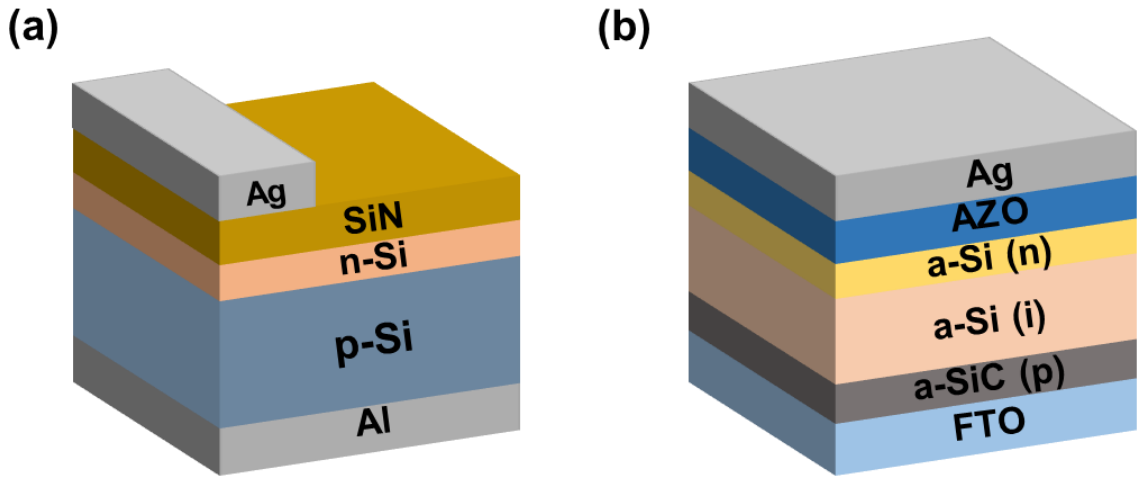

Figure 2.1 Device structure of (a) crystalline Si and (b) amorphous Si solar cells.

2.2.2 Characterization of solar cells

The *J-V* characteristics were measured under AM1.5 spectrum illumination (0.1-100 mW/cm^2) with a solar simulator (Wacom Co., KXL-1000F). In order to adjust the light intensity, ND filter (Opto Sigma) was inserted in AM1.5 illumination. The external quantum efficiency (EQE) was measured using an EQE system (Bunkoukeiki Co., CEP-2000RR) under 0.25 and 0.0025 mW/cm^2 monochromatic lighting of comparable intensity with outdoor and indoor lighting, respectively. The intensity of monochromatic lighting is also adjusted using an ND filter. The active areas of the PSCs, c-Si, and a-Si solar cells were set to 0.09, 0.64, and 1 cm^2 using shadow mask, respectively. Impedance spectroscopy was performed with potentiostat (BioLogic, SP-150) under light illumination (from dark to 100 mW/cm^2, AM1.5 spectrum). The measurements were carried out at frequencies from 1 MHz to 500 mHz with an amplitude voltage of 100 mV.

2.3 Characterization of perovskite solar cells under various light intensities

2.3.1 *J-V* characteristics under low-illuminance conditions

Figure 2.2 shows *J-V* curves of mesostructured PSCs, a-Si, and c-Si solar cells under 100, 50, 10, 1, and 0.1 mW/cm^2 illuminance. The *J-V* characteristics of each solar cells under 100 mW/cm^2 are shown in Table 2.1. The short-circuit current (J_{SC}) of each solar cell decreased in proportion to light intensity, and the behavior was not different for different types of solar cells as shown in Figure 2.3 (a). By contrast, the behavior of V_{OC} was different depending on the type of solar cells.

Figure 2.3 (b) shows V_{OC} of each solar cells under various light intensities. The value is normalized using V_{OC} value under 100 mW/cm^2 illuminance. At 0.1 mW/cm^2 illuminance, which is comparable to the light intensity of indoor lighting, the V_{OC} of the c-Si solar cells decreased remarkably to about 10% of the initial voltage. By contrast, the V_{OC} of mesostructured PSCs at 0.1 mW/cm^2 remains at about 70% of its initial voltage. The difference on the behavior of V_{OC} is probably due to the device structure of each solar cell.

The working mechanism of c-Si solar cell is based on the p-n junction. In the p-n junction, the driving force of the carriers is the build-in-potential, and the carrier transfer depends on the diffusion, which is strongly related to the carrier injection level. Also, the carrier concentration of c-Si wafer should be around 10^{16} to 10^{17} cm^{-3} to achieve high V_{OC}. Under high-injection level condition, c-Si shows better carrier lifetime (τ) by trap saturation effect even if c-Si is highly doped. However, the τ is strongly affected by defects in the c-Si and decreases under low-illuminance conditions, which is a low-level injection condition [1]. As a result, the saturation current (J_0) in

solar cells becomes higher, which decreases the V_{OC} of c-Si solar cells under low-illuminance conditions. On the other hand, PSCs have a p-i-n structure (n-type ETL, intrinsic perovskite, and p-type HTL). In the p-i-n structure, carrier collection is aided by an internal electrical field between p and n layer, which helps offset the low lifetimes in some materials, such as a-Si. Therefore, the decrease in τ is not caused easily even under a low-level injection condition in the p-i-n structure [2]. As a result, the V_{OC} of PSCs could be kept at a higher value than that of c-Si solar cells under low-illuminance conditions. Comparing PSCs and a-Si solar cells, which also consist of the p-i-n junction, the normalized V_{OC} value of a-Si solar cells is as similar to that of PSCs. However, the absolute value of V_{OC} is higher in PSCs than that of a-Si solar cells as shown in Figure 2.3 (c). (mesostructured PSC: 0.71 V, a-Si: 0.58 V at 0.1 mW/cm^2).

The relationship between V_{OC}, J_0 and τ is given as follows:

$$V_{OC} \approx \frac{kT}{e} \ln\left(\frac{J_{SC}}{J_0}\right)$$

$$J_0 = \frac{en_iW}{\tau}$$

In the above equation, only J_{SC} is changed by light intensity. Because the J_{SC} decreases in proportion to light intensity, the V_{OC} decreases linearly in semi-log plots. However, when τ decreases severely with injection level such as c-Si solar cells, the behavior of V_{OC} deviates from a linear relationship under low-illuminance conditions. By contrast, the V_{OC} decreases in proportion to light intensity in the PSCs and a-Si solar cells even under low-illuminance conditions since the τ is not strongly affected by injection level.

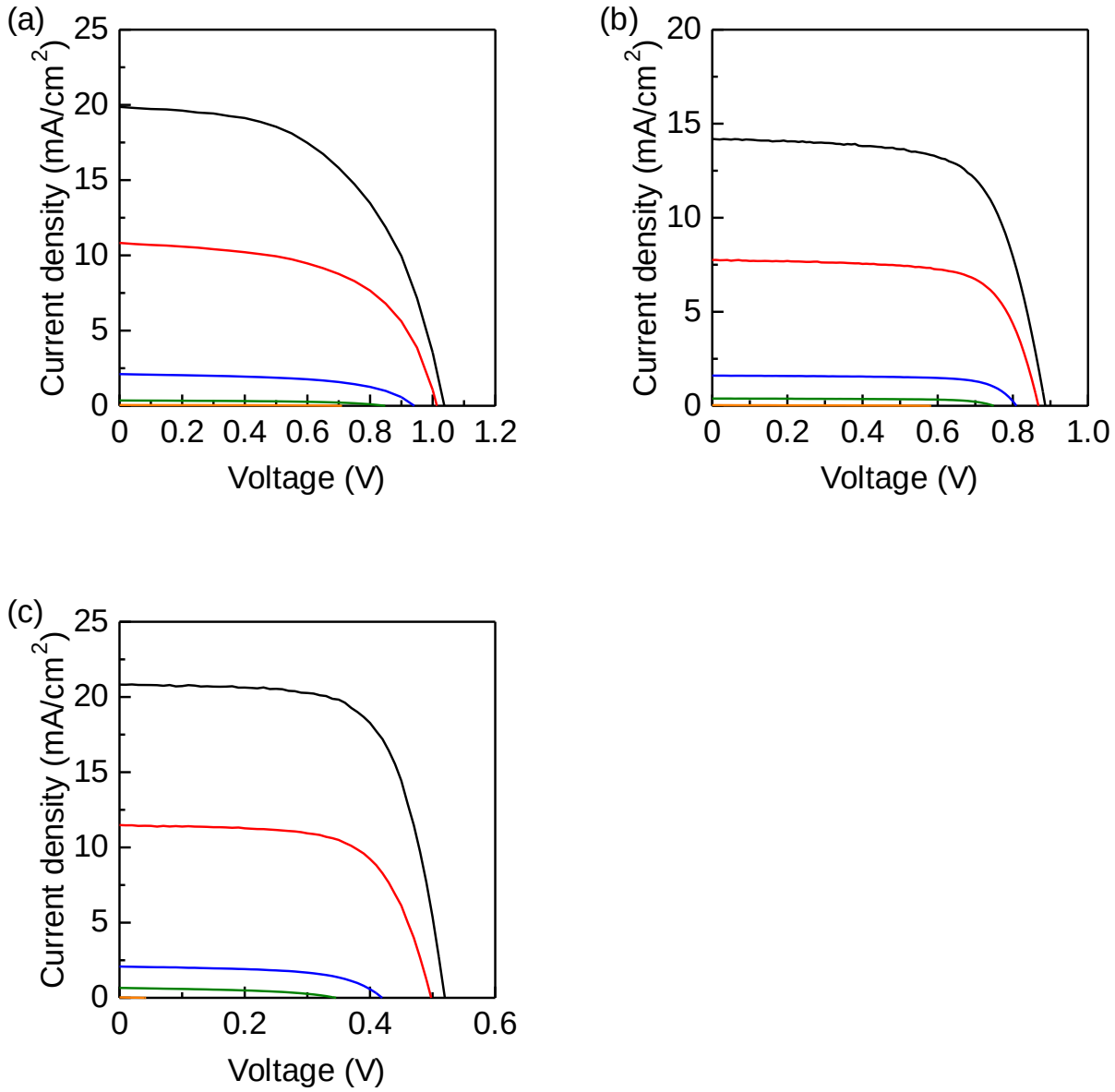

Figure 2.2 Illuminance dependency of the *J-V* characteristics of (a) mesostructured perovskite, (b) amorphous Si, and (c) crystalline Si solar cells. The black, red, blue, green, and orange lines represent the *J-V* curves under 100, 50, 10, 1, and 0.1 mW/cm^2 illumination, respectively.

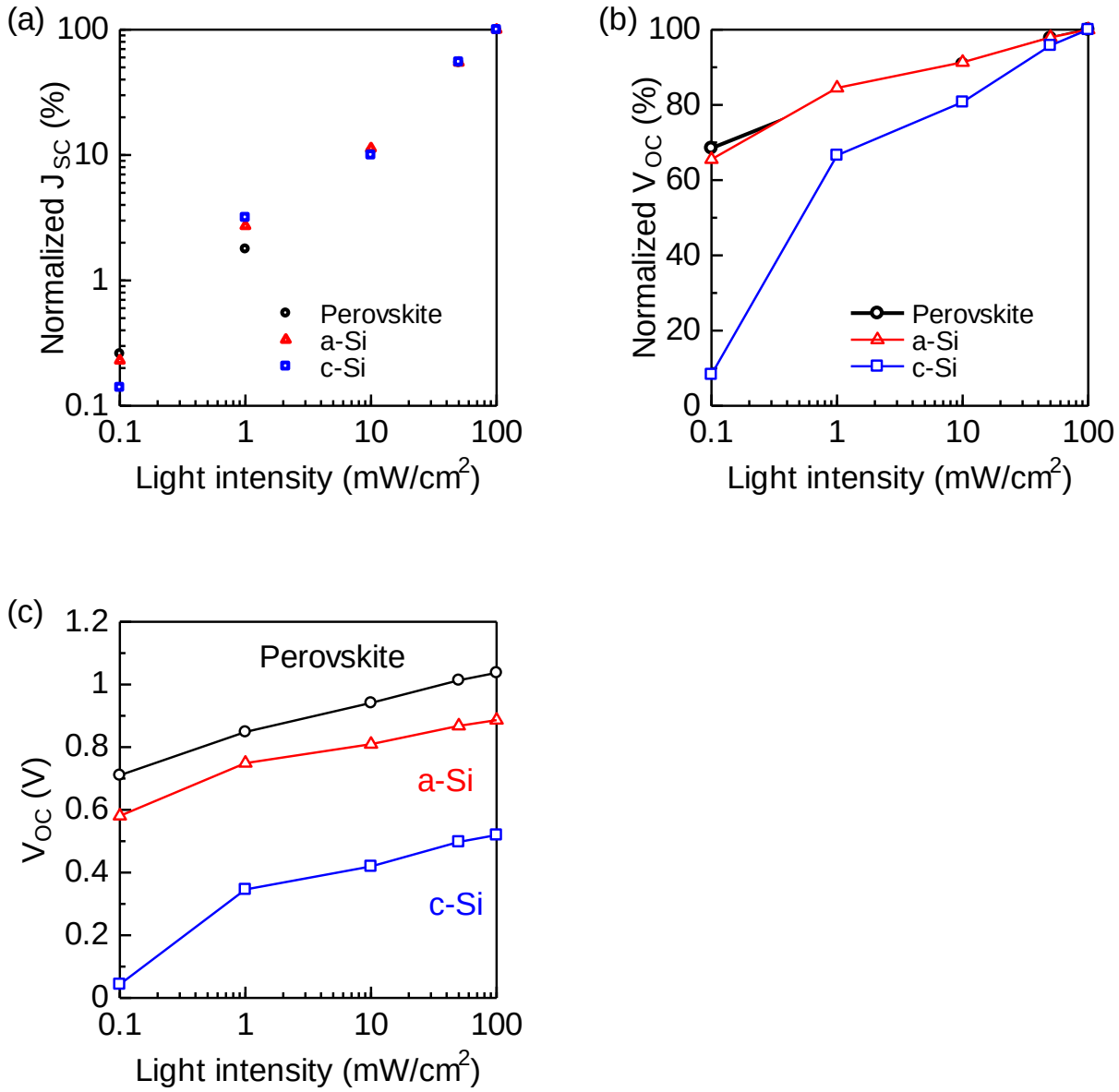

Figure 2.3 (a) Normalized J_{SC}, (b) normalized V_{OC}, and (c) absolute value of V_{OC} of mesostructured perovskite, amorphous Si (a-Si), and crystalline Si (c-Si) solar cells under various illuminance conditions.

Table 2.1. The *J–V* characteristics of mesostructured perovskite (PSCs), amorphous Si (a-Si), and crystalline Si (c-Si) solar cells under AM1.5 spectrum (1sun, 100 mW/cm^2) illumination. (FF: fill factor, PCE: power conversion efficiency).

	J_{SC} (mA/cm^2)	V_{OC} (V)	FF	PCE (%)
PSCs	19.51	1.04	0.643	13.0
a-Si	14.19	0.886	0.672	8.46
c-Si	20.82	0.520	0.676	7.31

2.3.2 Spectral sensitivity under low-illuminance conditions

The spectral sensitivity of PSCs was investigated by utilizing EQE measurement. Figure 2.4 (a) shows the normalized EQE spectra of mesostructured PSCs under 0.25 and 0.0025 mW/cm^2 monochromatic lighting that is the comparable intensity with outdoor and indoor lightings, respectively. As shown in Figure 2.4 (a), the EQE spectra of mesostructured PSCs did not show a large shift due to light intensity as well as a-Si solar cells, which have been used for indoor applications shown in Figure 2.4 (b). In addition, because PSCs showed acceptable spectral response in the wavelength range of 400 to 700 nm, which is included in indoor lighting such as either typical white LED or fluorescent lamp, it is expected that mesostructured PSCs can work effectively not only under sunlight but also under indoor lighting.

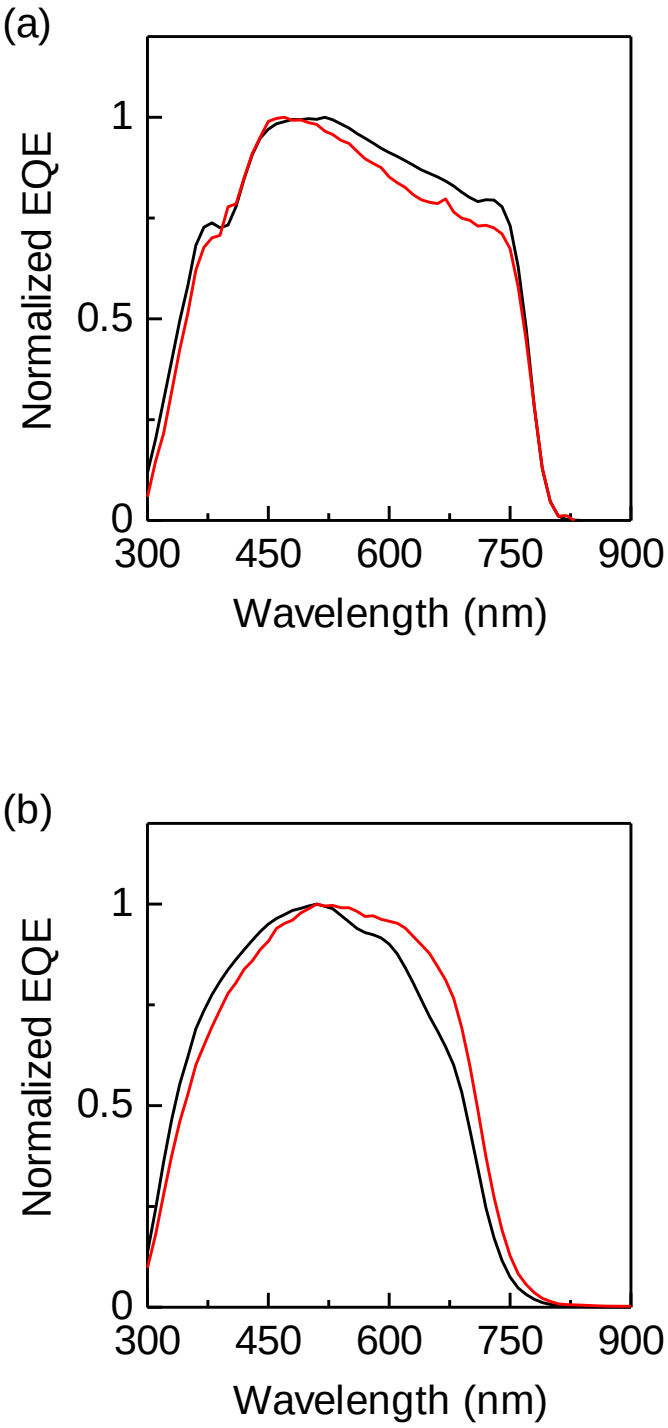

Figure 2.4 Normalized external quantum efficiency (EQE) spectra of (a) mesostructured perovskite and (b) amorphous Si solar cells. The black and red lines represent the normalized EQE under 0.25 and 0.0025 mW/cm^2 illumination, respectively.

2.4 Internal resistance of perovskite solar cells under low-illuminance conditions

Because the spectral sensitivity characteristics of mesostructured PSCs did not show large difference due to light intensity, it is considered that an improvement in the V_{OC} is important for indoor applications. Generally, V_{OC} is related to carrier collection, which depends on the internal resistance of solar cells. Consequently, impedance spectroscopy was performed for mesostructured PSCs to evaluate the internal resistance. Figure 2.5 shows the Nyquist plots of mesostructured PSCs under various illuminance conditions. The highest frequency point shows the resistance from an FTO substrate or external circuit. The semicircle in the high-frequency range is attributed to the diffusion of holes through the hole transport layer. The low-frequency part is attributed to the recombination resistance between the perovskite layer and the TiO_2 layer [3-5]. Under 1 sun illumination, two semicircles were observed in high-frequency and low-frequency range. However, under low-illuminance conditions, such as 0.1 mW/cm^2 illumination, a transmission-line (TL) behavior was observed in the low-frequency range of Nyquist plots. It was reported that the TL behavior is because of the electron transport resistance [6]. Hence, it is considered that the internal resistance of mesostructured PSCs increased under low-illuminance conditions. As a result, the carrier collection efficiency decreased and thus causing V_{OC} to decrease.

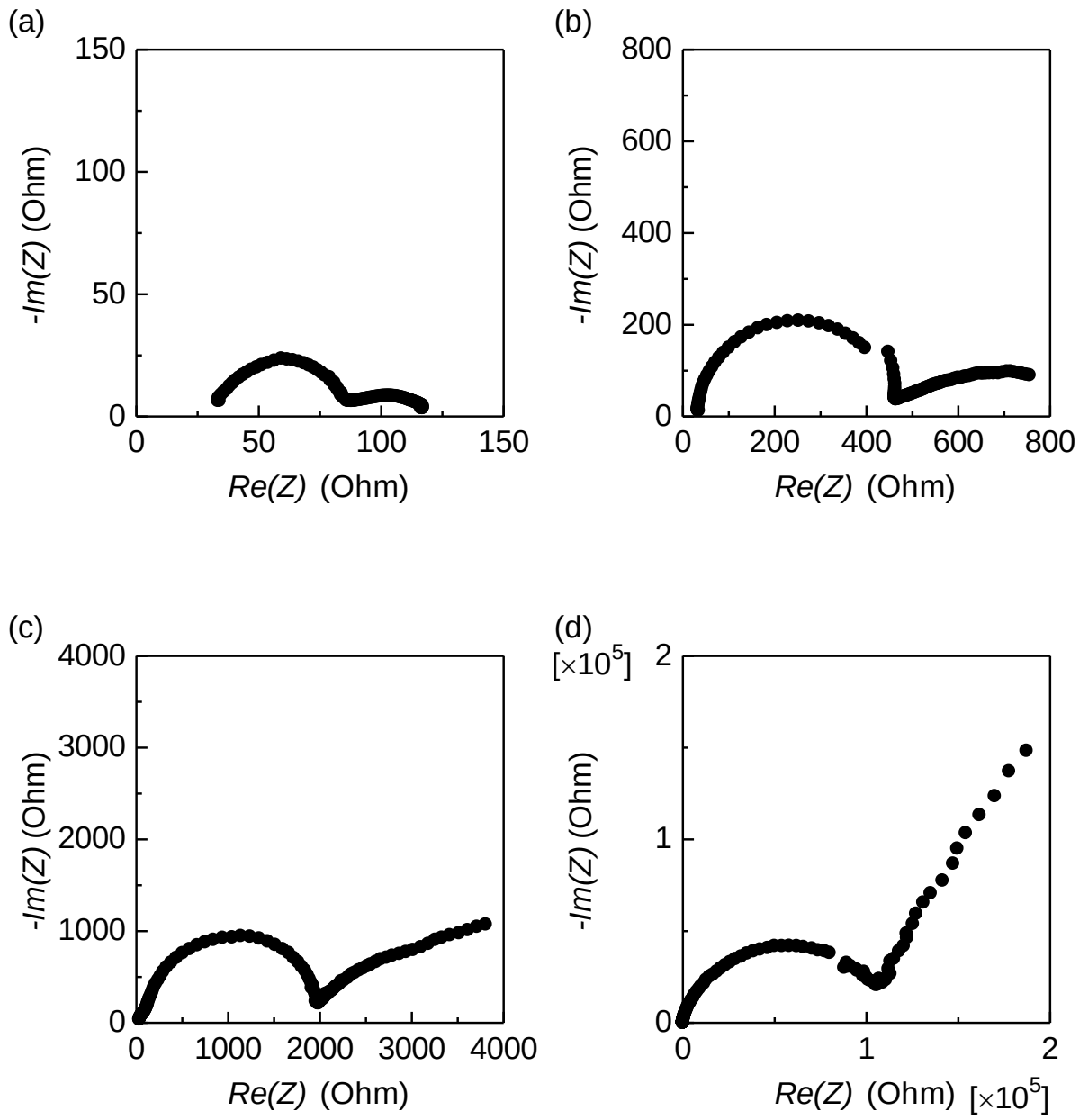

Figure 2.5 Nyquist plots of mesostructured perovskite solar cells under (a) 100 mW/cm^2, (b) 10 mW/cm^2, (c) 0.1 mW/cm^2, and (d) dark condition.

A TiO_2 layer is suggested to increase the internal resistance under low-illuminance conditions. TiO_2 is naturally as insulator material, but it shows conductivity by filling the trap site with carriers [7, 8]. Therefore, TiO_2 acts as a resistance under low-illuminance conditions that cannot generate enough carriers to fill the trap sites. Consequently, it is suggested that the planar structure eliminated the mp-TiO_2, which has many trap sites, is suitable for indoor applications.

The same investigation was carried out for planar-type PSCs. Figure 2.6 shows Nyquist plots of the planar type PSCs under 100 mW/cm^2 and 0.1 mW/cm^2 illuminations. The inset of Figure 2.6 (b) shows low-frequency part of Nyquist plot under 0.1 mW/cm^2 illumination. As shown in Figure 2.6 (b), the TL behavior was not observed in the planar type PSCs even under 0.1 mW/cm^2 illumination. These results indicate the electron transport resistance of planar type PSCs is lower than mesostructured PSCs under low-illuminance condition. Therefore, it is expected that planar type PSCs show better performance than mesostructured PSCs under low-illuminance conditions.

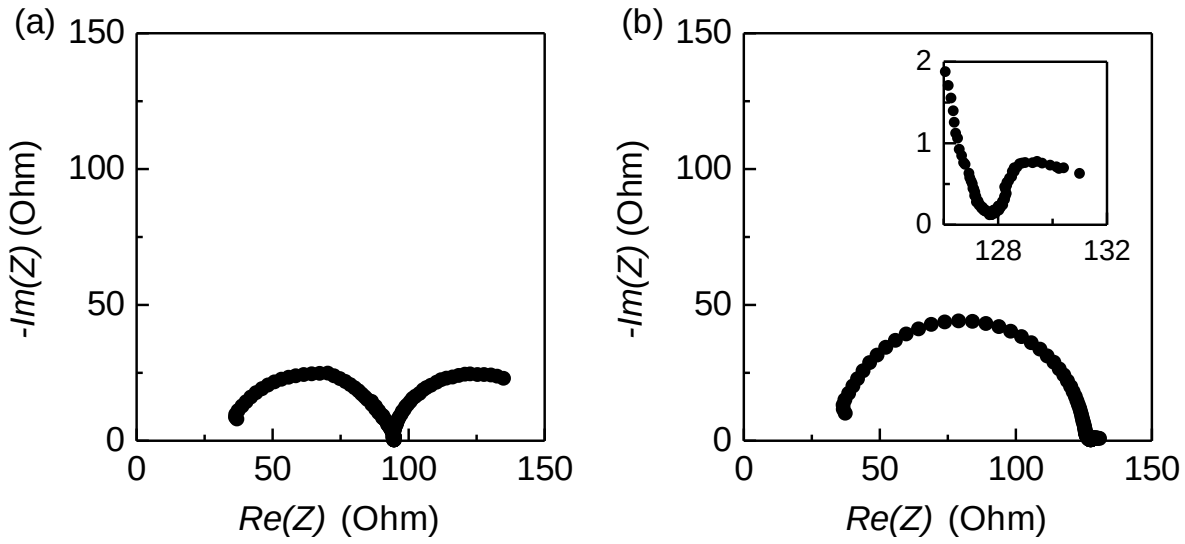

Figure 2.6 Nyquist plots of planar-type perovskite solar cells (a) 100 mW/cm^2 and (b) 0.1 mW/cm^2 illumination.

2.5 Influence of device structure on low-illuminance characteristics

J-V characteristics of planar type PSCs were investigated under various light intensities. Figure 2.7 (a) shows *J-V* curves of planar type PSCs under 100, 50, 10, 1, and 0.1 mW/cm^2 illuminance. As shown in Figure 2.7 (b), the J_{SC} value of planar type PSCs is in proportion to light intensity as well as mesostructured PSCs. Figure 2.7 (c) shows normalized V_{OC} of mesostructured and planar type PSCs under various light intensities. Planar type PSCs showed clearly higher normalized V_{OC} at low-illuminance conditions than that of mesostructured PSCs. The mesostructured and planar type PSCs showed an absolute V_{OC} value of 0.71 V and 0.84 V at 0.1 mW/cm^2 illumination, respectively. Figure 2.7 (d) shows the normalized EQE spectra of planar type PSCs under 0.25 and 0.0025 mW/cm^2 monochromatic lighting. The EQE spectra of planar type PSCs did not show a large change due to light intensity as well as mesostructured PSCs.

Shunt resistance (Rsh) and series resistance (Rs) of each solar cell were compared. Figure 2.8 shows Rsh and Rs of mesostructured and planar type PSCs under various light intensities. As shown in Figure 2.8 (a), the Rsh of each solar cell increased with decreasing light intensity. Also, the behavior was not different for each structure. By contrast, the Rs of the mesostructured PSCs increased remarkably than that of the planar type PSCs, indicating mp-TiO_2 is a resistance under low-illuminance conditions.

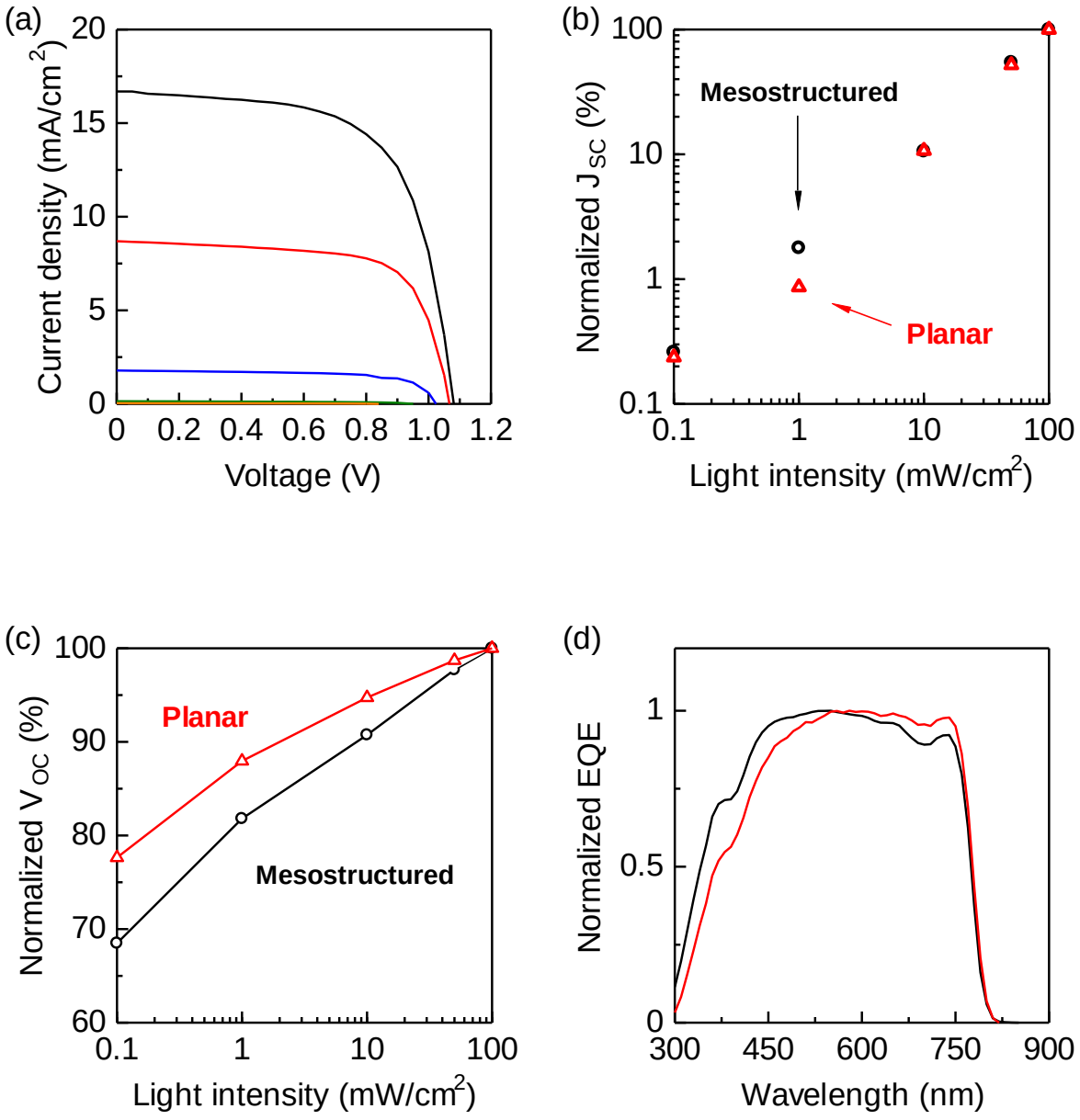

Figure 2.7 (a) *J-V* curves of planar-type perovskite solar cells. The black, red, blue, green, and orange lines represent the *J-V* curves under 100, 50, 10, 1, and 0.1 mW/cm^2 illumination, respectively. (b) Normalized J_{SC} and (c) Normalized V_{OC} of mesostructured and planar-type perovskite solar cells under various illuminance conditions. (d) Normalized EQE spectra of planar-type perovskite solar cells. The black and red lines represent the normalized EQE under 0.25 and 0.0025 mW/cm^2 illumination, respectively.

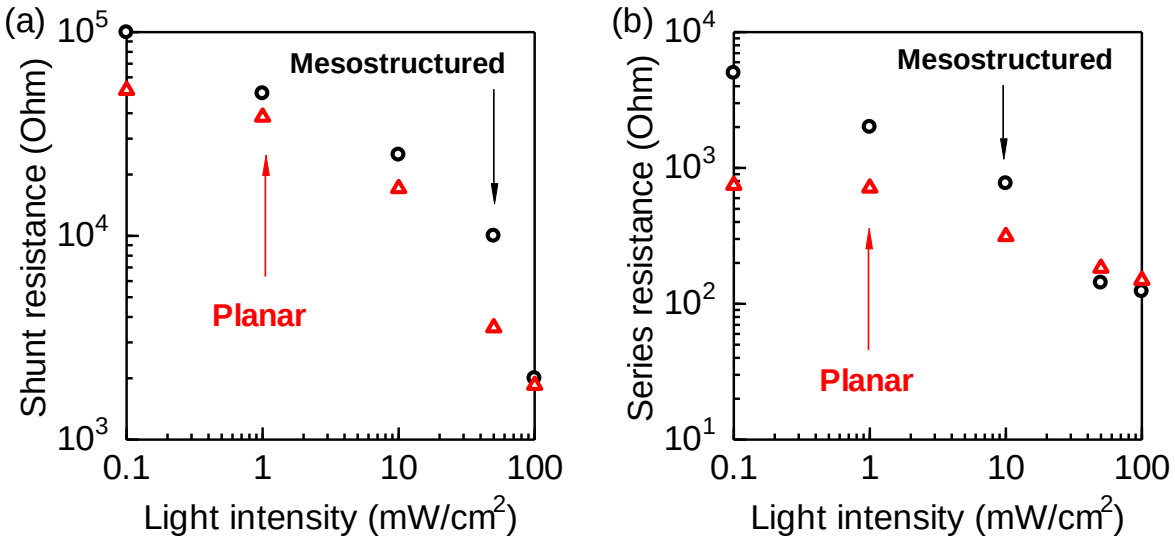

Figure 2.8 (a) Rsh and (b) Rs of mesostructured and planar-type perovskite solar cells under various illuminance conditions.

2.6 Summary

In this chapter, characteristics of PSCs were investigated under various light intensities with AM 1.5 spectrum. From the *J-V* measurement, it was clarified that PSCs can maintain higher V_{OC} value under low-illuminance conditions than a-Si solar cells, which has been used for indoor applications. Spectral sensitivity of PSCs was also investigated under low-illuminance conditions by EQE measurements. As a result, PSCs showed acceptable spectral response in wavelength range of 400-700 nm, which is included in typical indoor lighting such as white LED or fluorescent lamp. From impedance spectroscopy, it was considered that the mp-TiO_2 layer included in mesostructured PSCs acts as an internal resistance and decreases V_{OC} under low-illuminance conditions. Therefore, planar type PSCs were suggested as suitable device structure under low-

illuminance conditions and the *J-V* characteristics were evaluated. Planar type PSCs kept higher V_{OC} than mesostructured PSCs under low-illuminance conditions.

Results described in this chapter indicate an effective structural model of PSCs for low-illuminance applications and potential of PSCs for indoor applications, such as dispersed power sources for IoT applications.

References

[1] G. Aberle (1999). *Crystalline Silicon Solar Cells Advanced Surface Passivation and Analysis*. Centre for Photovoltaic Engineering, University of New South Wales.

[2] Luque and S. Hegedus (2011). *Handbook of Photovoltaic Science and Engineering*, 2nd ed. John Wiley & Sons, Ltd.

[3] V.-D. Dao, L. L. Larina, and H.-S. Choi, *Thin Solid Films* **593**, 10 (2015).

[4] Y. Rong, Z. Ku, A. Mei, T. Liu, M. Xu, S. Ko, X. Li, and H. Han, *J. Phys. Chem. Lett.* **5**, 2160 (2014).

[5] E. J. J.-Perez, M. Wuβler, F. F.-Santiago, K. L.-Wollny, E. Mankel, T. Mayer, W. Jaegermann, and I. M.-Sero, *J. Phys. Chem. Lett.* **5**, 680 (2014).

[6] J. A. Christians, R. C. M. Fung, and P. V. Kamat, *J. Am. Chem. Soc*. **136**, 758 (2014).

[7] A. Solbrand, A. Henningsson, S. Södergren, H. Lindstöm, A. Hagfeldt, and S.-E. Lindquist, *J. Phys. Chem. B* **103**, 1078 (1999).

[8] P.M. Sommeling, H.C. Rie!e, J.A.M. van Roosmalen, A. SchoK necker, J.M. Kroon, J.A. Wienke, and A. Hinsch, *Sol. Energ. Mater. Sol. C*. **62**, 399 (2000).

Chapter 3

Evaluation of Perovskite Solar Cells Under Ambient Lighting

3.1 Introduction

In Chapter 2, it was revealed that PSCs show very low voltage losses under low-illuminance conditions with standard solar spectrum AM 1.5. For IoT applications, it is supposed that PSCs will also be operated under indoor lighting such as fluorescent lamp or LED. However, emission spectra of indoor lightings are quite different from the standard spectrum. Thus, further investigations are needed to evaluate the potential of PSCs for indoor applications.

Typical indoor lightings do not show a spectrum in the wavelength range of over 700 nm [1]. Therefore, optimum band gap of light absorber is different from standard condition with AM 1.5 spectrum. In this chapter, cesium containing triple-cation perovskite materials, $Cs_{0.05}FA_{0.79}MA_{0.16}Pb(I_{0.84}Br_{0.16})_3$ (3-cat-Br16) and $Cs_{0.05}FA_{0.79}MA_{0.16}Pb(I_{0.50}Br_{0.50})_3$ (3-cat-Br50) (FA: formamidinium, MA: methylammonium) having different bandgap are used as light absorbers [2].

In the early investigation of PSCs, mono-cation perovskite, $MAPbI_3$ was mainly used as the light absorber. After PCE of $MAPbI_3$-based PSCs was saturated throughout various investigations, $FAPbI_3$, which has a smaller band gap than that of $MAPbI_3$, has attracted attention as an alternative

light absorber. However, $FAPbI_3$ transforms into a non-perovskite phase at room temperature [2]. On the other hand, an all-inorganic perovskite material such as $CsPbI_3$ have also investigated to overcome the instability of $MAPbI_3$. However, $CsPbI_3$ also becomes non-perovskite phase at room temperature [3]. Because of the phase instabilities, mixed-cation strategy becomes an important way to improve performance and stability of PSCs. Indeed, PSCs containing the triple-cation perovskite materials shows high PCE of over 20% and better stability than conventional PSCs including $MAPbI_3$ [4]. Moreover, triple-cation perovskite materials have less defect than mono cation perovskite which will lead lower V_{OC} loss [4]. Thus, I focused on triple-cation perovskite as light absorber of PSCs for indoor applications.

In this chapter, characteristics of PSCs under fluorescent lamp illumination are discussed. In section 3.3, optical property and morphology of triple-cation perovskite films are evaluated. In section 3.4, *J-V* characteristics of 3-cat-Br16 and 3-cat-Br50 based PSCs are evaluated under AM1.5 and fluorescent spectra. In section 3.5, phase segregation, which decreases the performance of bromide rich PSCs is discussed. In section 3.6, several measurements are carried out to discuss the effect of hysteresis on photovoltaics performance under low-illuminance conditions. In section 3.7, stability of 3-cat-Br16 PSCs under low-illuminance condition is described.

3.2 Experimental

3.2.1 Device fabrication of triple-cation perovskite solar cells

FTO coated glass substrates (8 Ohm/sq., Pilkington TEC8) were etched with zinc powder and 2 M HCl. The substrates were then rinsed with pure water, ethanol, and acetone. To prepare the

ETL, titanium diisopropoxide bis(acetylacetonate) (75 wt% in isopropanol, Sigma-Aldrich) diluted in ethanol (1:39, volume ratio) was sprayed on the FTO substrates at 475 °C. Then, the substrates were annealed at 475 °C for 30 min. A mp-TiO_2 layer was deposited on the ETL by spin-coating a TiO_2 paste (30 NR-D, GreatCell Solar Co.) diluted in ethanol (1:8, weight ratio) at 4000 rpm for 30 s. After spin coating, the substrates were annealed at 500 °C for 30 min. Perovskite layer was deposited by spin coating on the mesoporous TiO_2 layer in a two-step process. First, the substrates were accelerated to 2000 rpm for 10 s (200 rpm/s) and then spun at 5000 rpm for 20 s (2000 rpm/s). During the second step, 200 μL of chlorobenzene was dropped onto the rotating substrate at 5 s before the end of the spin-coating process. The composition of precursor solutions are shown in Table 3.1. After spin coating, the substrates were annealed at 100 °C for 1 h. Spiro-OMeTAD solution consisting same additives with Chapter 2, was spin-coated on the perovskite layer at 4000 rpm for 30 s to deposit a HTL. Finally, an Au electrode was deposited by thermal evaporation on the HTL.

3.2.2 Characterization

The *J-V* characteristics were measured under AM1.5 one sun illumination (100 mW/cm^2) with a solar simulator (Enli Tech, SS-F5 3A, Taiwan), calibrated by reference silicon solar cells (Enli Tech, SRC2000) and source meter (Keithley, 2401). The low-illuminance characteristics were measured under T5 fluorescent lamp illumination (200 lx, 65 μW/cm^2) with a source meter (Keithley 2420). Source meter (Keithley 2401) was used for stabilized measurements under fluorescent lamp illumination. The emission spectrum of the fluorescent lamp is shown in Figure 3.1. The active area of the samples was set as 0.16 cm^2. The EQE was measured with an EQE

measurement system (Newport Cornerstone 260). The absorption spectrum of perovskite films were measured with UV/VIS/NIR spectrophotometer (V-570, JASCO). The SEM images were obtained using the ultrahigh-resolution electron microscope Hitachi SU9000.

Table 3.1 The composition of perovskite precursor solution

	3-cat-Br16	3-cat-Br50
Formamidinium iodide	93.9 mg	98.6 mg
Methylammonim bromide	11.3 mg	11.9 mg
Lead iodide	264.5 mg	108.9 mg
Lead bromide	37.2 mg	173.4 mg
Cesium iodide (1.3 M DMSO solution)	25 μL	25 μL
DMF	400 μL	400 μL
DMSO	100 μL	100 μL

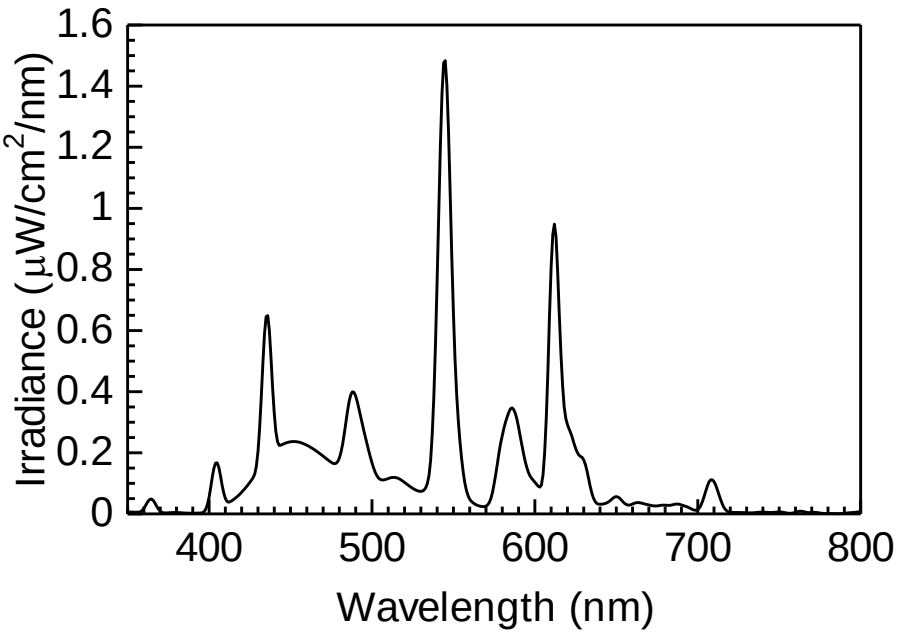

Figure 3.1 Emission spectrum of the T5 fluorescent lamp.

3.3 Characterization of triple-cation perovskite films

It is possible to control the bandgap of organic-inorganic perovskite compounds by changing the halogen ratio [5]. The bandgap of iodide based perovskite increases by increasing bromide ratio in the composition. Figure 3.2 shows absorption spectra of 3-cat-Br16 and 3-cat-Br50 perovskite films. The 3-cat-Br16 and 3-cat-Br50 perovskite films have absorption edge of 780 nm and 680 nm, respectively. Figure 3.3 shows SEM images of 3-cat-Br16 and 3-cat-Br50 perovskite films. There were no significant difference in morphology of both perovskite films.

3.4 Photovoltaic performance of triple-cation perovskite solar cells

3.4.1 Characterization under standard conditions

Figure 3.4 shows *J-V* curves of triple-cation PSCs measured under AM1.5G spectrum (1sun, 100 mW/cm^2). Under the 1sun condition, the highest PCE of 3-cat-Br16 PSCs was 15.8% with J_{SC} of 20.99 mA/cm^2, V_{OC} of 1.033 V, and fill factor (FF) of 0.730 in reverse scan. The highest PCE of 3-cat-Br50 PSCs was 9.9% with J_{SC} of 15.19 mA/cm^2, V_{OC} of 1.018 V, and FF of 0.639 in reverse scan. 3-cat-Br50 PSCs showed lower PCE than 3-cat-Br16 PSCs mainly due to lower J_{SC} arose from wider band gap. The photovoltaic performance of each PSCs are summarized in Table 3.2 and Table 3.3. Comparing both PSCs, 3-cat-Br50 PSCs showed poor FF and similar V_{OC} with 3-cat-Br16 PSCs although they have different bandgaps. This is probably due to phase segregation of bromide-rich perovskite films described in section 3.5.

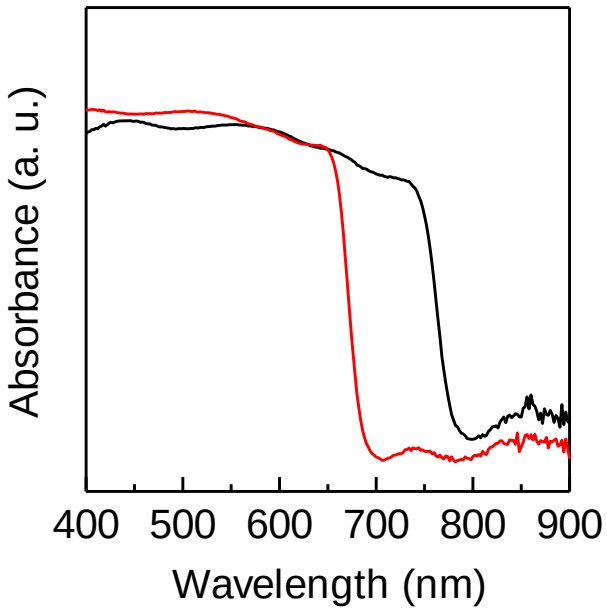

Figure 3.2 Absorption spectra of triple-cation perovskite films. The black and red lines represent absorption spectra of 3-cat-Br16 and 3-cat-Br50, respectively.

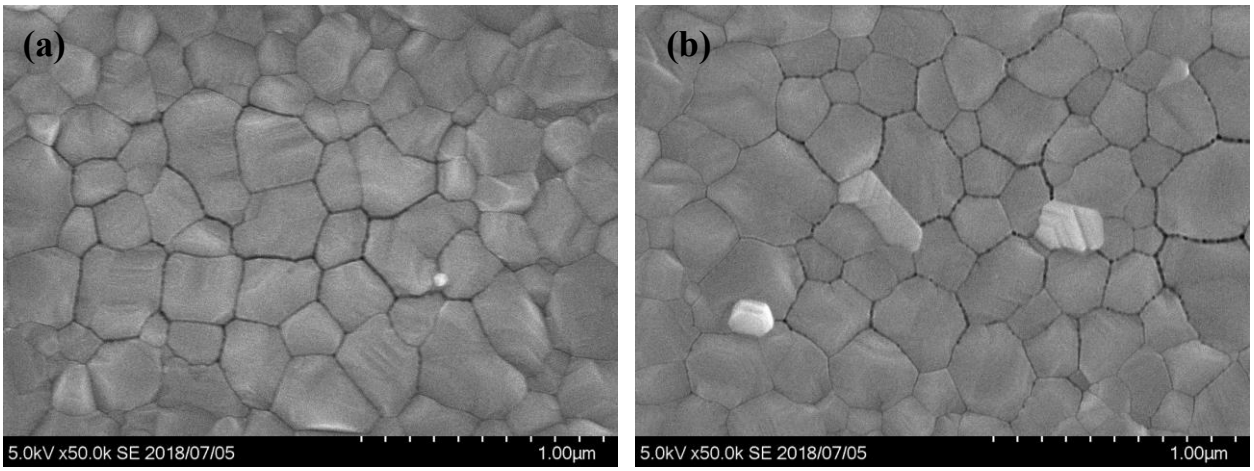

Figure 3.3 SEM images of (a) 3-cat-Br16 and (b) 3-cat-Br50 perovskite films.

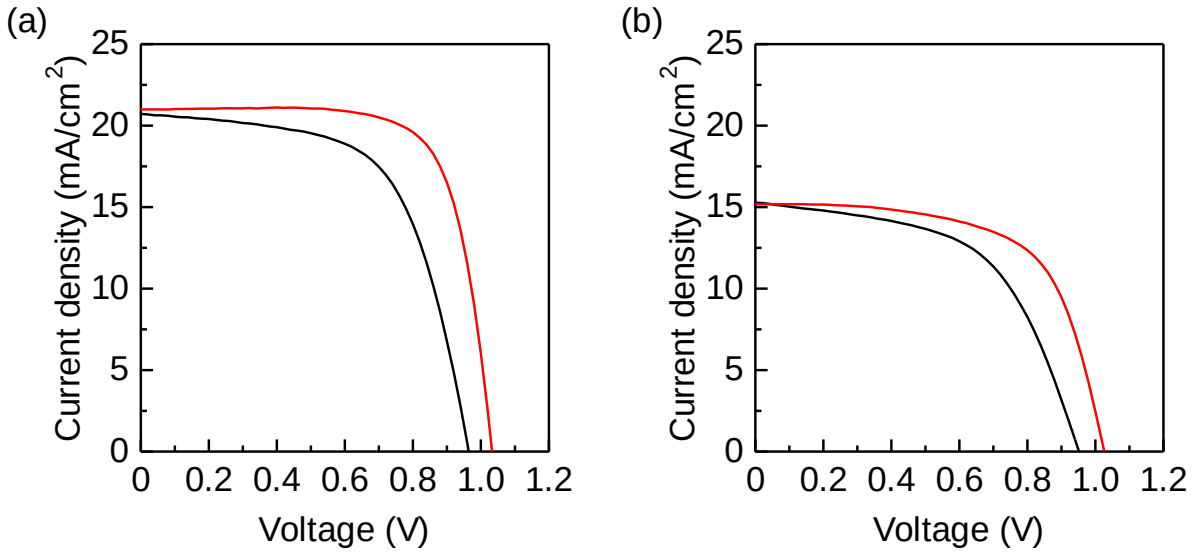

Figure 3.4 *J-V* curves of (a) 3-cat-Br16 and (b) 3-cat-Br50 perovskite solar cells measured under AM 1.5G illumination (100 mW/cm^2). The black and red lines represent the *J-V* curves from forward scan and reverse scan, respectively.

Table 3.2 *J–V* characteristics of 3-cat-Br16 perovskite solar cells under AM1.5 1 sun condition

	J_{SC} (mA/cm^2)	V_{OC} (V)	FF	PCE (%)
Forward	20.35±0.31 (20.72)	0.968±0.013 (0.964)	0.606±0.011 (0.612)	11.9±0.3 (12.2)
Reverse	20.68±0.30 (20.99)	1.032±0.014 (1.033)	0.709±0.010 (0.730)	15.1±0.3 (15.8)

Table 3.3 *J–V* characteristics of 3-cat-Br50 perovskite solar cells under AM1.5 1 sun condition

	J_{SC} (mA/cm^2)	V_{OC} (V)	FF	PCE (%)
Forward	14.67±0.39 (15.27)	0.963±0.069 (0.952)	0.559±0.037 (0.551)	7.9±0.9 (8.0)
Reverse	14.38±0.68 (15.19)	1.018±0.034 (1.026)	0.639±0.031 (0.634)	9.3±0.4 (9.9)

Figure 3.5 shows the EQE spectra of PSCs including 3-cat-Br16 and 3-cat-Br50. PSCs based on 3-cat-Br16 and 3-cat-Br50 showed EQE response extended to ~780 nm and ~680 nm, respectively. The EQE response is consistent with the absorption spectrum of each perovskite films (Fig. 3.2). Both PSCs showed similar EQE value within their absorption region.

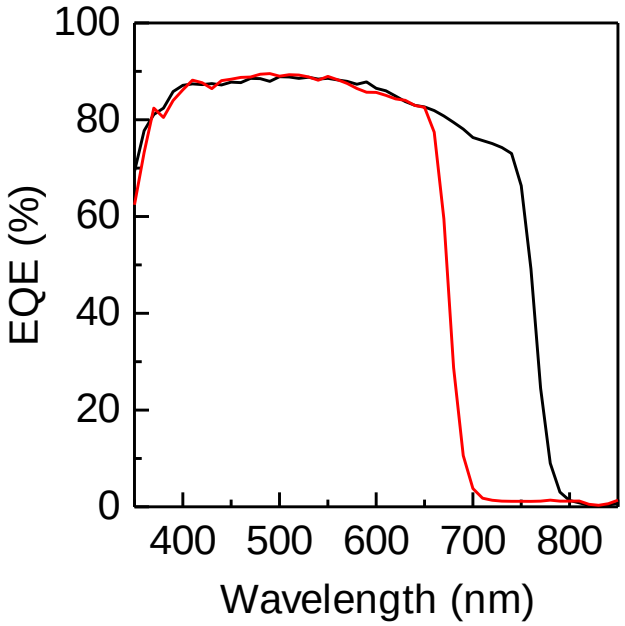

Figure 3.5 EQE spectra of triple-cation perovskite solar cells. The black and red lines represent EQE spectra of 3-cat-Br16 and 3-cat-Br50, respectively.

3.4.2 Characterization under low-illuminance conditions

Figure 3.6 (a) shows *J-V* curves of 3-cat-Br16 PSCs measured under fluorescent lamp illumination (200 lx, 65 μW/cm^2). Under 200 lx illumination, maximum output (P_{MAX}) of 17.6 μW/cm^2, corresponding to a PCE of 27.1 %, was confirmed with J_{SC} of 30.53 μA/cm^2, V_{OC} of 0.778 V, and FF of 0.742 in reverse scan.

Typically, PSCs with a bandgap of ~1.6 eV show high EQE from 400 nm to 800 nm [6-8]. However, common indoor lighting sources such as fluorescent lamp or LED do not include emission spectrum over 700 nm as shown in Figure 3.1. Therefore, tuning the band gap of perovskite materials is a promising method to improve the performance of PSCs under ambient lighting. Increasing the bandgap of perovskite materials will lead to higher V_{OC} without sacrificing J_{SC}. Figure 3.6 (b) shows *J-V* curves of 3-cat-Br50 PSCs measured under fluorescent lamp illumination. The 3-cat-Br50 PSCs showed a P_{MAX} of 19.7 μW/cm^2, which corresponds to a PCE of 30.3 % with J_{SC} of 31.02 μA/cm^2, V_{OC} of 0.815 V, and FF of 0.780. As expected, 3-cat-Br50 PSCs showed higher V_{OC} without decreasing J_{SC}. This is the first report that experimentally shows that band gap tuning is an effective strategy to improve the photovoltaic characteristics of PSCs under low-illuminance conditions. The *J-V* characteristics of both triple-cation PSCs measured under fluorescent lamp illumination are summarized in Table 3.4 and Table 3.5. To the best of my knowledge, these PCE values are the highest compared with the values, which have been reported so far as shown in Figure 3.7 [9-11].

Freunek *et al*. reported the theoretical PCE of the absorber having 1.8 eV bandgap exceeds 40% in the case of fluorescent lamp, suggesting the record PCE of over 30.3% has a still room to improve [12].

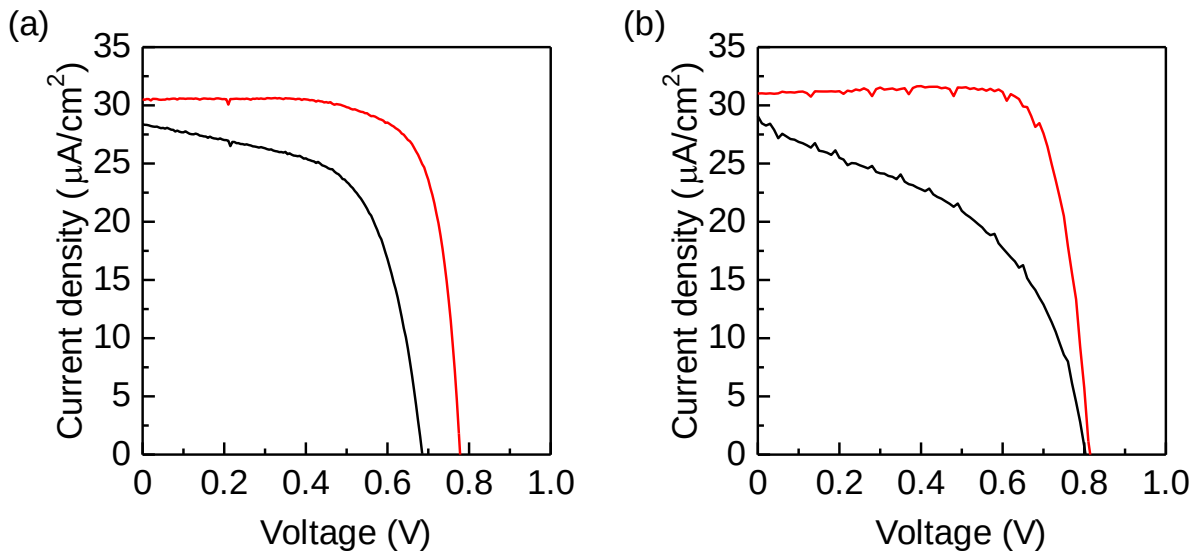

Figure 3.6 *J-V* curves of (a) 3-cat-Br16 and (b) 3-cat-Br50 perovskite solar cells measured under fluorescent lamp illumination (200lx, 65 μW/cm^2). The black and red lines represent the *J-V* curves from forward scan and reverse scan, respectively.

Table 3.4 *J–V* characteristics of 3-cat-Br16 perovskite solar cells under 200 lx illumination

	J_{SC} (μA/cm^2)	V_{OC} (V)	FF	P_{MAX} (μW/cm^2)	PCE (%)
Forward	27.67±0.52 (28.38)	0.680±0.011 (0.685)	0.619±0.011 (0.606)	11.6±0.4 (11.8)	17.9±0.6 (18.1)
Reverse	29.84±0.51 (30.53)	0.776±0.005 (0.778)	0.727±0.009 (0.742)	16.9±0.5 (17.6)	25.9±0.7 (27.1)

Table 3.5 *J–V* characteristics of 3-cat-Br50 perovskite solar cells under 200 lx illumination

	J_{SC} (μA/cm^2)	V_{OC} (V)	FF	P_{MAX} (μW/cm^2)	PCE (%)
Forward	26.80±1.35 (29.08)	0.818±0.057 (0.803)	0.527±0.039 (0.471)	11.6±1.5 (11.0)	17.8±2.2 (16.9)
Reverse	29.90±0.96 (31.02)	0.812±0.058 (0.815)	0.698±0.069 (0.780)	17.0±2.5 (19.7)	26.1±3.9 (30.3)

3.5 Phase segregation in mixed-halide perovskite

Commonly, solar cells consisting wider bandgap materials show higher V_{OC} than that of narrow bandgap materials. However, 3-cat-Br50 PSCs showed similar V_{OC} with 3-cat-Br16 PSCs under AM1.5G 1 sun condition. This phenomenon is attributed to phase segregation of mixed-halide perovskite materials. It was reported that mixed-halide perovskite shows phase segregation when subjected to light irradiation [13, 14]. As a result, iodine rich region and bromide rich region are separated in perovskite layer. Then, iodine rich region serves as charge recombination site to reduce V_{OC} and FF of PSCs. On the other hand, it was reported that phase segregation takes a longer time under dark condition [15]. From the report, it is considered that phase segregation occurs slower under low-illuminance condition than under AM1.5G 1 sun condition. Consequently, there is a possibility that phase segregation does not progress during measurement and lead to a higher V_{OC} and FF of 3-cat-Br50 PSCs under low-illuminance condition. In fact, it was found that 3-cat-Br50 perovskite films shows photoluminescence peak shift after exposure to AM1.5G 1 sun condition as shown in Figure 3.8. This tendency is consistent with previous reports on phase segregation of mixed-halide perovskite films [13, 14]. However, there are no reports on phase segregation under low intensity light illumination so that further investigation is required.

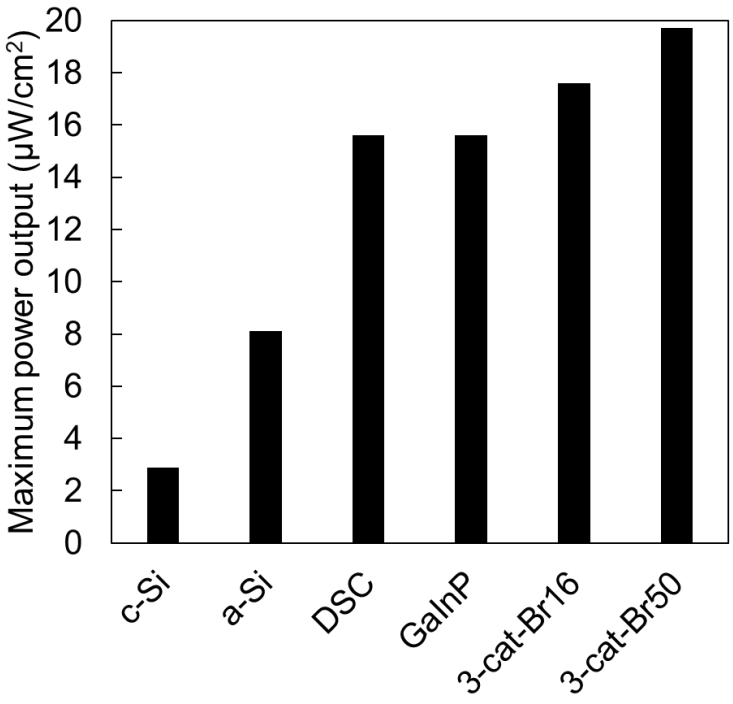

Figure 3.7 Maximum power output of various solar cells under 200 lx fluorescent lamp illumination.

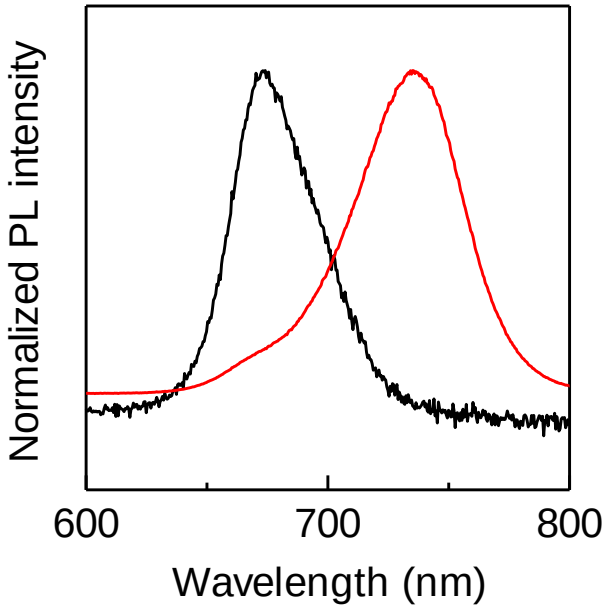

Figure 3.8 Normalized photoluminescence spectra of 3-cat-Br50 perovskite films. The black and red curves represent before and after light soaking (AM1.5G, 1 sun), respectively.

3.6 *J-V* hysteresis under low-illuminance condition

3.6.1 Stabilized efficiency

As described in section 1.3, it is widely known that PSCs show hysteresis, which means different *J-V* curves dependent on the scan direction. The origin of hysteresis has been discussed and some reasons have been suggested such as ferroelectric effect, ion migration, and capacitance effect [16-18]. In general, PSCs shows difference in V_{OC} and FF depending on the scan direction. However, there are differences in not only V_{OC} and FF but also J_{SC} particularly under low-illuminance condition. Stabilized measurement is one of an evaluation method to avoid the effect of hysteresis on the *J-V* characteristics.

Figure 3.9 shows a typical *J-V* curve of solar cells. PCE of solar cells is calculated by below equation;

$$\mathrm{PCE} = \frac{J_{SC} \times V_{OC} \times FF}{Incident\ power} \times 100\ [\%]$$

$$\mathrm{FF} = \frac{J_m \times V_m}{J_{SC} \times V_{OC}}$$

Where J_m and V_m are current density and voltage at P_{MAX} of the solar cells. Under 100 mW/cm^2 illumination, the above equations can be simplified as below;

$$\mathrm{PCE} = J_{SC} \times V_{OC} \times FF = J_m \times V_m$$

Therefore, PCE can be estimated by tracking the current value under applying bias voltage of V_m. In this method, the influence of hysteresis on photovoltaics performance of solar cells is ignorable.

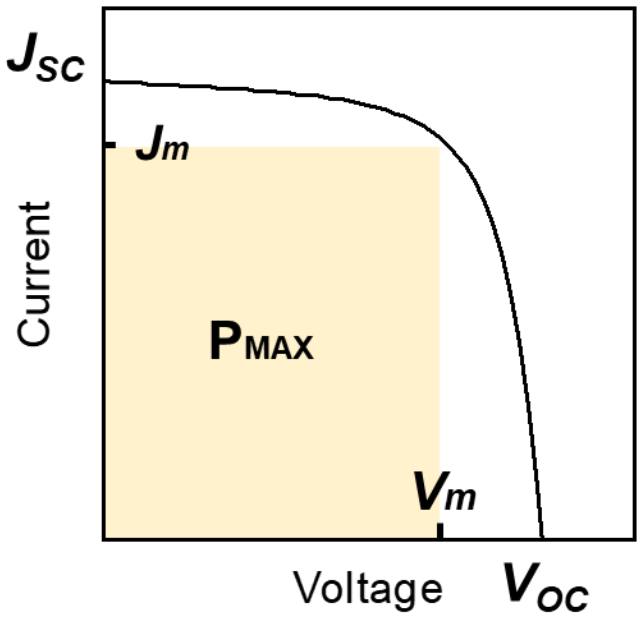

Figure 3.9 A typical *J-V* curve of solar cells.

Figure 3.10 (a) shows *J-V* curves of a 3-cat-Br16 PSCs measured under 200 lx illumination. The *J-V* characteristics are summarized in Table 3.6. Figure 3.10 (b) shows stabilized current density and PCE measured at a voltage at maximum power point of the sample (calculated from forward scan). The oscillation of stabilized current density is probably due to resolution of source meter. Although the stabilized PCE was smaller than that of from *J-V* curves, stable PCE was observed. Figure 3.10 (c) shows stabilized current density measured at 0 V. Stabilized J_{SC} was also smaller than the value from *J-V* curves. 3-cat-Br50 PSCs also showed similar behavior as shown in Figure 3.11 and Table 3.7.

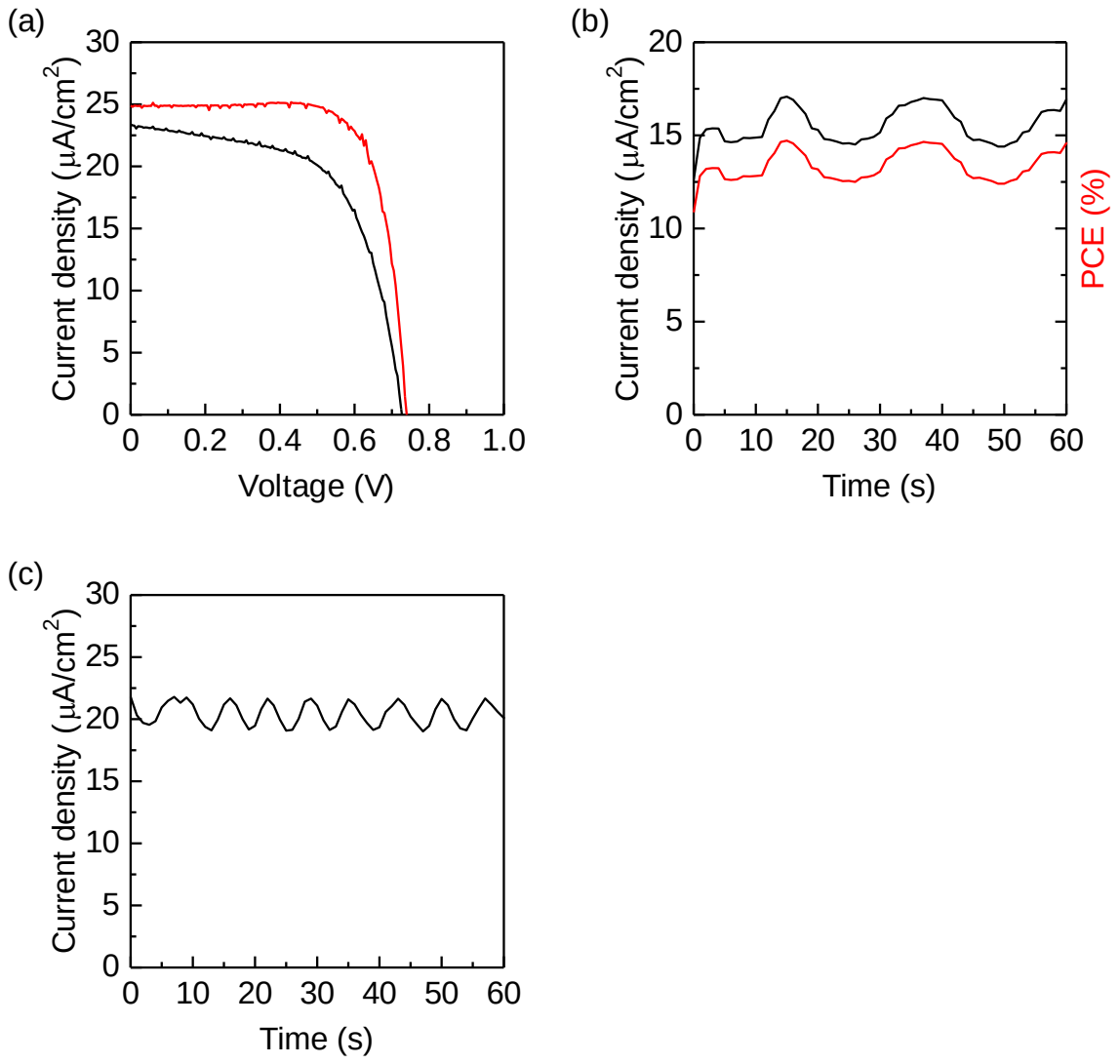

Figure 3.10 (a) *J-V* curves of a 3-cat-Br16 perovskite solar cells (PSCs). The black and red lines represent the *J-V* curves from forward scan and reverse scan, respectively. (b) Stabilized current density and power conversion efficiency (PCE) of the 3-cat-Br16 PSCs. The black and red lines represent stabilized current density and PCE, respectively. (c) Stabilized J_{SC} of the 3-cat-Br16 PSCs.

Table 3.6 *J–V* characteristics of 3-cat-Br16 perovskite solar cells used stabilized measurement

	J_{SC} (μA/cm^2)	V_{OC} (V)	FF	PCE (%)
Forward	23.38	0.727	0.614	16.0
Reverse	24.89	0.740	0.761	21.6

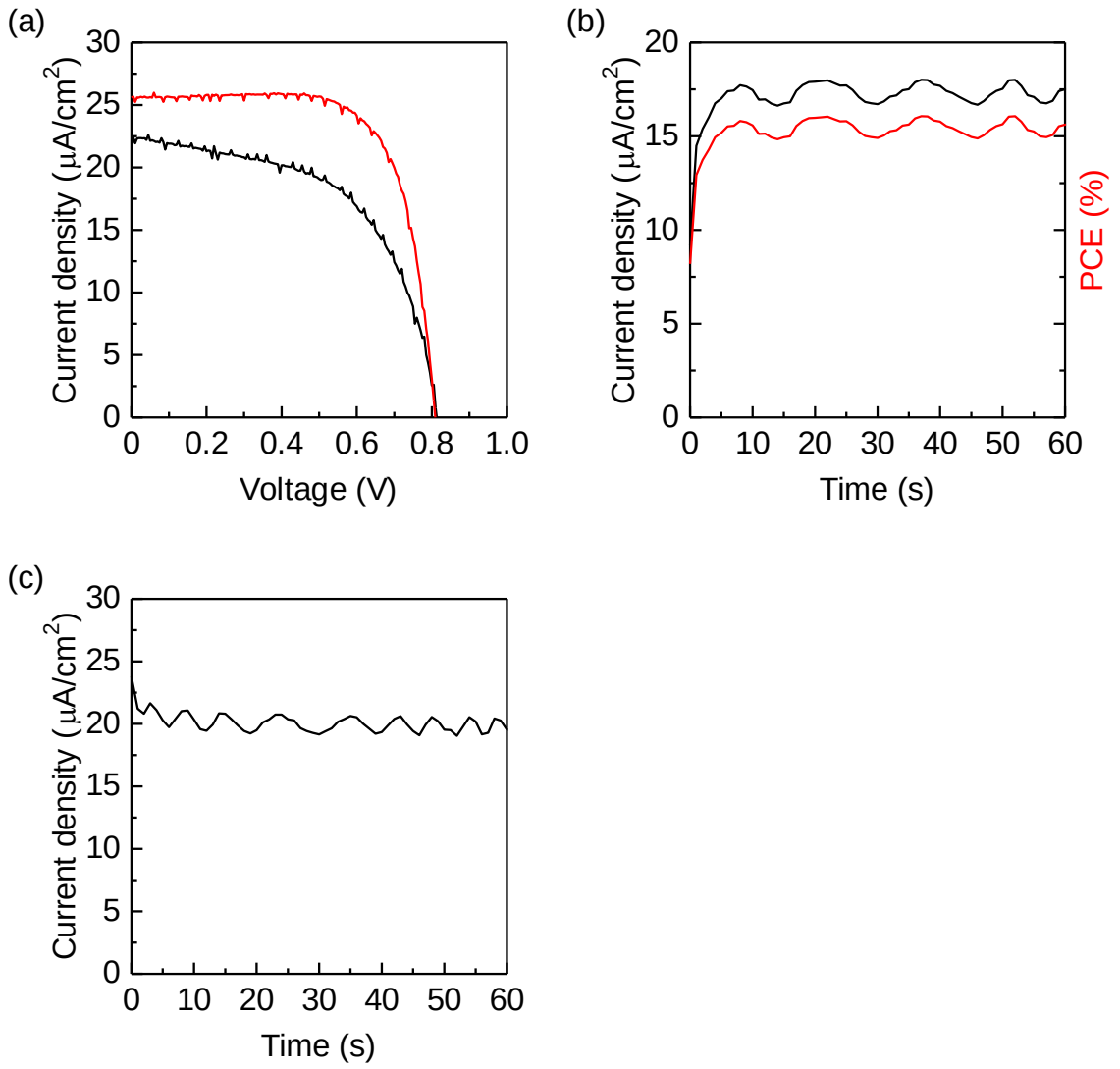

Figure 3.11 (a) *J-V* curves of a 3-cat-Br50 perovskite solar cells (PSCs). The black and red lines represent the *J-V* curves from forward scan and reverse scan, respectively. (b) Stabilized current density and power conversion efficiency (PCE) of the 3-cat-Br50 PSCs. The black and red lines represent stabilized current density and PCE, respectively. (c) Stabilized J_{SC} of the 3-cat-Br50 PSCs.

Table 3.7 *J–V* characteristics of 3-cat-Br50 perovskite solar cells used stabilized measurement

	J_{SC} (μA/cm^2)	V_{OC} (V)	FF	PCE (%)
Forward	22.55	0.813	0.574	16.2
Reverse	25.59	0.809	0.714	22.8

3.6.2 Light intensity dependence

There is a report on performance of PSCs under various light intensities [19]. It is reported that the J_{SC} calculated from *J-V* curves was not proportional to light intensity under ultra-low light intensity (< 10 μW/cm^2) due to capacitive current. J_{SC} value become higher than proportional value and it leads overestimate of the device performance. Although the condition (65 μW/cm^2) in this chapter is higher light intensity than such condition, there is no evidence that there is no capacitive effect in *J-V* curves in this chapter. Further investigation is mandatory to evaluate accurately the potential of PSCs for indoor applications.

Light intensity dependence on PCE of PSCs are evaluated under AM 1.5G (0.01 sun to 1 sun) and fluorescent lamp (200, 400, and 600 lx) illumination. Figure 3.12 (a) shows PCE of 3-cat-Br16 PSCs measured under various light intensities with AM 1.5 G spectrum. It was confirmed that the J_{SC} value is proportional to light intensity between 0.01 to 1 sun conditions as shown in Figure 3.12 (b). 3-cat-Br50 PSCs showed same behavior with 3-cat-Br16 PSCs as shown in Figure 3.13.

Figure 3.14 (a) shows *J-V* curves of 3-cat-Br50 PSCs measured under 200, 400, and 600 lx with fluorescent lamp. The J_{SC} value is also proportional to light intensity even under 200-600 lx conditions that seems there are less influence of such capacitive effect in *J-V* curves.

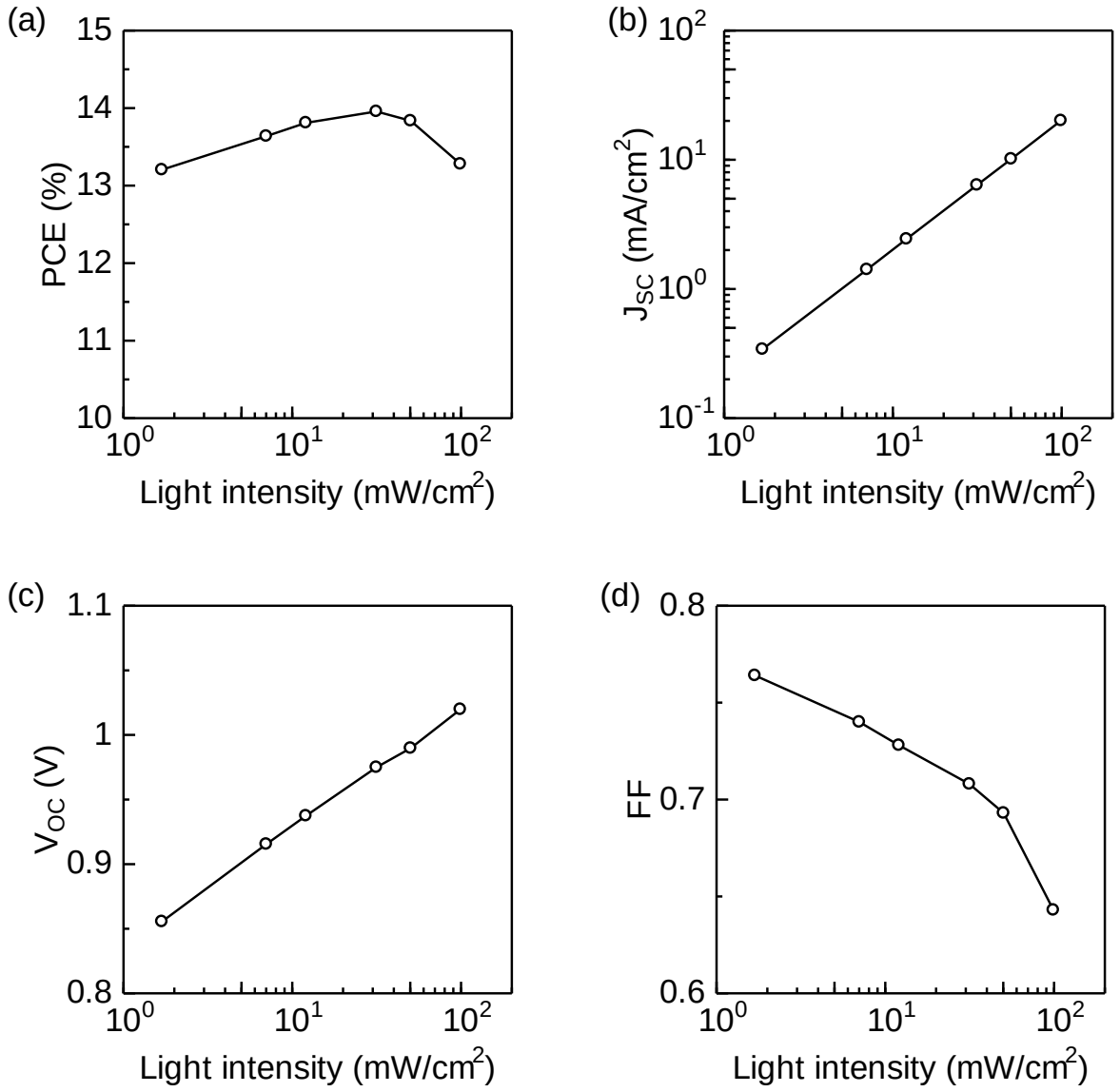

Figure 3.12 Light intensity dependence on photovoltaics performance of 3-cat-Br16 perovskite solar cells.

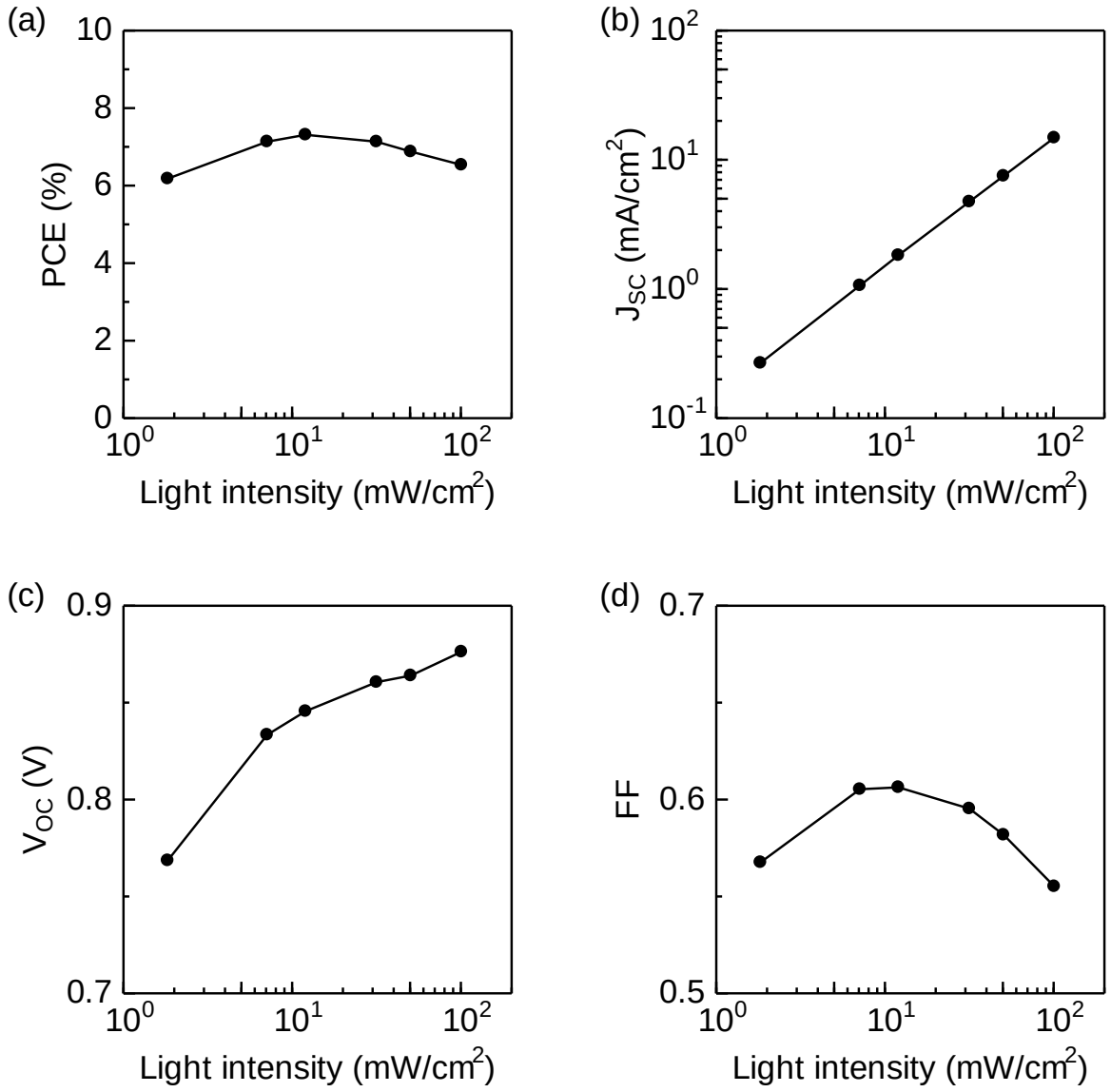

Figure 3.13 Light intensity dependence on photovoltaic performance of 3-cat-Br50 perovskite solar cells.

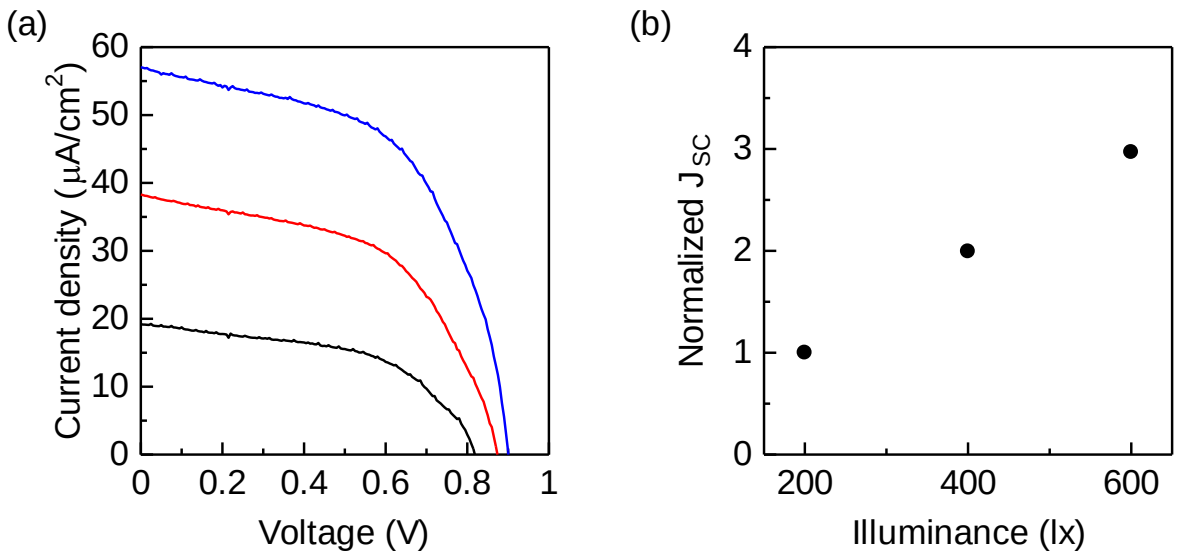

Figure 3.14 (a) *J-V* curves of 3-cat-Br50 perovskite solar cells under various light intensities with fluorescent lamp illumination. The black, red, and blue lines represent *J-V* curves measured under 200, 400, and 600 lx, respectively. (b) J_{SC} value of the sample. The J_{SC} value is normalized using J_{SC} at 200 lx.

3.7 Stability of perovskite solar cells under low-illuminance condition

Stability issue is one of the problems in PSCs. In this section, stability of 3-cat-Br16 PSCs are investigated using sealed PSCs (Figure 3.15). The sealing was carried out by fixing glass cover on the PSCs using UV curing resin. Figure 3.16 (a) shows the PCE of sealed PSCs after storage under ambient condition with room temperature and in dark. PSCs retained 93% of its initial efficiency after being stored for 672 h. This result indicates there is a possibility that PSCs can operate long-term under indoor conditions. After being stored in 72 h, the PCE increased with increasing V_{OC} and FF then decreased with decreasing all parameters. The increasing of V_{OC} and FF in the first 72 h might be attributed to improvement of hole conductivity of spiro-OMeTAD arose from oxidation by Li dopant [20, 21]. Changes in V_{OC}, FF and J_{SC} are shown in Figure 3.16 (b), (c), and (d), respectively. *J-V* curves before and after storage are shown in Figure 3.17.

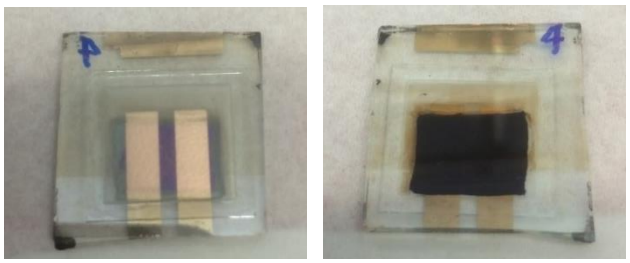

Figure 3.15 Photographs of sealed perovskite solar cells used for stability test.

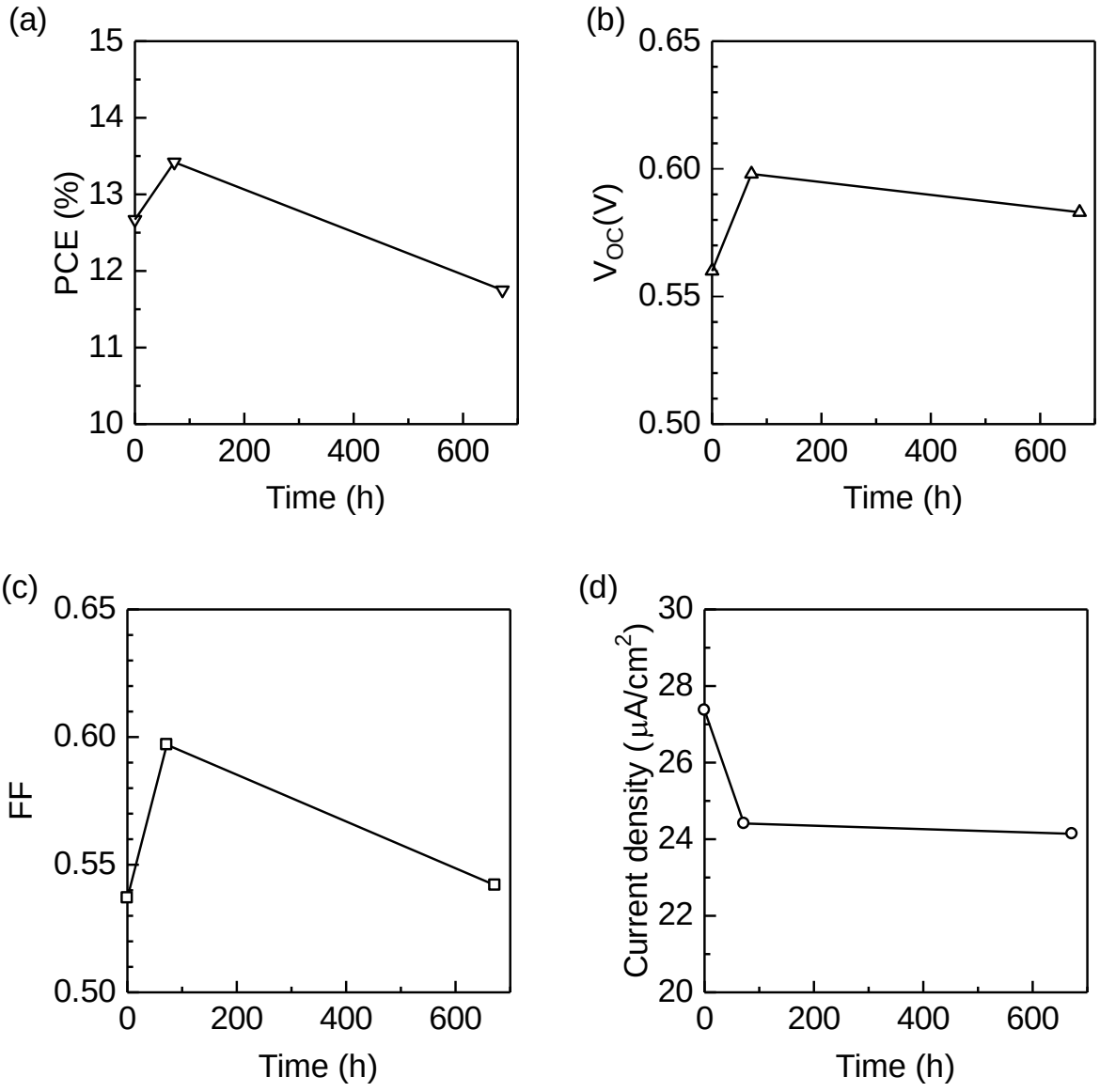

Figure 3.16 *J-V* characteristics of 3-cat-Br16 perovskite solar cells under 200 lx illumination during stability test. The photovoltaic characteristics were calculated from the forward scan.

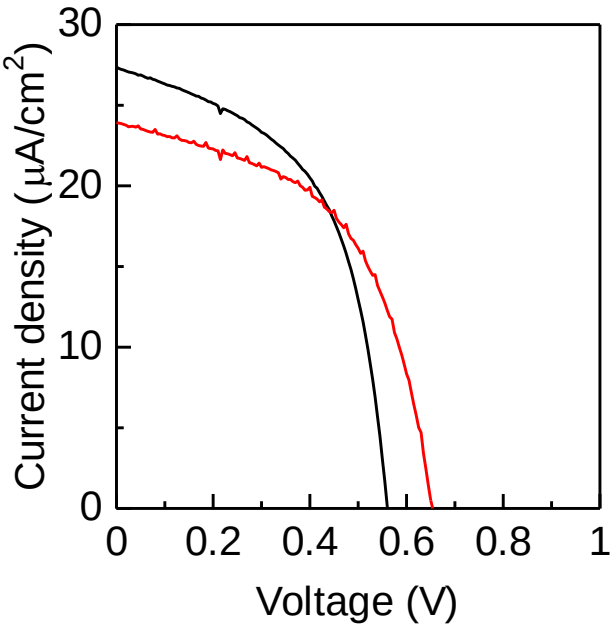

Figure 3.17 *J-V* curves of 3-cat-Br16 perovskite solar cells stored under ambient condition. The black and red lines represent before storage and after storage for 672 h, respectively. The *J-V* curves were taken by forward scan.

3.8 Summary

In this chapter, characteristics of PSCs were investigated under fluorescent lamp illumination, which is one of the indoor lightings. It was confirmed that 3-cat-Br16 PSCs, which have optimum band gap for AM 1.5 spectrum showed PCE of 27.1% under 200 lx condition. In addition, 3-cat-Br50 PSCs, which of band gap was tuned, showed PCE of over 30% under 200 lx illumination. These values are highest compared with that of other kind of solar cells under similar light intensities. Commonly, bromide rich PSCs shows lower photovoltaics performance due to form recombination site in perovskite layer under 1 sun condition. Results described in this chapter indicate the phase segregation affect slight influence on photovoltaic performance under low-

illuminance conditions. From stability test, PSCs stored under ambient condition showed 93% of its initial PCE after being stored 672 h.

Results described in this chapter indicate PSCs can work effectively even under spectrum of indoor lighting such as fluorescent lamp. In addition, PSCs showed better stability under low-illuminance condition that of under 1 sun condition. These results indicate PSCs is promising candidate for dispersed power sources for IoT applications.

References

[1] C.-Y. Chen, J.-H. Chang, K.-M. Chiang, H.-L. Lin, S.-Y. Hsiao, and H.-W. Lin, *Adv Funct. Mater.* **25**, 7064 (2015).

[2] J.-W. Lee, D.-J. Seol, A.-N. Cho, and N.-G. Park, *Adv. Mater.* **26**, 4991 (2014).

[3] P. Luo, W. Xia, S. Zhou, L. Sun, J. Cheng, C. Xu, and Y. Lu, *J. Phys. Chem. Lett.* **7**, 3603 (2016).

[4] M. Saliba, T. Matsui, J.-Y. Seo, K. Domanski, J.-P. C.-Baena, M. K. Nazeeruddin, S. M. Zakeeruddin, W. Tress, A. Abate, A. Hagfeldt, and M. Grätzel, *Enery Emvron. Sci.* **9**, 1989 (2016).

[5] D. P. McMeekin, G. Sadoughi, W. Rehman, G. E. Eperon, M. Saliba, M. T. Hörantner, A. Haghighirad, N. Sakai, L. Korte, B. Rech, M. B. Johnston, L. M. Herz, H. J. Snaith, *Science* **351**, 151 (2016).

[6] W. S. Yang, B.-W. Park, E. H. Jung, N. J. Jeon, Y. C. Kim, D. U. Lee, S. S. Shin, J. Seo, E. K. Kim, J. H. Noh, S. I. Seok, *Science* **356**, 1376 (2017).

[7] N. J. Jeon, J. H. Noh, Y. C. Kim, W. S. Yang, S. Ryu, and S. I. Seok, *Nature Materials* **13**, 897 (2014).

[8] X. Yin, Z. Yao, Q. Luo, X. Dai, Y. Zhou, Y. Zhang, Y. Zhou, S. Luo, J. Li, N. Wang, and H. Lin, *ACS Appl. Mater. Interfaces* **9**, 2439 (2017).

[9] Y. Li, N. J. Grabham, S. P. Beeby, and M. J. Tudor, *Solar Energy* **111**, 21 (2015).

[10] Mathews, P. J. King, F. Stafford, and R. Frizzell, *IEEE Journal of Photovoltaics* **6**, 230 (2016).

[11] M. Freitag, J. Teuscher, Y. Saygili, X. Zhang, F. Giordano, P. Liska, J. Hua, S. M. Zakeeruddin, J.-E. Moser, M. Grätzel, and A. Hagfeldt, *Nature Photonics* **11**, 372 (2017).

[12] M. F. Muller, M. Freunek, and L. M. Reindl, *IEEE J. Photovolt.* **3**, 59 (2013).

[13] S. J. Yoon, S. Draguta, J. S. Manser, O. Sharia, W. F. Schneider, M. Kuno, and P. V. Kamat, *ACS energy Lett.* **1**, 290 (2016).

[14] E. T. Hoke, D. J. Slotcavage, E. R. Dohner, A. R. Bowring, H. I. Karunadasa, and M. D. McGehee, *Chem. Sci*. **6**, 613 (2015).

[15] A. Sadhanala, F. Deschler, T. H. Thomas, S. E. Dutton, K. C. Goedel, F. C. Hanusch, M. L. Lai, U. Steiner, T. Bein, P. Docampo, D. Cahen, and R. H. Friend, *J. Phys. Chem. Lett.* **5**, 2501 (2014).

[16] J. Wei, Y. Zhao, H. Li, G. Li, J. Pan, D. Xu, Q. Zhao, and D. Yu, *J. Phys. Chem. Lett*. **5**, 3937 (2014).

[17] T. Zhang, H. Chen, Y. Bai, S. Xiao, L. Zhu, C. Hu, Q. Xue, and S. Yang, *Nano Energy* **26**, 620 (2016).

[18] L. Cojocaru, S. Uchida, P. V. V. Jayaweera, S. Kaneko, J. Nakazaki, T. Kubo, and H. Segawa, *Chem. Lett*. **44**, 1750 (2015).

[19] L. Cojocaru, S. Uchida, K. Tamaki, P. V. V. Jayaweera, S. Kaneko, J. Nakazaki, T. Kubo, and H. Segawa, *Sci. Rep*. **7**, 11790 (2017).

[20] X. Zhao and N.-G. Park, *Photonics* **2**, 1139 (2015).

[21] Q. Luo, Y. Zhang, C. Liu, J. Li, N. Wang, and H. Lin, *J. Mater. Chem. A* **3**, 15996 (2015).

Chapter 4

Fabrication of Perovskite Solar Cells Using Sputter Processed Perovskite Films

4.1 Introduction

In Chapter 2 and Chapter 3, great potential of PSCs for low-illuminance applications were demonstrated. However, reproducibility should be solved to expand the use of PSCs. Due to the major fabrication process of PSCs is spin-coating using anti-solvent dropping, which is carried out by human hand, large area and reproducibility are still being challenges. In this chapter, sputtering which is one of vacuum process is suggested as a novel fabrication process of PSCs.

One of the merits of sputtering process is that can fabricate homogeneous films on a large scale. Actually, a part of sputter processed transport layer based PSCs show acceptable photovoltaic performance with good reproducibility [1-3]. Another merit of sputtering is step coverage of deposited films. It is reported that sputtering process can deposit homogeneous films on textured substrates such as random pyramid textured substrates, which is difficult to form uniform films by solution process [4]. Usually, PSCs are formed on non-textured substrates such as FTO or ITO. However, to achieve high efficiency solar cells, textured substrates are necessary to reduce optical losses [5, 6]. If it became possible to fabricate PSCs on textured substrates, higher efficient PSCs will be obtained under both outdoor and indoor conditions.

In this chapter, fabrication process of perovskite films via sputtering process is suggested and the characteristics are evaluated. In section 4.2, fabrication process of typical perovskite compounds for PSCs is suggested. In section 4.3, crystal structure, optical characteristics, and morphology of sputter processed perovskite films are evaluated with X-ray diffraction (XRD) measurement, optical spectroscopy in UV-visible region, and SEM observation. In section 4.4, planar type PSCs are fabricated with sputter processed perovskite films and the photovoltaic performance is evaluated. In section 4.5, the morphology of sputter processed perovskite films deposited on random-pyramid-textured Si substrates is described.

4.2 Experimental

4.2.1 Fabrication process of $CH_3NH_3PbI_3$ films via sputtering

Perovskite films were obtained by reacting sputtered PbI_2 films and CH_3NH_3I gas as shown in Figure 4.1. The PbI_2 sputtering target was prepared from PbI_2 powder (Sigma-Aldrich, purity 99.999%) by pressing under 10 MPa on a stainless plate. Then, PbI_2 films were deposited on glass substrates by RF sputtering using the PbI_2 target. The sputtering conditions were Ar atmosphere under 1 Pa at room temperature with an RF power of 20 W. To obtain perovskite films, sputtered PbI_2 films were annealed at 100 °C in a CH_3NH_3I-gas-filled petri dish.

4.2.2 Solar cells fabrication

PSCs were fabricated by similar protocol with Chapter 2. FTO coated glass substrates (AGC Fabritech, thickness: 1.8 mm) were etched with zinc powder and 2 M HCl. The etched substrates were then washed with detergent and acetone in an ultrasonic bath for 10 min. Then, UV/O_3 treatment was carried out for 15 min at 115 °C. To prepare ETL, 0.15 M titanium diisopropoxide bis(acetylacetonate) (Sigma-Aldrich, 75 wt% in isopropanol) in 1-butanol was spin-coated on a FTO glass substrate at 700 rpm for 8s, 1000 rpm for 10 s, and 2000 rpm for 40 s, which was followed by drying at 125 °C for 5 min. After drying, the substrate was annealed at 450 °C for 1 h. Then, perovskite layer was deposited on the ETL following the above procedure. A spiro-OMeTAD solution consisting same additives with Chapter 2 was spin-coated on the perovskite layer at 1000 rpm for 4 s and 4000 rpm for 26 s to form a HTL. Finally, an Au electrode was deposited by thermal deposition on the HTL.

4.2.3 Characterization

The sputter processed perovskite films were characterized by SEM observation, XRD measurement, and absorption spectroscopy. SEM images were obtained using the ultrahigh-resolution electron microscope (Hitachi SU9000). The XRD measurements were performed using Rigaku RINT-TTR III with Cu Kα radiation. The absorption spectra were obtained using the UV-vis-NIR spectrophotometer (JASCO V-570). The *J-V* characteristics were measured under AM1.5 1 sun illumination (100 mW/cm^2) The EQE was measured under 0.25 mW/cm^2 monochromatic

lighting. *J-V* and EQE measurements were carried out using the EQE system (Bunkoukeiki Co., CEP-2000RR).

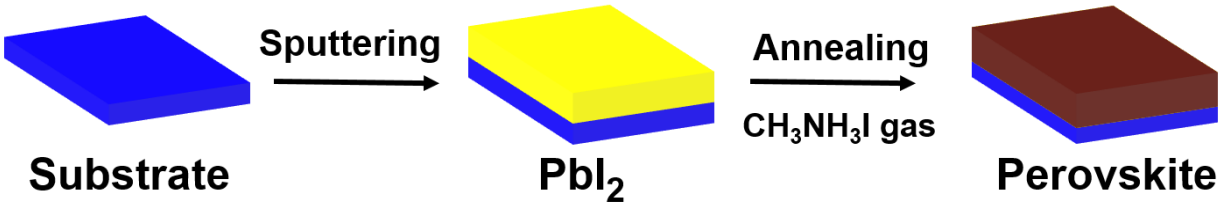

Figure 4.1 Process flow for the fabrication of perovskite films via sputtering process.

4.3 Characterization of sputter processed perovskite films

Figure 4.2 (a) shows the XRD pattern of the sputtered PbI_2 film. The sputtered PbI_2 films showed a strong diffraction peak at around 12°, which is assigned to the (001) facet of PbI_2 crystal. Figure 4.2 (b) shows the XRD pattern of a perovskite film fabricated by sputtering and annealing a PbI_2 film in CH_3NH_3I gas. Sputter processed perovskite films showed a strongest peak at around 14°, which is a typical diffraction pattern of $CH_3NH_3PbI_3$ perovskite films. In addition, sputter processed films had peaks similar to those of solution processed perovskite films shown in Figure 4.2 (c). Also, residual PbI_2 peaks were not observed in the XRD pattern. I also tried to fabricate perovskite films using perovskite powder, which was obtained by mixing PbI_2 and CH_3NH_3I powder, as a sputtering target. Figure 4.2 (d) shows the XRD pattern of perovskite films fabricated from a perovskite sputtering target. Although diffraction patterns of $CH_3NH_3PbI_3$ perovskite were obtained without annealing the films, there were some diffraction patterns of PbI_2, which might have been caused by plasma damage. In this chapter, perovskite films fabricated from the sputtered

PbI_2 films were investigated in more detail. Detail of perovskite films fabricated from perovskite powder are summarized in Appendix.

Figure 4.3 (a) shows an absorption spectrum of a sputter processed perovskite film. The film has an absorption edge at a wavelength of around 800 nm. Figure 4.3 (b) shows a Tauc plot of the sputter processed perovskite film. From the Tauc plot, the band gap of sputter processed perovskite films is around 1.6 eV, which is consistent with typical solution processed $CH_3NH_3PbI_3$ films [7].

Figure 4.4 (a) shows an SEM image of a sputter processed perovskite film. As shown in Figure 4.4 (a), the substrate was entirely covered with perovskite grains. In addition, there were no pinholes, which induce low photovoltaic performance in the perovskite film. Comparing with a solution processed film, relatively larger grain size was observed as shown in Figure 4.4 (b).

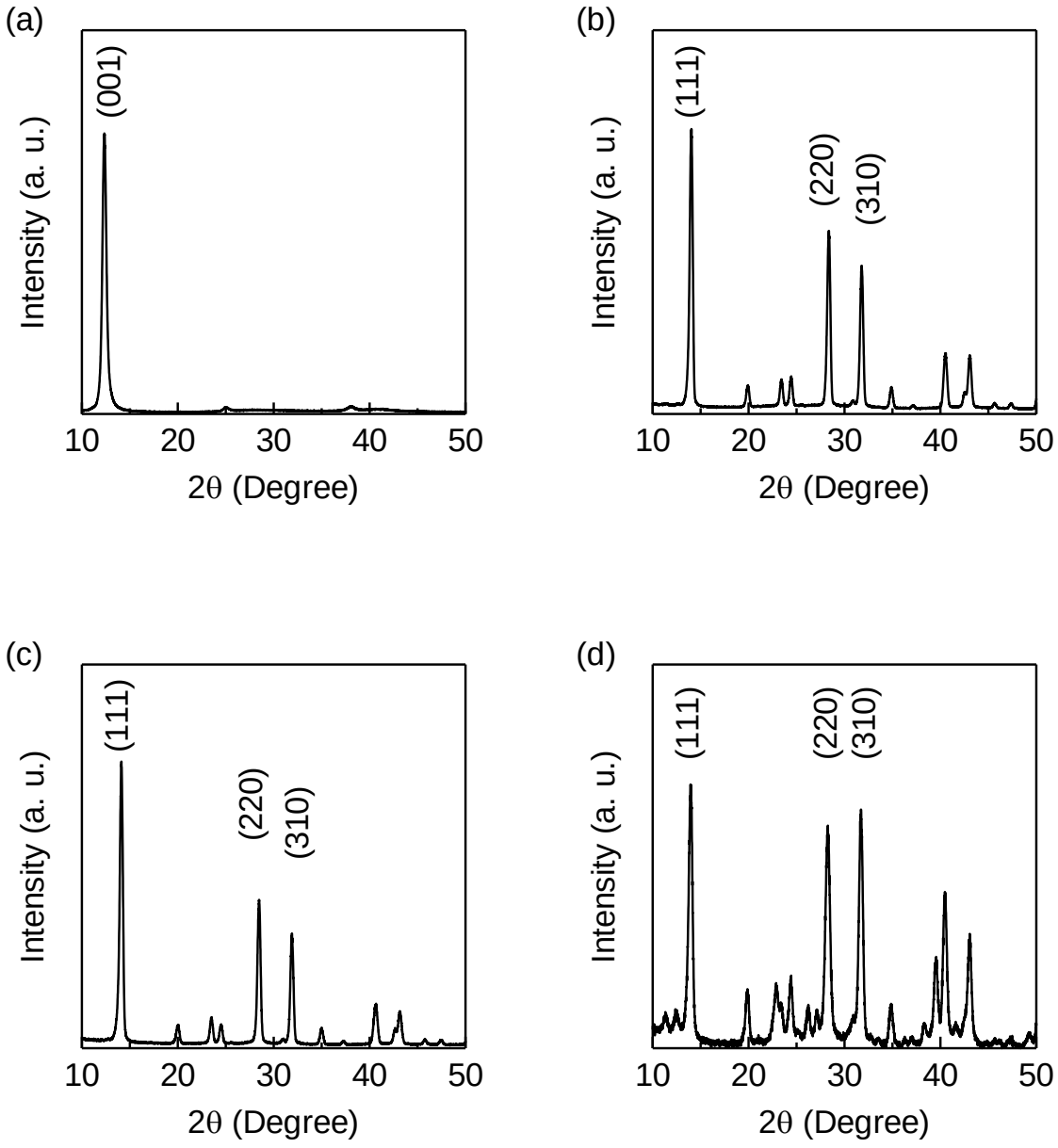

Figure 4.2 XRD patterns of (a) sputter processed PbI_2 film, (b) sputter processed $CH_3NH_3PbI_3$ perovskite film, (c) solution processed $CH_3NH_3PbI_3$ perovskite film, and (d) sputter processed $CH_3NH_3PbI_3$ perovskite films using a perovskite powder target.

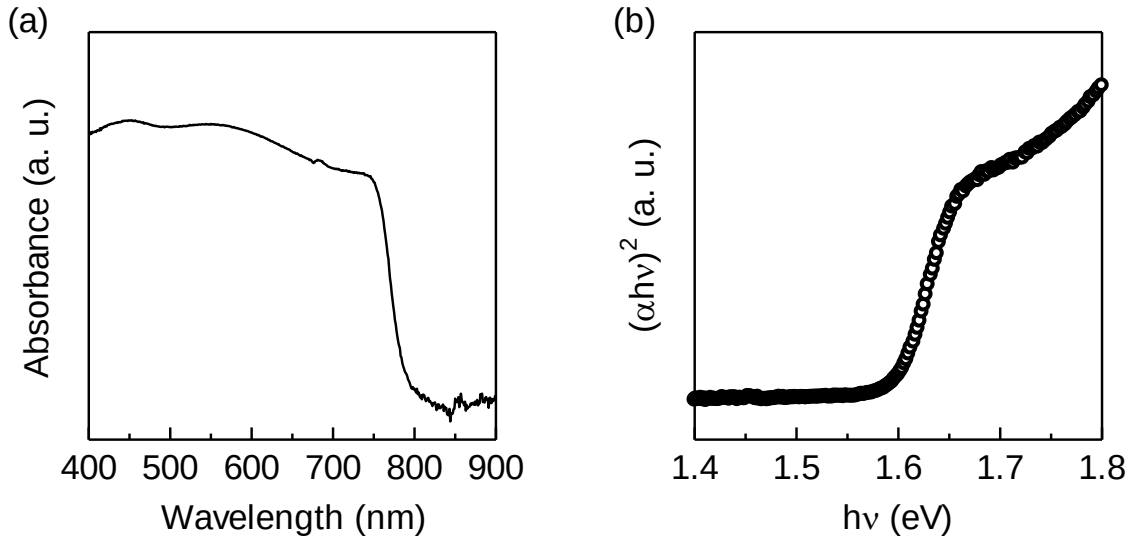

Figure 4.3 (a) absorption spectrum and (b) Tauc plot of sputter processed $CH_3NH_3PbI_3$ perovskite film.

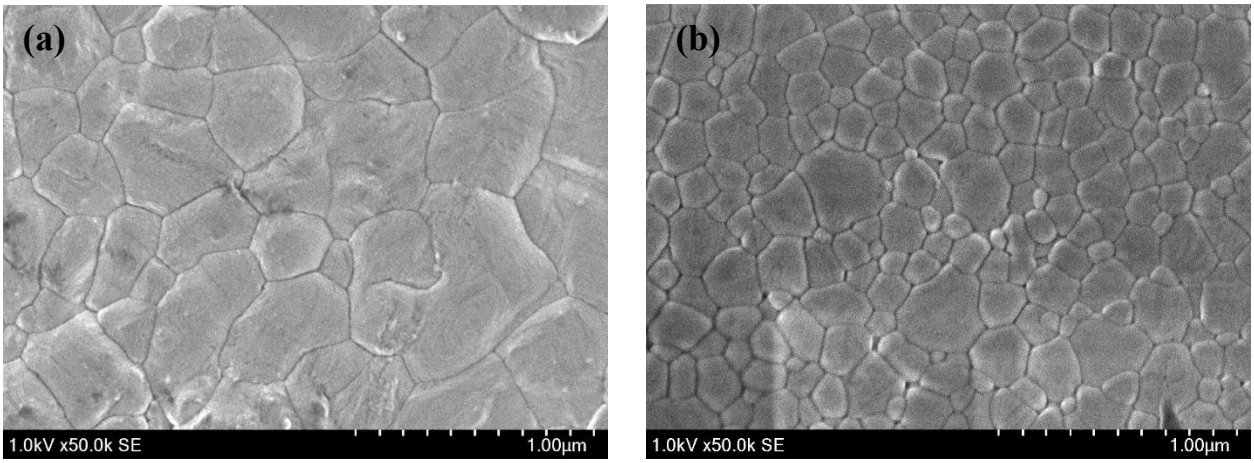

Figure 4.4 SEM images of (a) sputter and (b) solution processed $CH_3NH_3PbI_3$ perovskite films.

4.4 Solar cell application of sputter processed perovskite films

Sputter processed $CH_3NH_3PbI_3$ films were applied as light absorbing layer of PSCs. The TiO_2 layer and Spiro-OMeTAD layer were deposited by spin-coating as same as conventional PSCs to eliminate the influence of fabrication process. Figure 4.5 shows the *J-V* curves of the best performing solar cell. Photovoltaic performance was successfully obtained from the PSCs that include sputter processed perovskite films as shown in Figure 4.5. This is the first report on sputter processed perovskite films worked as light absorbing layer of PSCs. The *J-V* characteristics are summarized in Table 4.1. In forward scan, a PCE of 1.02% with a J_{SC} of 3.41 mA/cm^2, V_{OC} of 0.649 V, and FF of 0.460 was obtained. In reverse scan, a PCE of 1.84% with J_{SC} of 3.61 mA/cm^2, V_{OC} of 0.813 V, and FF of 0.628 was obtained.

Although sputtered perovskite films showed photovoltaic performance, the PCE is lower than that of conventional PSCs. Particularly, J_{SC} value is 5 to 6 times lower than conventional PSCs (see Table 2.1). EQE of sputter processed PSCs was evaluated. Figure 4.6 shows the EQE spectra of sputter processed PSCs measured under various bias voltages. The J_{SC} value from EQE spectrum measured without a bias voltage was 2.46 mA/cm^2, which was similar value with that of from *J-V* curve. However, when a bias voltage of -0.5 V was applied during the EQE measurement, the J_{SC} value from the EQE spectra was markedly enhanced from 2.46 to 9.25 mA/cm^2. This enhancement indicates that many carriers are lost in the absorber by recombination. Thus, it is expected that the *J-V* characteristics of PSCs including sputter processed films could be improved by optimizing the conversion process from PbI_2 to perovskite films.

One possible route to enhance the reaction of PbI_2 and CH_3NH_3I is controlling the density of PbI_2 films. There is a report on effect of the PbI_2 density on photovoltaic performance [8]. In the

report, perovskite films are fabricated by reacting spin-coated PbI_2 films and CH_3NH_3I solution. The PCE of resulted PSCs were enhanced from 1.51% to 10.67% by decreasing the density of PbI_2 films. The lower density PbI_2 films react with CH_3NH_3I gas easier than dense PbI_2 films. It leads uniform perovskite films and enhance the performance of PSCs. In sputtering process, the density of sputtered films can be controlled by sputtering conditions [9]. From a Thornton model, pressure and substrate temperature during sputtering affect the morphology of sputtered films. Therefore, it is expected that film density of sputtered PbI_2 films can be controlled by changing those sputtering conditions. Another route is reaction of PbI_2 films and CH_3NH_3I gas under low-pressure conditions. It is possible to achieve faster vapor diffusion rate and lower sublimation temperature of CH_3NH_3I under low-pressure conditions. It leads shorter reaction time for perovskite film formation and provide uniform perovskite films [10-12]. It is expected that photovoltaic performance of sputter processed PSCs will be improved by combining above strategies.

Table 4.1 *J-V* characteristics of a best performing solar cell

Direction	J_{SC} (mA/cm^2)	V_{OC} (V)	FF	PCE (%)
Forward	3.41	0.649	0.460	1.02
Reverse	3.61	0.813	0.628	1.84

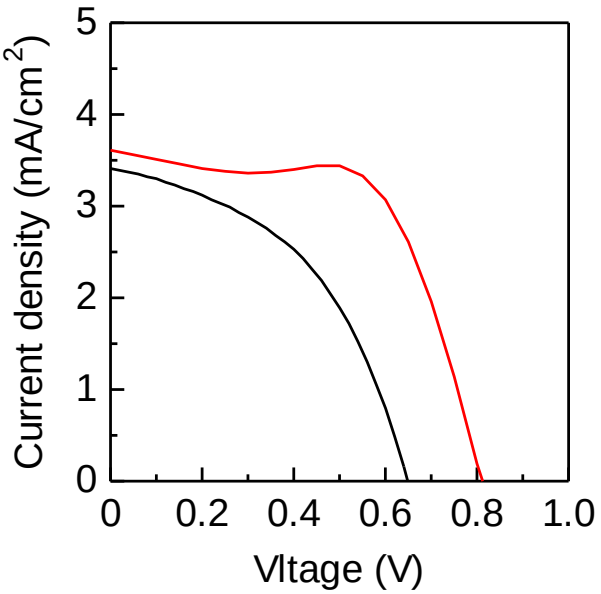

Figure 4.5 *J-V* curves of best performing perovskite solar cells including sputter processed perovskite film. The black and red line represent *J-V* curves recorded during forward scan and reverse scan, respectively.

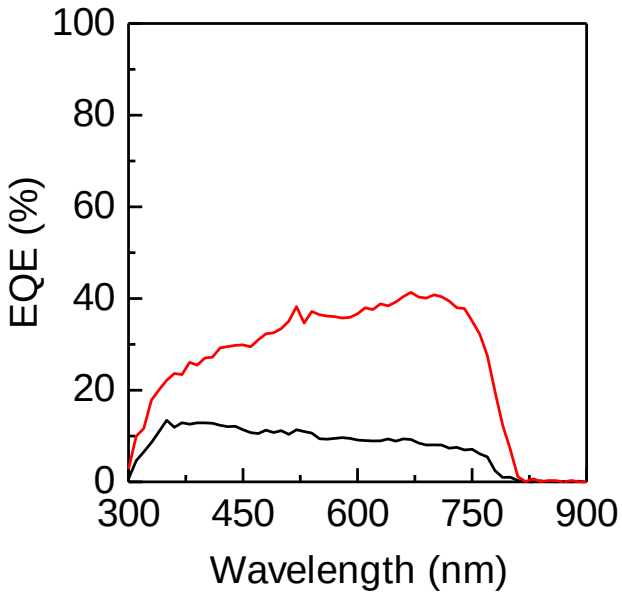

Figure 4.6 External quantum efficiency (EQE) spectra of best performing perovskite solar cells. The black and red lines represent EQE spectra measured without and with a bias voltage of -0.5 V, respectively.

4.5 Morphology of sputter processed perovskite films deposited on textured substrates

Figure 4.7 (a) shows a cross-sectional SEM image of a solar cell using sputter processed perovskite films. From the cross-sectional SEM image, it can be confirmed that a sputter processed perovskite film has homogeneous interface between the perovskite layer and the Spiro-OMeTAD layer. In addition, the bottom side of the perovskite film has a similar morphology with those of the FTO substrate and TiO_2 layer. Figure 4.7 (b) shows a cross-sectional SEM image of a PbI_2 film sputtered on TiO_2 layer. These results indicate that homogeneous PbI_2 and/or perovskite films can be fabricated by sputtering even if the substrates have a nanometer-scale roughness.

To confirm the morphology of sputter processed PbI_2 and perovskite films fabricated on substrates with a micrometer-scale roughness, these films were fabricated on random-pyramid-textured Si substrates. Figure 4.8 shows the cross-sectional images of the PbI_2 film sputtered on the textured Si substrate. As shown in Figure 4.8 (a), the films thickness of sputter processed films were uniform even when it located on top and between the pyramid structures. In addition, it was confirmed that pyramid surface is entirely covered with sputtered PbI_2 as shown in Figure 4.8 (b). Sputtered perovskite films showed same tendency as shown in Figure 4.9. These results indicate various kinds of substrates are available for sputter processed PSCs.

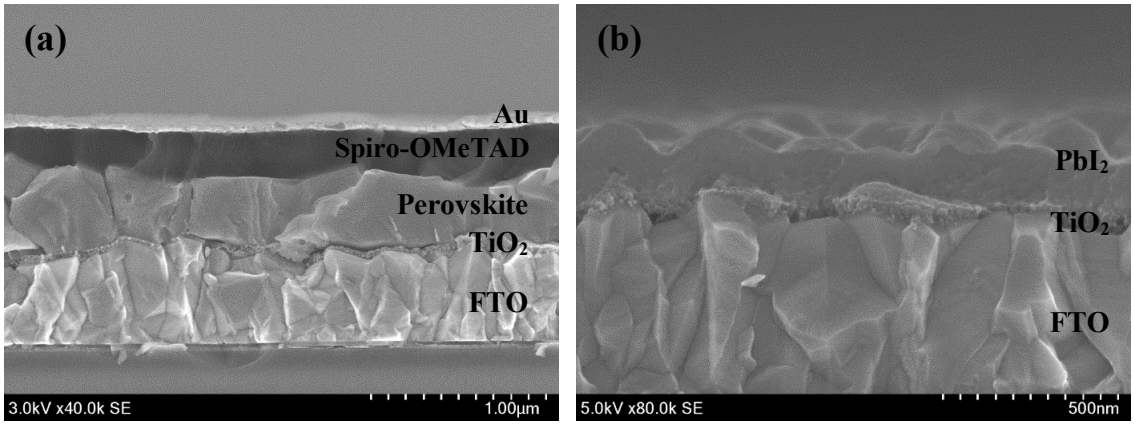

Figure 4.7 Cross-sectional SEM images of (a) completed solar cell and (b) PbI_2 film sputtered on a FTO/TiO_2 substrate.

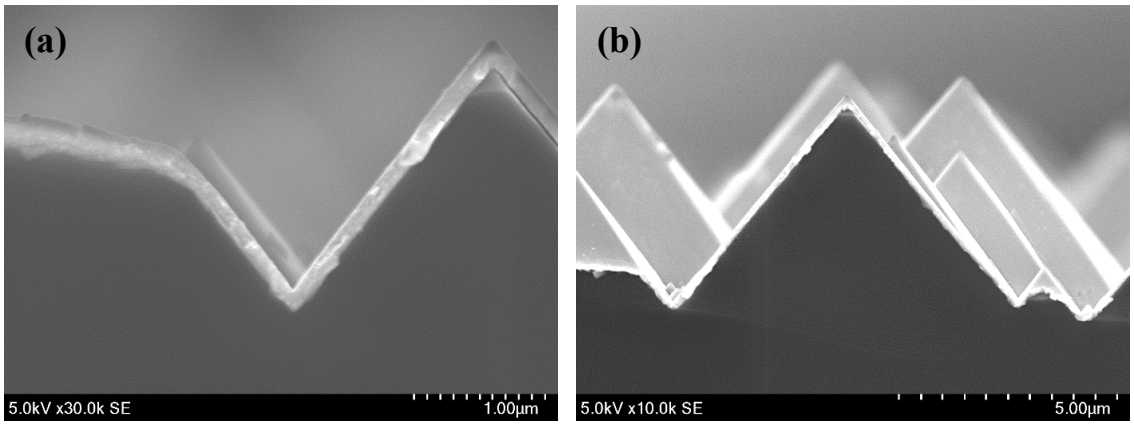

Figure 4.8 PbI_2 films sputtered on random-pyramid-textured Si substrates.

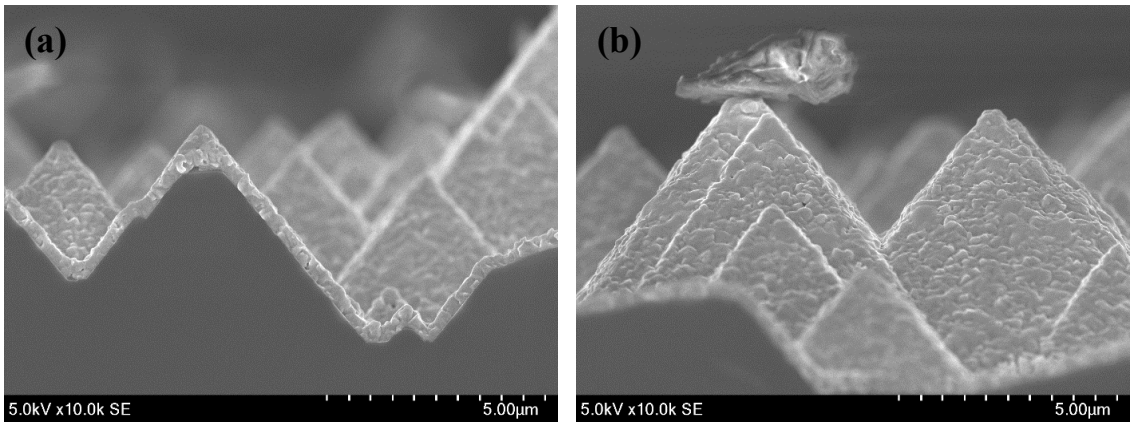

Figure 4.9 Sputter processed perovskite films deposited on random-pyramid-textured Si substrates.

4.6 Summary

In this chapter, sputtering process was suggested as novel fabrication process of PSCs and the sputter processed perovskite films and PSCs were evaluated. From the XRD measurement and UV/vis spectroscopy, it was confirmed that $CH_3NH_3PbI_3$ perovskite films could be synthesized from sputtered PbI_2 films. After sputtering process for perovskite films have been established, PSCs were fabricated using sputter processed perovskite films. From *J-V* measurement, a PCE of 1.84% was confirmed in PSCs employing sputter processed perovskite films. The EQE of the sputter processed PSCs was markedly increased by applying a reverse bias voltage during measurements. It indicated that the photovoltaic performance of sputter processed PSCs will be improved by reducing the number of defects in the perovskite films. Cross-sectional SEM observation of sputter processed films deposited on random-pyramid-textured Si substrates revealed that homogeneous PbI_2 and/or perovskite films can be fabricated on substrates with a large roughness.

Results described in this chapter indicate that sputtering process, which has used for industrial using, can be applied for fabrication of PSCs. Because homogeneous and large films can be fabricated with reproducibility by sputtering, it might contribute to solve the problems of PSCs. In addition, knowledge obtained in this chapter will contribute to the growth of not only PSCs field but also other research field such as tandem solar cells.

References

[1] L. Qiu, Z. Liu, L. K. Ono, Y. Jiang, D.-Y. Son, Z. Hawash, S. He, and Y. Qi, *Adv. Funct. Mater.*, 1806779 (2018).

[2] M. B. Islam, M. Yanagida, Y. Shirai, Y. Nabetani, and K. Miyano, *ACS Omega* **2**, 2291 (2017).

[3] X. Yao, J. Liang, Y. Li, J. Luo, B. Shi, C. Wei, D. Zhang, B. Li, Y. Ding, Y. Zhao, and X. Zhang, *Adv. Sci.* **4**, 1700008 (2017).

[4] R. Watanabe, Y. Eguchi, T. Yamada, and Y. Saito, *Int. J. Photoenergy* **2015**, 147836 (2015).

[5] S. Yoshinaga, Y. Ishikawa, S. Araki, T. Honda, Y. Jiang, and Y. Uraoka, *Jpn. J. Appl. Phys*. **56**, 022301 (2017).

[6] D.-L. Wang, H.-J. Cui, G.-J. Hou, Z.-G. Zhu, Q.-B. Yan, and G. Su, *Sci. Rep.* **6**, 18922 (2016).

[7] T. Dittrich, C. Awino, P. Prajongtat, B. Rech, and M. C. L.-Steiner, *J. Phys. Chem. C* **119**, 23968 (2015).

[8] H. Zhang, J. Mao, H. He, D. Zhang, H. L. Zhu, F. Xie, K. S. Wong, M. Grätzel, and W. C. H. Choy, *Adv. Energy Mater.* **5**, 1501354 (2015).

[9] S. Sanzaro, E. Smecca, G. Mannino, C. Bongiorno, G. Pellegrino, F. Neri, G. Malandrino, M. R. Catalano, G. G. Condorelli, R. Iacobellis, L. D. Marco, C. Spinella, A. L. Magna, and A. Alberti, *Sci. Rep.* **6**, 39509 (2016).

[10] P.-S. Shen, J.-S. Chen, Y.-H. Chiang, M.-H. Li, T.-F. Guo, and P. Chen, *Adv. Mater. Interfaces* **3**, 1500849 (2016).

[11] Y.-H. Chiang, H.-M. Cheng, M.-H. Li, T.-F. Guo, and P. Chen, *ChemSusChem* **9**, 2620 (2016).

[12] M.-H. Li, H.-H. Yeh, Y.-H. Chiang, U.-S. Jeng, C.-J. Su, H.-W. Shiu, Y.-J. Hsu, N. Kosugi, T. Ohigashi, Y.-A. Chen, P.-S. Shen, P. Chen, and T.-F. Guo, *Adv. Mater.* **30**, 1801401 (2018).

Chapter 5

Conclusions

5.1 Conclusions

In this work, PSCs were suggested as power sources for IoT applications and the low-illuminance characteristics were investigated. In addition, sputtering process was suggested as a novel fabrication process to overcome poor reliability of PSCs. Results obtained each chapters are summarized below.

In Chapter 2, characteristics of PSCs were investigated under various light intensities with AM 1.5 spectrum, which is similar to emission spectrum of sunlight. From *J-V* measurements, it was clarified that PSCs can maintain higher V_{OC} value under low-illuminance conditions than a-Si solar cells, which has been used for indoor applications. Spectral sensitivity of PSCs was also investigated under low-illuminance conditions by EQE measurements. As a result, PSCs showed acceptable spectral response in wavelength range of 400-700 nm, which is included in typical indoor lighting such as white LED or fluorescent lamp. These results indicate PSCs work efficiently even under low-illuminance conditions. The internal resistance of PSCs was evaluated with impedance spectroscopy under various light intensities. From the results, it was considered that the mp-TiO_2 layer included in mesostructured PSCs acts as an internal resistance and decreases V_{OC} under low-illuminance conditions. Therefore, planar type PSCs were suggested as suitable device structure under low-illuminance conditions and the *J-V* characteristics were

evaluated. Planar type PSCs kept higher V_{OC} than mesostructured PSCs under low-illuminance conditions.

In Chapter 3, characteristics of PSCs were investigated under fluorescent lamp illumination, which is one of the indoor lightings. It was confirmed that 3-cat-Br16 PSCs, which have optimum band gap for AM 1.5 spectrum showed PCE of 27.1% under 200 lx condition. In addition, 3-cat-Br50 PSCs, which of band gap was tuned, showed PCE of over 30% under 200 lx illumination. These values are highest value compared with that of other kind of solar cells under similar light intensities. Commonly, bromide doping causes lower photovoltaics performance due to form recombination site in perovskite layer under 1 sun condition. Results described in this chapter indicate the phase segregation affect slight influence on photovoltaic performance of PSCs under low-illuminance conditions. From stability test, PSCs stored under ambient condition showed 93% of its initial PCE after being stored for approximately a month.

In Chapter 4, sputtering process was suggested as novel fabrication process of PSCs and the sputter processed perovskite films and PSCs were evaluated. From the XRD measurement and UV/vis spectroscopy, it was confirmed that $CH_3NH_3PbI_3$ perovskite films could be synthesized from sputtered PbI_2 films. After sputtering process for perovskite films have been established, PSCs were fabricated using sputter processed perovskite films. From *J-V* measurement, a PCE of 1.84% was confirmed in PSCs employing sputter processed perovskite films. The EQE of the sputter processed PSCs was markedly increased by applying a reverse bias voltage during measurements. It indicated that there is still room to improve the PCE of PSCs by reducing the number of defects in the perovskite films.

In this study, it is revealed that PSC shows low voltage losses under low-illuminance conditions and it works efficiently under indoor lighting such as fluorescent lamp. Moreover, strategies to achieve higher PCE PSCs under low-illuminance conditions are suggested such as device structure and composition of light absorbing layer. In addition, sputtering process, which will solve problems of PSCs, are established. Results obtained in this study indicates that PSCs have great potential for power sources of IoT applications. Thus, this thesis will contribute to further advancement of IoT society and will enrich human life.

5.2 Suggestions for future work

Power sources of sensors are considered as one of the IoT applications of PSCs. In this system, sensing devices and wireless communication unit require power supply. Assuming the required consumed power as 200 μW, over 10 cm^2 device area is needed when the condition is same as in this thesis. To reduce the device area, some PSCs should be connected in series. Laser-scribing patterning has already been established for perovskite solar modules, and this technique probably available for smaller sized PSCs [1-3]. When 3 PSCs are connected in series, 4 cm^2 is enough to ensure 200 μW. However, it is difficult to put the sensors under light irradiation at all time. Therefore, combination with other power sources such as thermoelectric devices should be considered. Also, the power output of PSCs will decrease due to its deterioration. Thus, it is also considerable that to establish replaceable PSCs system.

Even focused on only PSCs, several topics need to investigate are still remained. Some of the topics from results in this thesis are described below.

1. Investigation of low-illuminance characteristics of Pb-free PSCs

PSCs showing high PCE include Pb element that is toxic in their composition. Particularly, Pb element should be eliminated for indoor using. There are already some reports on Pb-free PSCs using Sn, Sb, Bi, and Ti instead of Pb element [4-8]. However, there are no reports on low-illuminance characteristics on Pb-free PSCs. To investigate the characteristics will give us further interesting knowledge.

2. Phase segregation of perovskite films under low-illuminance conditions

This study demonstrated that bromide doping is an effective method to improve the photovoltaic performance of PSCs under indoor lighting. However, bromide-rich PSCs suffer from phase segregation under light illumination. It seemed that effect of the phase segregation on the performance of PSCs under low-illuminance condition is small. However, there are no findings showing state of bromide-rich perovskite films after exposed to indoor lightings long time. Therefore, systematical investigation on phase segregation under low-illuminance condition is necessary for practical using of PSCs under indoor lightings.

3. Improving sputter process for PSCs

Although sputter processed PSCs showed photovoltaic performance, the PCE is lower than that of conventional PSCs. Improving the PCE is mandatory for practical using of sputter processed PSCs. As described in Chapter 4, film density of PbI_2 plays an important role in PCE of PSCs. The film density can be controlled by changing the sputtering conditions. Therefore, to investigate the effect of PbI_2 sputter conditions on PSCs performance is necessary to further development of sputter processed PSCs.

References

[1] A. L. Palma, F. Matteocci, A. Agresti, S. Pescetelli, E. Calabro, L. Vesce, S. Christiansen, M. Schmidt, and A. D. Carlo, *IEEE Jounal of Photovoltaics* **7**, 1674 (2017).

[2] S. -J. Moon, J. -H. Yum, L. Lofgren, A. Walter, L. Sansonnens, M. Benkhaira, S. Nicolay, J. Bailat, and C. Ballif, *IEEE Jounal of Photovoltaics* **5**, 1087 (2015).

[3] B. Turan, A. Huuskonen, I. Kuhn, T. Kirchartz, and S. Haas, *Solar RRL* **1**, 1700003 (2017).

[4] N. Ito, M. A. Kamarudin, D. Hirotani, Y. Zhang, Q. Shen, Y. Ogomi, S. Iikubo, T. Minemoto, K. Yoshino, and S. Hayase, *J. Phys. Chem. Lett.* **9**, 1682 (2018).

[5] P. Karuppuswamy, K. M. Boopathic, A. Mohapatra, H.-C. Chen, K.-T. Wongd, P.-C. Wang, and C.-W. Chu, *Nano Energy* **45**, 330 (2018).

[6] A. K. Baranwal, H. Masutani, H. Sugita, H. Kanda, S. Kanaya, N. Shibayama, Y. Sanehira, M. Ikegami, Y. Numata, K. Yamada, T. Miyasaka, T. Umeyama, H. Imahori and S. Ito, *Nano Convergence* **4**, 26 (2017).

[7] Z. Zhang, X. Li, X. Xia, Z. Wang, Z. Huang, B. Lei, and Y. Gao, *J. Phys. Chem. Lett*. **8**, 4300 (2017).

[8] M. Chen, M.-G. Ju, A. D. Carl, Y. Zong, R. L. Grimm, J. Gu, X. C. Zeng, Y. Zhou, and N. P. Padture, *Joule* **2**, 558 (2018).

List of Publications

A. Academic journals

1. **Itaru Raifuku**, Yasuaki Ishikawa, Seigo Ito, and Yukiharu Uraoka, "Characteristics of Perovskite Solar Cells under Low-Illuminance Conditions", *J. Phys. Chem. C* **120**, 18986 (2016).

2. **Itaru Raifuku**, Yasuaki Ishikawa, Tiphaine Bourgeteau, Yvan Bonnasieux, Pere Roca i Cabarrocas, and Yukiharu Uraoka, "Fabrication of Perovskite Solar Cells using Sputter-Processed $CH_3NH_3PbI_3$ Films", *Applied Physics Express* **10**, 094101 (2017).

3. **Itaru Raifuku**, Yasuaki Ishikawa, Yu-Hsien Chiang, Pei-Ying Lin, Ming-Hsien Li, Hiroto Murakami, Yukiharu Uraoka, and Peter Chen, "Enormous Performance of Perovskite Solar Cells under Ambient Lighting", (submitted).

B. Related Publications

1. Ippei Inoue, Yuki Umemura, **Itaru Raifuku**, Kenichi Toyoda, Yasuaki Ishikawa, Seigo Ito, Hisashi Yasueda, Yukiharu Uraoka, and Ichiro Yamashita, "Biotemplated Synthesis of TiO_2-Coated Gold Nanowire for Perovskite Solar Cells", *ACS Omega* **2**, 5478 (2017).

2. Zhang Song, Tiphaine Bourgeteau, **Itaru Raifuku**, Yvan Bonnassieux, Erik Johnson, Yasuaki Ishikawa, Martin Foldyna, Pere Roca i Cabarrocas, and Yukiharu Uraoka, "Structural Study

of NiO_x Thin Films Fabricated by Radio Frequency Sputtering at Low Temperature", *Thin Solid Films* **646**, 209 (2018).

3. Yuki Hashima, Yasuaki Ishikawa, **Itaru Raifuku**, Ippei Inoue, Naofumi Okamoto, Ichiro Yamashita, Tsuyoshi Minami, and Yukiharu Uraoka, "Easy and Green Preparation of a Graphene-TiO_2 Nanohybrid using a Supramolecular Biomaterial Consisted of Artificially Bifunctionalized Proteins and its Application for a Perovskite Solar Cell", *Nanoscale* **10**, 19249 (2018).

Presented Works

A. Presentations at international conference

1. **Itaru Raifuku**, Yasuaki Ishikawa, and Yukiharu Uraoka, "Characteristics of Perovskite Solar Cells under Low Illuminance condition", the 2015 International Meeting for Future of Electron Devices, Kansai (IMFEDK2015), Kyoto, Japan, June (2015).

2. **Itaru Raifuku**, Yasuaki Ishikawa, Seigo Ito, and Yukiharu Uraoka, "Potential of Perovskite Solar Cells for Power Sources of IoT Applications", the 2016 International Meeting for future of electron Devices, Kansai (IMFEDK2016), Kyoto, Japan, June (2016).

3. **Itaru Raifuku**, Yasuaki Ishikawa, Seigo Ito, and Yukiharu Uraoka, "Characteristics Change of Perovskite Solar Cells by Device Structure under Low Illuminance Conditions", International Conference on Hybrid and Organic Photovoltaics (HOPV16), Swansea, United Kingdom, June (2016).

4. **Itaru Raifuku**, Yasuaki Ishikawa, Seigo Ito, and Yukiharu Uraoka, "Internal Resistance of Perovskite Solar Cells under Low Illuminance Conditions", The 23rd International Workshop on Active-Matrix Fratpanel Displays and Devices (AM-FPD16), Kyoto, Japan, July (2016).

5. **Itaru Raifuku**, Yasuaki Ishikawa, Seigo Ito, and Yukiharu Uraoka, "Investigation of Perovskite Solar Cells for Indoor applications", The 2nd Best-Efficiency Engineering Research Workshop for Perovskite Photovoltaics and Beyond (BWP-2), Osaka, Japan, August (2016).

6. **Itaru Raifuku**, Yasuaki Ishikawa, Seigo Ito, and Yukiharu Uraoka, "Fabrication of Perovskite Films by Sputtering and its Application", The 3rd Best-Efficiency Engineering Research Workshop for Perovskite Photovoltaics and Beyond (BWP-3), Seoul, Korea, January (2017).

7. **Itaru Raifuku**, Yasuaki Ishikawa, Tiphaine Bourgeteau, Yvan Bonnassieux, Pere Roca i Cabarrocas, and Yukiharu Uraoka, "Fabrication of Perovskite Solar Cells using Sputter Processed Perovskite Films", Asia Pacific Hybrid and Organic Photovoltaics Conference (AP-HOPV17), Yokohama, Japan, February (2017).

8. **Itaru Raifuku**, Yasuaki Ishikawa, Tiphaine Bourgeteau, Yvan Bonnassieux, Pere Roca i Cabarrocas, and Yukiharu Uraoka, "Development of Sputter Processed Perovskite Films toward Tandem Solar Cells", 232nd ECS meeting, Washington, America, October (2017).

9. **Itaru Raifuku**, Yasuaki Ishikawa, Seigo Ito, Yukiharu Uraoka, and Peter Chen, "Effect of Cation Substitution for Low-Illuminance Characteristics of Perovskite Solar Cells", 11th Aseanian Conference on Nano-Hybrid Solar Cells (NHSC11), Himeji, Japan, October (2017).

10. **Itaru Raifuku**, Yasuaki Ishikawa, Sachiko Morioka, Seigo Ito, Yukiharu Uraoka, and Peter Chen, "Low-Illuminance Characteristics of Triple Cation Perovskite Solar Cells", Grand Renewable energy 2018 International Conference and Exhibition (GRE2018), Yokohama, Japan, June (2018).

B. Presentations at domestic conference

1. **Itaru Raifuku**, Yasuaki Ishikawa, Zhang Song, Seigo Ito, and Yukiharu Uraoka, “ペロブスカイト型太陽電池の低照度特性に関する検討”, The 76th Japan Society of Applied Physics Autumn Meeting 2015, Nagoya Congress Center, Aichi, September (2015).

2. **Itaru Raifuku**, Yasuaki Ishikawa, Zhang Song, Seigo Ito, and Yukiharu Uraoka, “光強度によるペロブスカイト型太陽電池の特性変化”, The 63rd Japan Society of Applied Physics Spring Meeting 2016, Tolyo Inst. of Tech. Ookayama Campus, Tokyo, March (2016).

3. **Itaru Raifuku**, Yasuaki Ishikawa, Seigo Ito, and Yukiharu Uraoka, “デバイス構造によるペロブスカイト型太陽電池の低照度特性の変化”, 13th “the next generation of solar light power generation system” Symposium, Nagaoka City Hall Aore, Niigata, May (2016).

4. **Itaru Raifuku**, Yasuaki Ishikawa, Seigo Ito, Yukiharu Uraoka, and Peter Chen, “デバイス構造および光吸収層の組成がペロブスカイト型太陽電池の低照度特性に及ぼす影響”, 14th “the next generation of solar light power generation system” Symposium, Nagoya University Higashiyama Campus, Aichi, July (2017).

5. **Itaru Raifuku**, Yasuaki Ishikawa, Tiphaine Bourgeteau, Seigo Ito, Yvan Bonnassieux, Pere Roca i Cabarrocas, and Yukiharu Uraoka, “タンデム型太陽電池応用へ向けたスパッタ法によるペロブスカイト薄膜の作製”, The 78th Japan Society of Applied Physics Autumn Meeting 2017, Fukuoka Convention Center, Fukuoka, September (2017).

6. **Itaru Raifuku**, Yasuaki Ishikawa, Hiroto Murakami, Sachiko Morioka, Yikiharu Uraoka, and Peter Chen, "室内光照射下におけるペロブスカイト型太陽電池の発電特性", 15th "the next generation of solar light power generation system" Symposium, Hotel Sapporo art and literature museum, Hokkaido, July (2018).

C. Award

1. **IEEE EDS Kansai Chapter IMFEDK Student Paper Award**, the 2016 International Meeting for future of electron Devices, Kansai (IMFEDK2016).

2. **TCI Poster Award**, Aseanian Conference on Nano-Hybrid Solar Cells (NHSC11).

D. Related presentations

1. Yuki Hashima, **Itaru Raifuku**, Yasuaki Ishikawa, Naofumi Okamoto, Mutsunori Uenuma, and Yukiharu Uraoka, "タンパク質を用いたグラフェン-TiO_2複合材料の作製とペロブスカイト太陽電池への応用", 13th "the next generation of solar light power generation system" Symposium, Nagaoka City Hall Aore, Niigata, Japan, May (2016).

2. Yuki Hashima, **Itaru Raifuku**, Yasuaki Ishikawa, Mutsunori Uenuma, Naofumi Okamoto, Ichiro Yamashita, and Yukiharu Uraoka, "TiO_2 Coated Graphene/Mesoporous TiO_2 Composite Layer for Perovskite Solar Cells Produced by Supramolecular Protein", ECS Prime 2016, Honolulu, Hawaii, October (2016).

3. Zhang Song, Yasuaki Ishikawa, **Itaru Raifuku**, Tiphaine Bourgeteau, Yukiharu Uraoka, Erik Juhnson, Martin Foldyna, Yvan Bonnassieux, and Pere Roca i Cabarrocas, "Development of Recombination Layer in Perovskite/Microcrystalline Si Tandem Solar Cells", Technical Committee on Silicon Device and Materials (SDM), Nara, Japan, December (2016).

4. Sachiko Morioka, Yasuaki Ishikawa, **Itaru Raifuku**, Hiroto Murakami, and Yukiharu Uraoka, "電子ビーム法を用いたペロブスカイト型太陽電池の低温作製", 15th "the next generation of solar light power generation system" Symposium, Hotel Sapporo art and literature museum, Hokkaido, July (2018).

Appendix

A. Evaluate the phase segregation of mixed-halide perovskite films

In Chapter 3, it was suggested that phase segregation of mixed-halide perovskite materials occurs under light illumination. Here, EQE measurement and fluorescent spectroscopy are applied to evaluate the phase segregation.

A.1 Evaluation with EQE measurements

Figure A.1 (a) shows EQE spectra of a 3-cat-Br50 PSC. The sample showed response between 300 nm to 700 nm, which consistent with its absorption spectrum. The EQE value increased with the number of measurements. This is probably from defects in perovskite layer or interfaces. By contrast, there are no difference in the wavelength range of over 700 nm as shown in Figure A.1 (b). Figure A.2 shows EQE spectra of the 3-cat-Br50 PSCs measured with and without bias white light. The light intensity of white bias light is 100 mW/cm^2. When the white bias light is applied, EQE value increased in the wavelength range of over 700 nm. This result indicates that lower bandgap components appeared during light illumination.

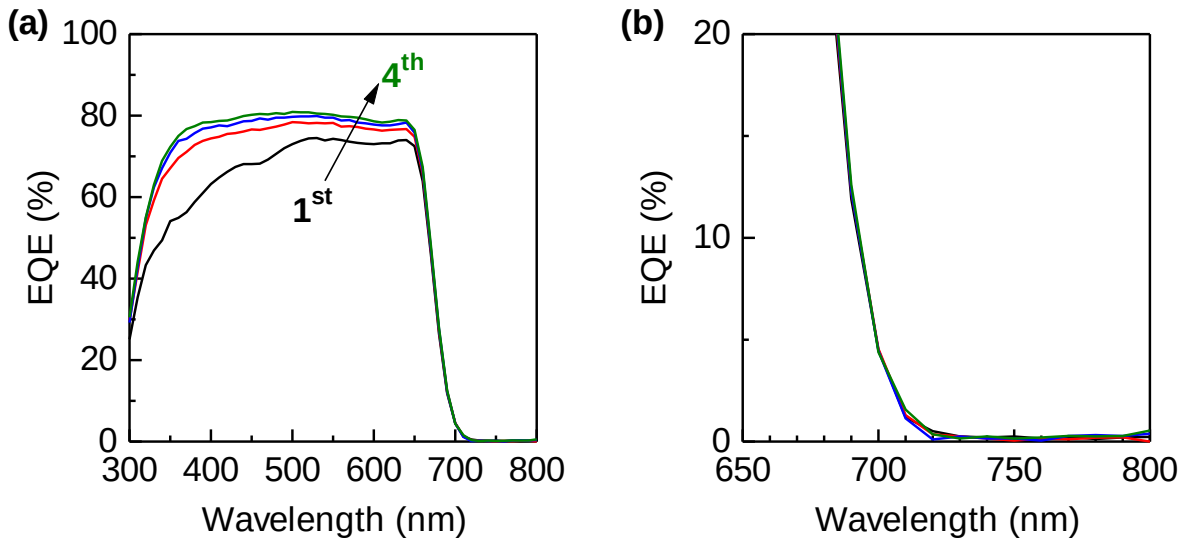

Figure A.1 External quantum efficiency spectra of 3-cat-Br50 perovskite solar cells measured several times with same condition.

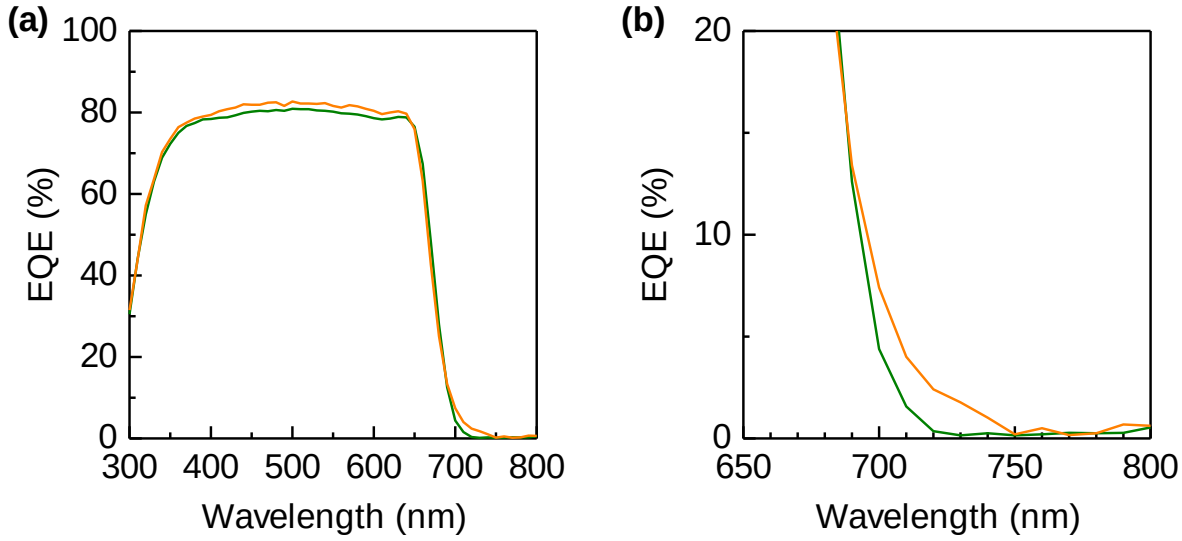

Figure A.2 External quantum efficiency (EQE) spectra of 3-cat-Br50 perovskite solar cells measured with white bias light. The green and orange lines represent EQE spectra measured without and with white bias light, respectively.

A.2 Evaluation with fluorescent spectroscopy

Figure A.3 shows emission spectra of a 3-cat-Br50 perovskite film before and after light exposure. The excitation wavelength is 455 nm. The pristine film shows an emission peak at 680 nm. After light exposure, another emission peak appeared at 720 nm. In addition, the intensity of the peak at 720 nm increased with light exposure time. This result also indicates light irradiation causes phase segregation of bromide-rich perovskite films. Figure A.4 shows emission spectra of the 3-cat-Br50 perovskite film stored under dark condition after light irradiation tests. The peak intensity at 720 nm became small after stored dark conditions. This tendency is consistent with previous reports on phase segregation of perovskite films [1].

Same investigation was carried out using fluorescent lamp (Intensity: 0.7 mW). Figure A.5 shows emission spectra of 3-cat-Br50 perovskite films before and after fluorescent lamp irradiation 7 h. There were no additional peaks after fluorescent lamp irradiation. This results indicates the influence of phase segregation on *J-V* characteristics of PSCs is negligible under low-illuminance conditions. However, further investigation is necessary to conclude it. For example, the effect of longer irradiation time or applying voltage should be evaluated.

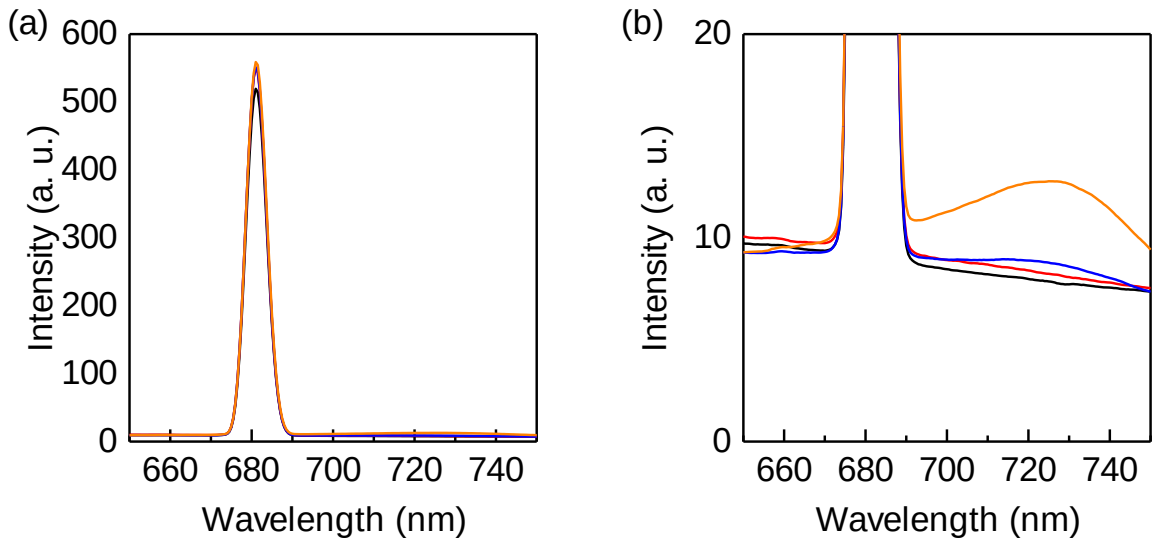

Figure A.3 Emission spectra of 3-cat-Br50 films. The black, red, blue, and orange lines represent emission spectra after 0, 10, 30, and 60 min light irradiation, respectively.

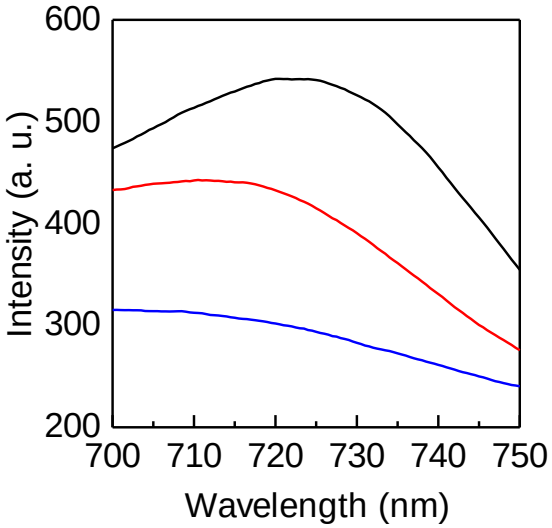

Figure A.4 Emission spectra of 3-cat-Br50 films stored dark condition after light irradiation tests. The black, red, and blue lines represent emission spectra after stored dark condition 0, 1.5, and 4.5 h, respectively.

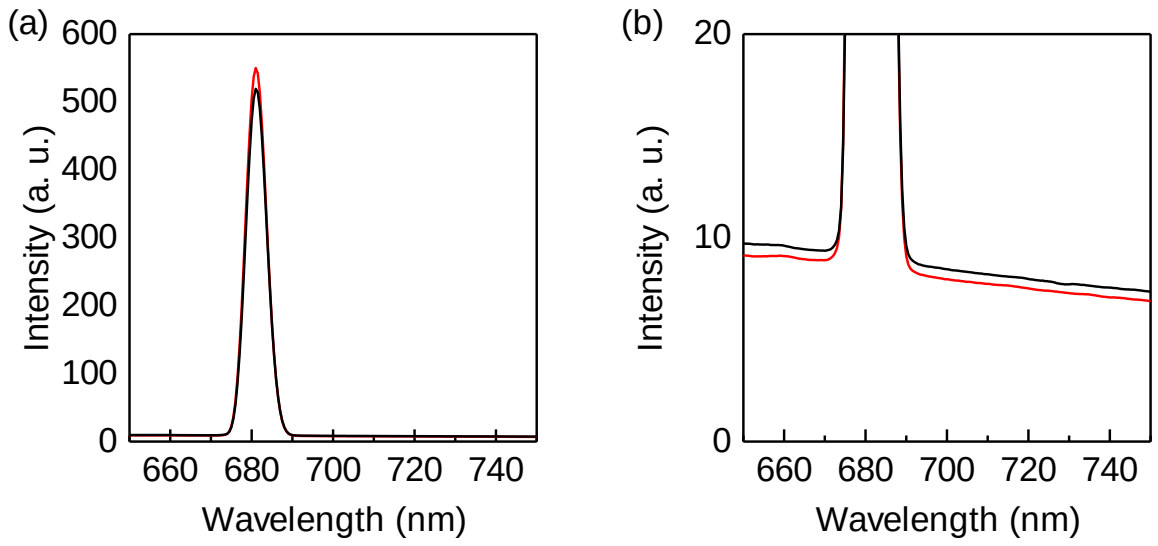

Figure A.5 Emission spectra of a 3-cat-Br50 film. The black and red lines represent before and after fluorescent lamp irradiation, respectively.

B. Fabrication of perovskite films via 1-step sputtering process

In Chapter 4, perovskite films were synthesized by reacting sputtered PbI_2 films and CH_3NH_3I gas. To establish more convenient process, 1-step sputtering process, that uses perovskite compounds as sputtering target, was investigated.

B.1 Fabrication of $CH_3NH_3PbI_3$ films

Firstly, conventional perovskite $CH_3NH_3PbI_3$ was investigated. The sputtering target was synthesized by mixing PbI_2 powder and CH_3NH_3I powder. Figure B.1 (a) shows XRD patterns of 1-step sputtered perovskite films. In the first sputtering, there was no PbI_2 peak at 12°. However, in the second sputtering, it was confirmed that sputtered perovskite films include a PbI_2 peak. Although $CH_3NH_3PbI_3$ powder shows black color, a part of sputtering target became yellow after sputtering as shown in Figure B.1 (b). This indicates CH_3NH_3I sublimed during sputtering and only yellow PbI_2 powder remains in the sputtering target.

To overcome above problem, excess amount of CH_3NH_3I powder was introduced in the sputtering target. Figure B.2 (a) shows XRD patterns of sputter processed perovskite films using CH_3NH_3I-rich sputtering target (PbI_2:CH_3NH_3I = 1:2 in molar ratio). The strongest peak at 9° in first and second sputtering is from CH_3NH_3I. The CH_3NH_3I peak disappeared in third sputtering. Comparing the PbI_2 peak at 12°, the peak intensity became stronger in second sputtering than first one. However, there was no clear PbI_2 peak in the XRD pattern of third sputtering. After the third sputtering, the state of sputtering target was confirmed. Figure B.2 (b) photo image of CH_3NH_3I-

rich perovskite sputtering target after sputtering. There was also yellow region as well as the stoichiometric target. This result indicate $CH_3NH_3PbI_3$ is not suitable for 1-step sputtering.

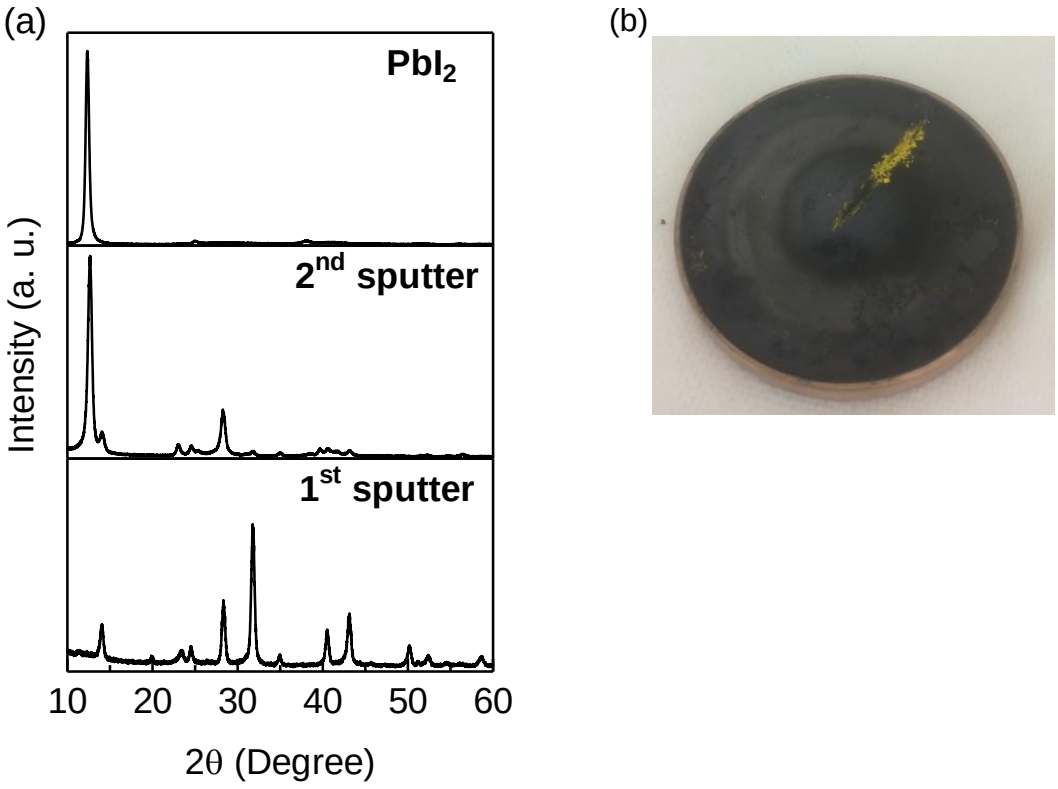

Figure B.1 (a) XRD patterns of 1-step sputtered $CH_3NH_3PbI_3$ films. (b) Photo image of $CH_3NH_3PbI_3$ sputtering target after sputtering. The molar ratio of PbI_2:CH_3NH_3I is 1:1. The surface of the target was scratched using spatula.

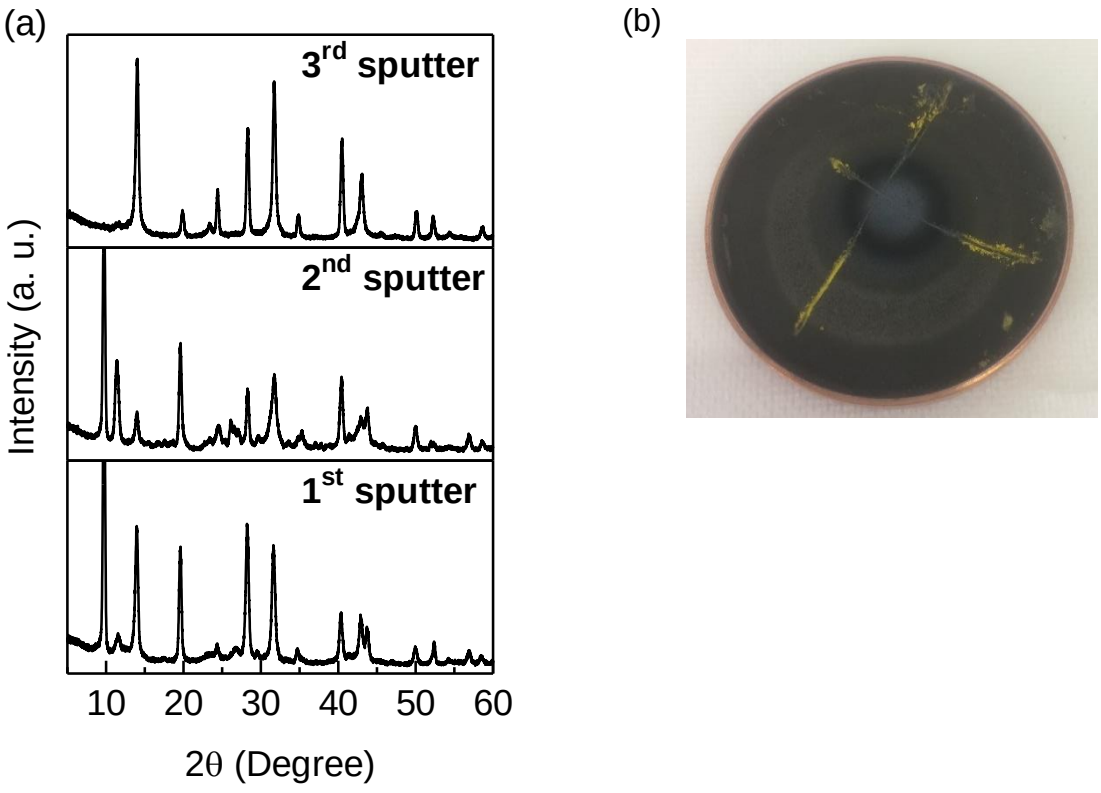

Figure B.2 (a) XRD patterns of 1-step sputtered $CH_3NH_3PbI_3$ films. (b) Photo image of $CH_3NH_3PbI_3$ sputtering target after sputtering. The molar ratio of PbI_2:CH_3NH_3I is 1:2. The surface of the target was scratched using spatula.

B.2 Fabrication of $Cs_3Bi_2I_9$

From the investigation of $CH_3NH_3PbI_3$, it is considered that sublimation cation is not suitable for 1-step sputtering. Therefore, $Cs_3Bi_2I_9$ including non-sublimation cation, CsI, was applied as a sputtering material.

$Cs_3Bi_2I_9$ powder was synthesized using CsI and BiI_3 powder. Firstly, CsI and BiI_3 were dissolved in DMF with molar ratio of 3:2. After clear solution was obtained, the solution was added into toluene that is an anti-solvent. The precipitate was rinsed with diethyl ether and dried at 100°C overnight in N_2 gas filled glovebox.

To check the composition of synthesized powder, the powder was dissolved in DMF and spin-coated on glass substrates. Figure B.3 (a) shows the XRD pattern of solution-processed $Cs_3Bi_2I_9$ films. The diffraction pattern was consistent with that of $Cs_3Bi_2I_9$. Figure B.3 (b) shows the Tauc plot of spin-coated $Cs_3Bi_2I_9$ film. The bandgap was estimated as 2.2 eV, which is consistent with literature value [2].

The synthesized powder and spin-coated films showed reddish orange color. However, sputtered films showed blackish color as shown in Figure B.4. Sputter processed films showed clearly difference XRD pattern and bandgap as shown in Figure B.5. From the XRD pattern, the composition of sputtered films was assigned as BiI_3. A safety data sheet (from Kojundo Chemical Laboratory) and a literature indicates BiI_3 is one of a sublimation compound [3]. Therefore, it is considered that BiI_3 is sputtered faster than CsI and as a result, deposited films are almost consisted with BiI_3. Figure B.6 shows photo images of $Cs_3Bi_2I_9$ target before and after sputtering. There

were entirely white region after sputtering. Because the color of CsI powder is white, it is considered that CsI tend to remain in the target after sputtering.

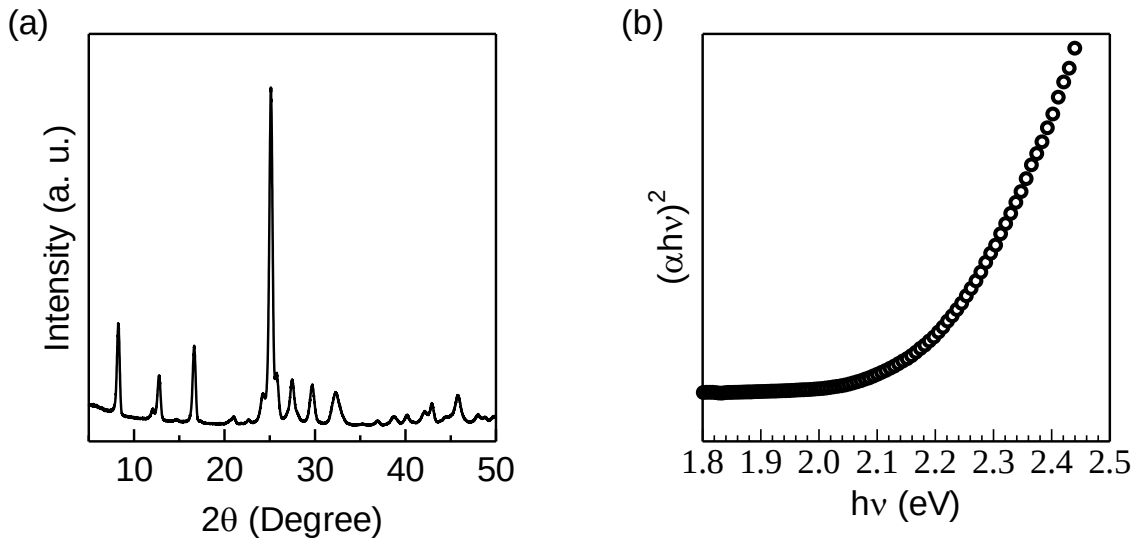

Figure B.3 (a) XRD pattern and (b) Tauc plot of spin-coated $Cs_3Bi_2I_9$ films.

Figure B.4 Photo image of the sputtered film using $Cs_3Bi_2I_9$ powder.

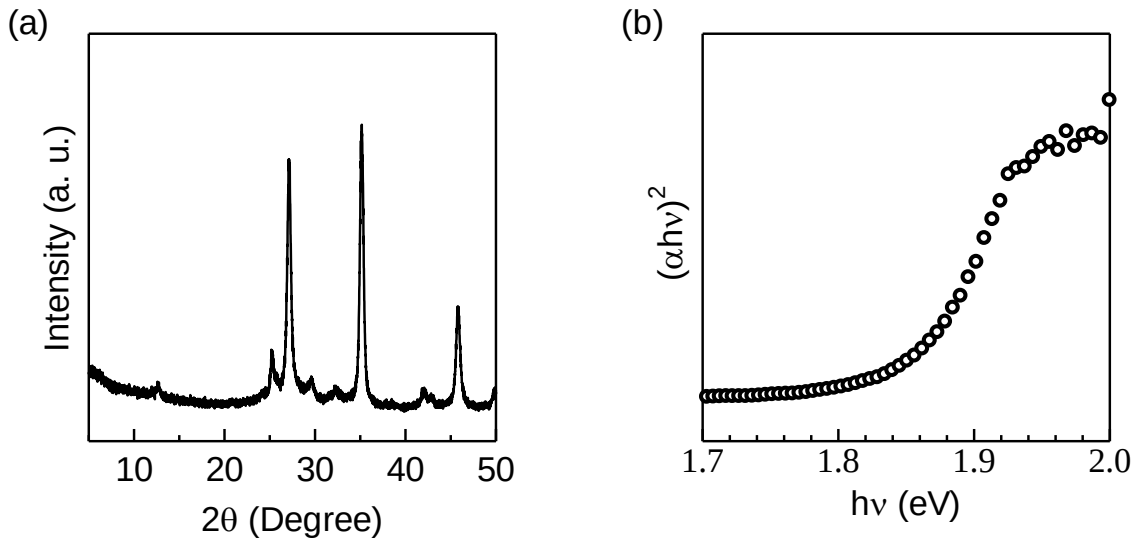

Figure B.5 (a) XRD pattern and (b) Tauc plot of sputtered films using $Cs_3Bi_2I_9$ powder.

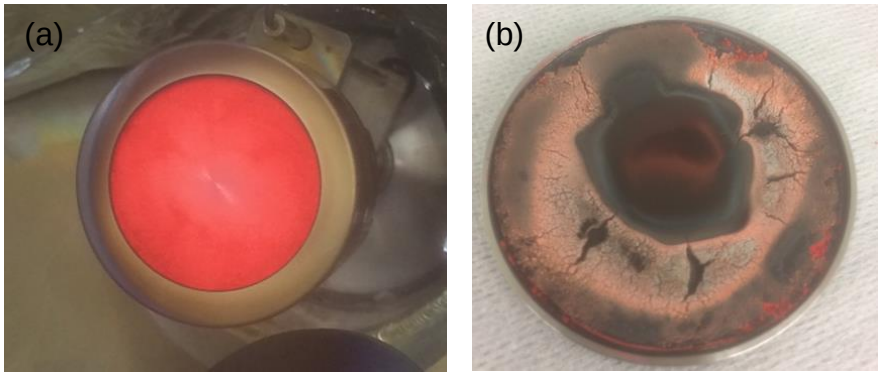

Figure B.6 Photo image of $Cs_3Bi_2I_9$ sputtering target (a) before and (b) after sputtering.

B.3 Fabrication of $CsPbI_3$ films

From above investigations, it is considered that both cation and metal halide should be non-sublimation materials to achieve 1-step processed perovskite films. Therefore, $CsPbI_3$, consisted with CsI and PbI_2 was applied as sputtering target. CsI and PbI_2 mixed powder (molar ratio 1:1) was used as sputtering target.

Figure B.7 shows photo images of sputtered $CsPbI_3$ films at 200°C. The pristine film showed blackish color as shown in Figure B.7 (a). After exposed to air, the color became yellow as shown in Figure B.7 (b).

It is reported that $CsPbI_3$ has several crystal structures [4, 5]. Black color α-$CsPbI_3$, which shows photovoltaic performance, is obtained at high temperature (over 300°C). When the α-$CsPbI_3$ is exposed to air at room temperature, it becomes yellow color δ-$CsPbI_3$, which does not show photovoltaic performance. Because the behavior of sputter-processed films is similar to above phenomena, it is considered that the sputter-processed films are $CsPbI_3$. Actually, it was confirmed that the sputtered films become black color again after annealing in N_2 filled glovebox.

XRD patterns of sputter-processed yellow films are compared with that of solution-processed δ-$CsPbI_3$ films. The sputtered yellow films showed similar XRD patterns with solution-processed films as shown in Figure B.8. Therefore, it is considered that $CsPbI_3$ films were successfully obtained by 1-step sputtering process.

Results in this section indicate that it is necessary to choose non-sublimation cation and metal halide as starting materials to achieve 1-step sputter-processed perovskite films.

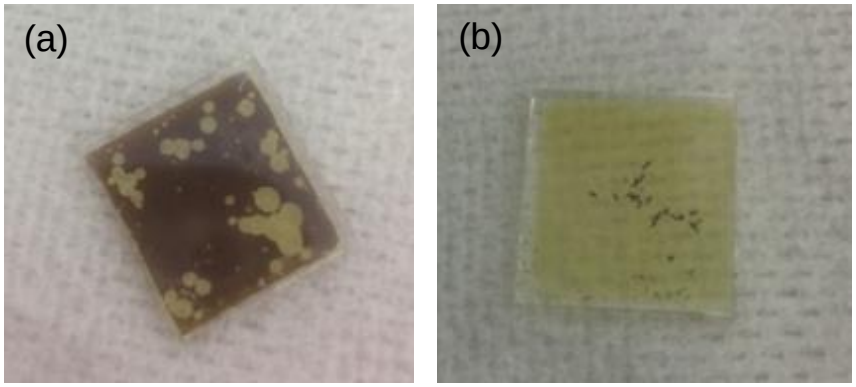

Figure B.7 Photo images of sputtered $CsPbI_3$ films. (a) Pristine film and (b) after air exposure.

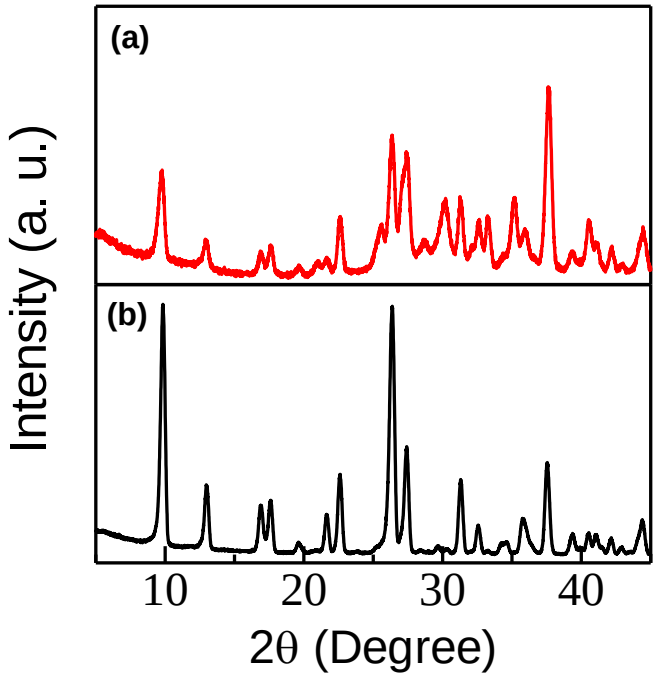

Figure B.8 XRD patterns of (a) sputter processed (b) solution processed $CsPbI_3$ films.

C. EDX mapping of sputter processed PbI_2 and $MAPbI_3$ films

C.1 EDX mapping of sputter PbI_2 films

When the sputter process is applied to fabricate mesostructured PSCs, there is a concern that sputtered PbI_2 particles cannot penetrate in mp-TiO_2 layer. Therefore, cross-sectional SEM observation was carried out. Figure C.1 shows cross-sectional SEM image of a PbI_2 deposited on FTO/mp-TiO_2 substrate. It seemed that PbI_2 film was formed on mp-TiO_2 layer. To evaluate in more detail, EDX mapping was taken using same sample. Figure C.2 shows EDX mapping of Sn, Pb, and Ti elements. Sn element existed along with FTO region. Pb element showed inhomogeneous distribution and surface region showed brighter color than bottom side. By contrast, Ti element showed blight color near the FTO region. These results indicate that sputtered PbI_2 films cannot penetrate uniformly in mp-TiO_2 layer. Therefore, planar structure was chosen as device architecture of sputter processed PSCs in this thesis. However, large noise in the EDX mappings indicates that further investigation is necessary to conclude suitable device architecture.

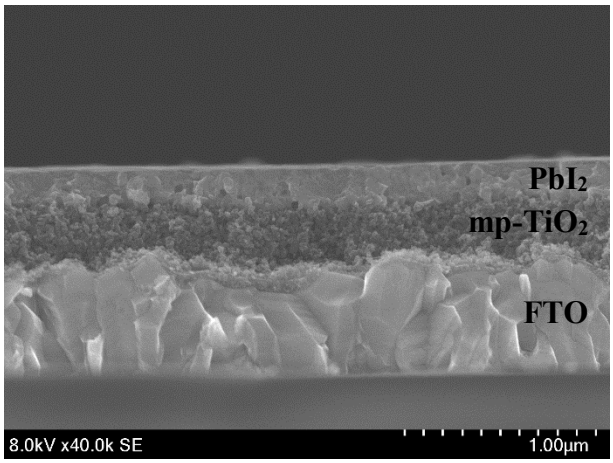

Figure C.1 cross-sectional SEM image of PbI_2 film sputtered on FTO/mp-TiO_2.

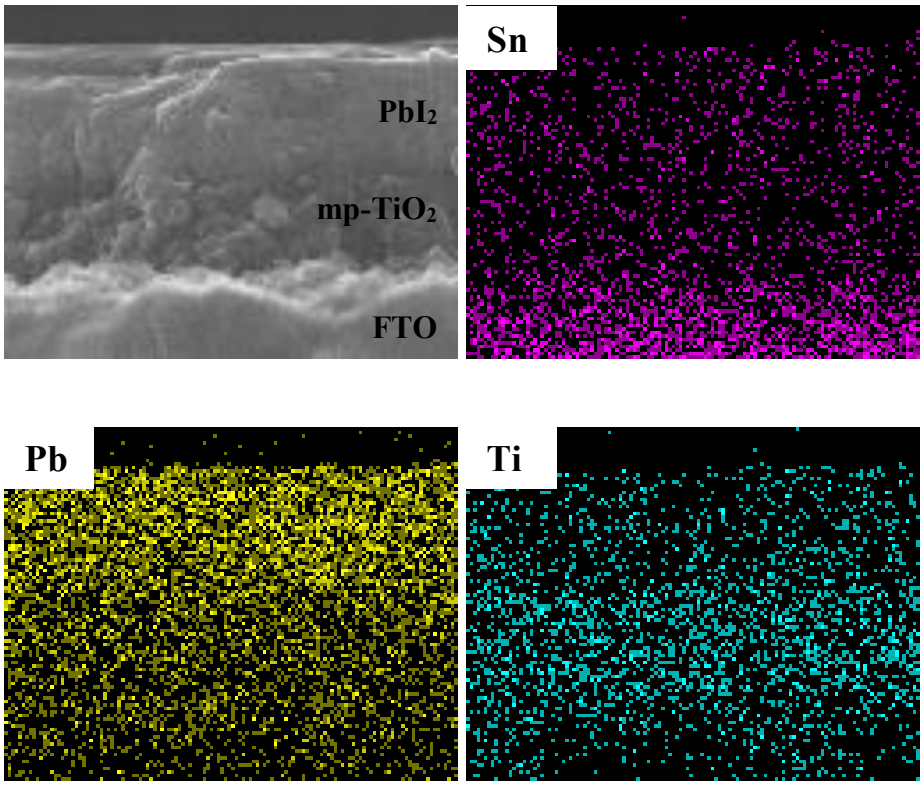

Figure C.2 EDX mapping of FTO/mp-TiO_2/PbI_2.The pink, yellow, and aqua color mapping represent Sn, Pb, and Ti, respectively.

C.2 EDX mapping of sputter processed $CH_3NH_3PbI_3$ films

In order to evaluate the composition of sputter processed perovskite films, EDX measurement was carried out with perovskite films deposited on Si substrates. Figure C.3 shows EDX mapping of C, N, Pb, I, and Si elements. The perovskite/Si substrate interface could be recognized from Si and Pb/I mapping. It was also confirmed that carbon and nitrogen elements existed at around the interface of perovskite/Si substrate. It indicates CH_3NH_3I gas can penetrate in sputtered PbI_2 films.

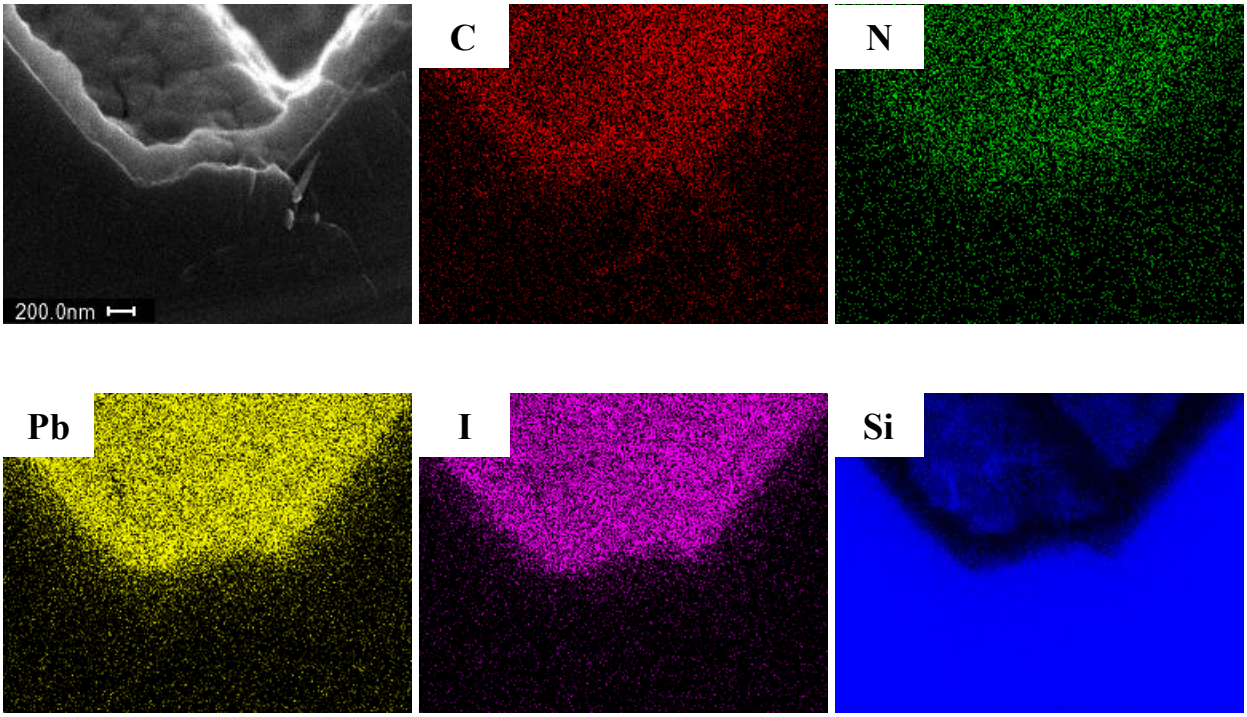

Figure C.3 EDX mapping of sputter processed perovskite films deposited on random-pyramid-textured Si substrates. The red, green, yellow, pink, and blue color mapping represent C, N, Pb, I, and Si, respectively.

References

[1] S. J. Yoon, S. Draguta, J. S. Manser, O. Sharia, W. F. Schneider, M. Kuno, and P. V. Kamat, *ACS Energy Lett.* **1**, 290 (2016).

[2] B.-W. Park, B. Philippe, X. Zhang, H. Rensmo, G. Boschloo, and E. M. J. Johansson, *Adv. Mater.* **27**, 6806 (2015).

[3] X. Chen, Y. Myung, A. Thind, Z. Gao, B. Yin, M. Shen, S. B. Cho, P. Cheng, B. Sadtler, R. Mishra, and P. Banerjee, *J. Mater. Chem. A* **5**, 24728 (2017).

[4] P. Luo, W. Xia, S. Zhou, L. Sun, J. Cheng, C. Xu, and Y. Lu, *J. Phys. Chem. Lett.* **7**, 3603 (2016).

[5] J. Liang, C. Wang, P. Zhao, Z. Lu, Y. Ma, Z. Xu, Y. Wang, H. Zhu, Y. Hu, G. Zhu, L. Ma, T. Chen, Z. Tie, J. Liua, and Z. Jin, *Nanoscale* **9**, 11841 (2017).